Title

Statistical Modeling Procedures for Rapid Battery Pack Characterization

Author

Beslow, Lucas

Publication Date

2023

Peer reviewed|Thesis/dissertation

Statistical Modeling Procedures for Rapid Battery Pack Characterization

By

LUCAS BESLOW
DISSERTATION

Submitted in partial satisfaction of the requirements for the degree of

DOCTOR OF PHILOSOPHY

in

Energy Systems

in the

OFFICE OF GRADUATE STUDIES

of the

UNIVERSITY OF CALIFORNIA

DAVIS

Approved:

Jae Wan Park, Chair

Xinfan Lin

Alan Jenn

Committee in Charge

2023

Acknowledgements

I want to express my sincere gratitude to my Major Professor, Dr. Jae Wan Park, for guiding and supporting me throughout the entirety of my PhD study. I would also like to thank my other dissertation committee members, Dr. Xinfan Lin and Dr. Alan Jenn, for their feedback and guidance in the dissertation writing process. In addition, I am incredibly grateful for the helpfulness and support of the Energy Graduate Group faculty, especially Annemarie Schaaf, throughout my time here at UC Davis in the Energy Systems program. Their patience and willingness to always answer any questions I had regarding the program, as well as their helpfulness in ensuring I was funded during my time here was invaluable and allowed for me to progress through the program smoothly.

On a more personal note, I would not have gotten through this process without the consistent support from my family and friends. The constant check-ins and genuine interest to see me succeed in this endeavor from my sisters, in-laws, friends made in Davis, and friends I made long before my time here did not go unnoticed and was instrumental in keeping me motivated to achieve my goals.

My wife, Karly, has sacrificed an incredible amount of her time, effort, and personal comfort to provide me with the indispensable support I needed to keep me going through the toughest and most daunting times of the past four years (and well before that). I cannot thank her enough for this, as well as providing me with some of the most joyful times of my life during these uncertain and exciting few years in Davis. Thank you, Karl.

To my parents: my accomplishments, and more importantly the person I am today, is a testament to your unconditional love and unwavering belief in me. Even when I was an unmotivated and underperforming student, you always pushed me to reach as high as I could academically and otherwise. Thank you for everything, Mom and Dad.

Abstract

As lithium-ion battery (LIB) cells degrade over time and usage, it is crucial to understand the remaining capacity, also known as State of Health (SoH), and inconsistencies between cells in a pack, also known as cell-to-cell variation (CtCV), to appropriately operate and maintain LIB packs. This study outlines efforts to model pack SoH and SoH CtCV of nickel-cobalt-aluminum (NCA) and lithium-iron-phosphate (LFP) battery packs consisting of four cells in series using pack-level voltage data. Using a small training data set and an under 3-minute testing procedure, partial least squares regression (PLS) models were built and achieved a mean absolute error of 0.38% and 1.43% pack SoH for NCA and LFP packs, respectively. PLS models were also built that correctly categorized packs having low, medium, and high ranked SoH CtCV 72.5% and 65% of the time for NCA and LFP packs, respectively. This study further investigates the relationships between pack SoH, SoH CtCV, and the voltage response of NCA and LFP packs. The slope of the discharge voltage response of the NCA packs was shown to have a strong correlation with pack dynamics and pack SoH, and the lowest SoH cell within NCA packs was shown to dominate the dynamic response of the entire pack.

Contents

Nomenclature

Abbreviation	Definition
Ah	Ampere-Hours
BMS	Battery Management System
CCCV	Constant Current Constant Voltage
CtCV	Cell-to-Cell Variation
DoD	Depth of Discharge
DVA	Differential Voltage Analysis
ECM	Equivalent Circuit Models
EIS	Electrochemical Impedance Spectroscopy
EoL	End Of Life
ESS	Energy Storage System
EV	Electric Vehicle
HEV	Hybrid Electric Vehicle
HPPC	Hybrid Pulse Power Characterization
ICA	Incremental Capacity Analysis
IC	Incremental Capacity
LAM	Loss of Active Material
LCO	Lithium Cobalt Oxide
LFP	Lithium-Iron-Phosphate
LIB	Lithium-Ion Battery
LLI	Loss of Lithium Inventory
LMO	Lithium Manganese Oxide
LOOCV	Leave-One-Out Cross-Validation
LTO	Lithium Titanium Oxide
MAE	Mean Absolute Error
MAPE	Mean Absolute Percent Error
MaxAE	Maximum Absolute Error
MLR	Multiple Linear Regression
MSE	Mean Squared Error
NCA	Nickel-Cobalt-Aluminum
NIPALS	Non-Linear Iterative Partial Least Squares
NMC	Lithium Nickel Manganese
OCV	Open Circuit Voltage
OLS	Ordinary Least Squares
PCA	Principle Component Analysis
PLS	Partial Least Squares
RC	Resistor-Capacitor
RMSE	Root-Mean Squared Error
RUL	Remaining Useful Life
SEI	Solid Electrolyte Interphase
SoC	State Of Charge
SoE	State Of Energy
SoH	State Of Health
SoP	State Of Power

Part I. Introduction

Lithium-ion batteries (LIBs) have become an increasingly integral technology world-wide due to their vast array of applications. Many products ranging from the size of a cell phone to electric vehicles (EVs) and even utility-scale energy storage increasingly rely on LIB technology for their ability to store and provide energy and power [1], [2]. Commercially introduced in the early 1990s [3], LIBs have been a source of great interest for industry and researchers due to the numerous benefits they provide. Mobile rechargeable power sources have unlocked monumental advances in society, including the usage of cellular phones, laptop computers, electric and hybrid electric vehicles, and more. LIBs have been an important innovation in this field, increasing the lifespan of products and providing power and energy at a fraction of the size and weight of previous technologies [4], [5].

Though LIB technology has matured significantly since its inception, there are still plenty of areas of research that need to be further developed to expand the usefulness, value, and safety of LIBs and the products that rely on them. One of these critical areas involves the accurate diagnosis of the state of degradation of a battery. Over time and usage, LIBs degrade due to a variety of mechanisms that negatively affect their ability to perform reliably and safely. A quantification of the state of battery degradation is referred to as state of health (SoH). SoH is one of the foundational parameters that influences and determines a myriad of battery behaviors and operational limitations.

This dissertation seeks to respond to deficiencies in LIB research by offering novel contributions in the field of SoH diagnostic procedures. Firstly, this dissertation will provide important and necessary background regarding LIBs, including the current and prospective status of the technology. Next, relevant theoretical background and the current state of LIB research literature will be presented and critiqued. Finally, in response to these critiques, this dissertation will explicitly present the research

methodology and discuss the results of a study conducted to rapidly and accurately diagnose battery pack SoH.

1 Background

1.1 Lithium-ion Battery Basics

1.1.1 Battery Operation

At its most basic level, the main function of a LIB is to convert electrical energy to and from chemical energy. The chemical reactions that govern these processes are reversible, allowing LIBs to be charged and discharged repeatedly, classifying LIBs into the category of "secondary batteries." Unlike other common secondary batteries such Lead Acid or Nickel Cadmium batteries, charge-carrying lithium ions are reversibly inserted ("intercalated") and removed ("deintercalated") from the crystalline and layered structures of the battery cell's anode and cathode. This process of lithium ions "rocking" from one electrode to the other is why LIBs are colloquially termed "rocking-chair batteries" [6].

The common components of a LIB include a carbon-based anode (e.g., graphite), lithium metal oxide cathode, electrically insulated separator, liquid electrolyte for ion transfer, and current collectors for electrical interface with external circuits [7]–[9]. The charging and discharging procedures of LIBs involve redox reactions at the cathode and anode, where Lithium ions move from one electrode to the other, causing or in response to a flow of electrons through an external circuit. The basic reactions at the graphite anode and lithium metal (Me) oxide cathode during charging and discharging are illustrated in equations 1 and 2 [6]–[8], respectively:

$$Li_{x+1}C_6 \leftrightarrows Li_xC_6 + xLi^+ + xe^- \quad (1)$$

$$Li_xMeO_2 + xLi^+ + xe^- \leftrightarrows Li_{x+1}MeO_2 \quad (2)$$

During charging, an external power supply forces electrons to flow from the cathode to anode through an external circuit. This results in the deintercalation of lithium ions from the cathode. The flow of electrons results in a negative charge buildup on the anode side of the cell, causing positively charged lithium ions to diffuse through the electrolyte, pass through the separator, and then intercalate into the anode. Conversely, the reverse occurs during discharge when an external load is applied to the cell. The load allows electrons to move to the positively charged cathode through the external circuit, with lithium ions moving to the cathode in response to the negative charge buildup at the electrode.

The differences in charge between the electrodes, determined by the level of lithiation in each, creates an electrochemical potential that is measured in volts. The capacity of a LIB is typically reported in ampere-hours (Ah), which refers to the magnitude of current that would completely discharge a battery from a fully charged state over the course of one hour. The charge or discharge rate applied to a LIB is often reported in terms of a unitless "C-rate," which refers to the amperage applied to a battery relative to its nominal discharge capacity. Clarifying further, if a battery is rated at 4 Ah, that means that completely discharging the fully charged battery at 4 A will take one hour. If a 2 C rate is applied, or 8 A, it will take 30 minutes to fully discharge the battery. The at-present discharge capacity of a cell relative to its maximum capacity is referred to as state of charge (SoC), which has a positive nonlinear relationship to voltage and is reported as a percentage. Figure 1 illustrates the relationship between the electrodes' and full-cell's open circuit voltage (OCV) potentials with SoC for a typical Nickel-Cobalt-Aluminum (NCA) LIB. OCV refers to a LIB's voltage at a fully rested state.

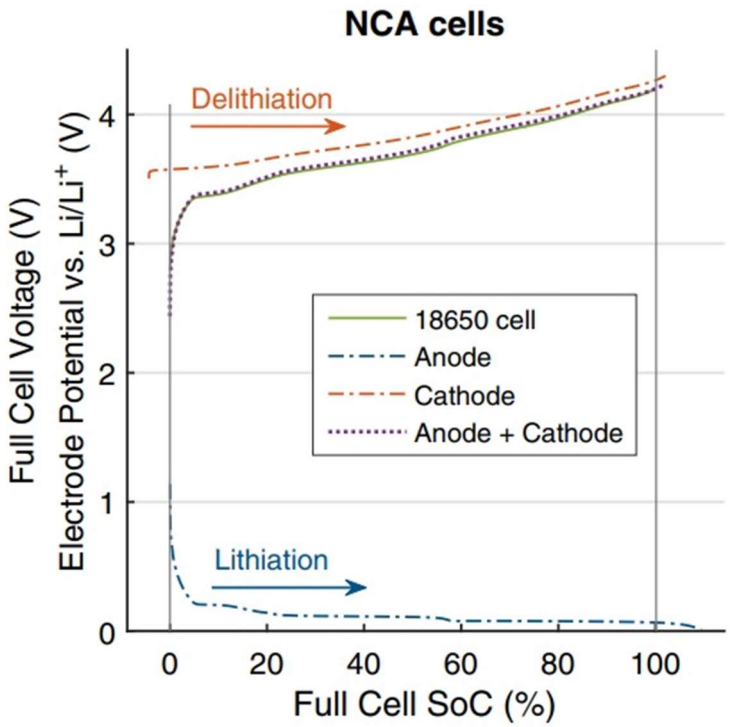

Figure 1: Nickel-Cobalt-Aluminum (NCA) lithium-ion battery electrode and full-cell open circuit voltage as a function of state of charge (SoC). Adapted from [10].

LIBs are designed to operate based on voltage ranges that maintain the stability of the electrolyte, electrodes, and other cell components. The upper and lower voltage limits are commonly referred to as charge or discharge safety cutoffs. Exceeding these limits can cause permanent damage to a LIB and may even result in serious safety incidents. The effects of overcharging or discharging LIBs is further described in section 4.1.2.3.

1.1.2 Battery Manufacturing and Assembly

Lithium is the charge carrier of choice for these batteries due to its weight (the lightest of any elemental metal) and high propensity to lose an electron, as measured by its largely negative reduction potential of -3.01 volts, which is the lowest of all elements [7], [11]–[13]. The voltage, and therefore power and energy capacity of a battery, is determined by the difference in reduction potentials between the positive and negative electrodes. The use of lithium allows LIBs to achieve high power and energy

density on a weight and volume basis compared to other electrochemical energy storage and conversion devices [4], [5].

Graphite is the commonly preferred choice of anode materials due to its low cost, abundance, and its favorable electrochemical and structural properties which allow for relatively easy lithium ion (de)intercalation while maintaining acceptable structural stability and low volume changes [8], [13], [14]. Lithium titanium oxide (LTO) and lithium metal anodes have become topics of growing interest in the literature as well. LTO anodes pose advantages due to their increased structural stability and safety compared to graphite, though disadvantages in terms of lowered lithium kinetics and energy density remain a challenge for their widespread adoption [8], [14]. In contrast, lithium metal anodes show potential to greatly increase the energy density of LIBs, though they introduce concerns regarding poor stability and safety relative to graphite anodes [15].

LIB types are often identified by their cathode materials. A varied array of lithium metal oxides are commonly used for LIB cathodes, which widely differ in key battery performance characteristics. Common elements utilized in cathodes include nickel, cobalt, aluminum, iron, and manganese [8], [13], [16]. These elements are used for and range in the ability to structurally or thermally stabilize cathode structures, provide increased electrical conductivity to produce higher power and energy density batteries, and increase battery safety [8], [13]. These characteristics, in addition to material cost, are tradeoffs considered by battery manufacturers and users when selecting cathode materials. Common battery chemistries and their relative attributes may be found in Table 1 and Figure 2, respectively.

Table 1: Common battery chemistries and their common abbreviations.

Name	Chemical Formula	Abbreviation
Lithium Cobalt Oxide	$LiCoO_2$	LCO
Lithium Manganese Oxide	$LiMn_2O_4$	LMO
Lithium Nickel Manganese Cobalt Oxide	$LiNiMnCoO_2$	NMC
Lithium Iron Phosphate	$LiFePO_4$	LFP
Lithium Nickel Cobalt Aluminum Oxide	$LiNiCoAlO_2$	NCA
Lithium Titanate (Anode Material)	Li_2TiO_3	LTO

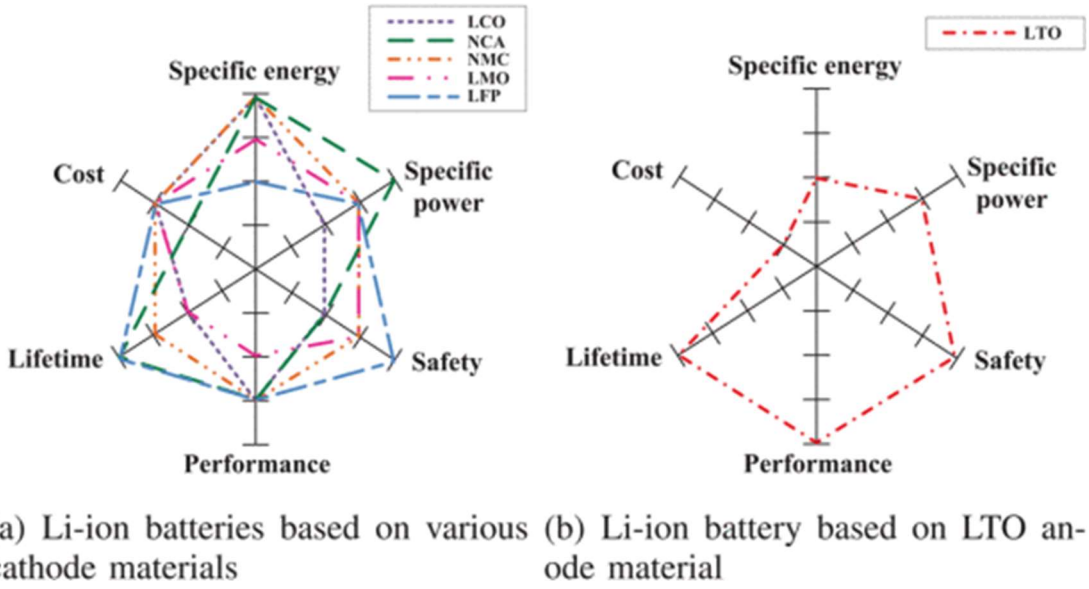

(a) Li-ion batteries based on various cathode materials (b) Li-ion battery based on LTO anode material

Figure 2: Relative characteristics of different lithium-ion battery types, synthesized and reproduced from [16].

LIBs are most commonly manufactured in the form of cylindrical, prismatic, coin, and pouch cells [8], [12]. Generally, cell components (e.g., anode, cathode, separator, current collector, etc.) are produced and stacked in many repeating sheet-like layers. These layers are then either directly encased in flexible pouches (pouch cells) or rigid flat cylinders (coin cells), or wound and placed in cylindrical canisters (cylindrical cells) or rigid rectangular containers (prismatic cells). The battery is then saturated with electrolyte and sealed [12]. The form factor of battery cells affects ease of manufacturing and pack

assembly, pack energy density, thermal management, and safety considerations of the battery cells and packs.

In order to serve the proper energy and power requirements of their end use LIBs are often connected in series and/or parallel packs, with some applications such as EVs requiring hundreds of individual LIB cells within a pack [17], [18]. Figure 3 details the main types of cell connections used in LIB packs.

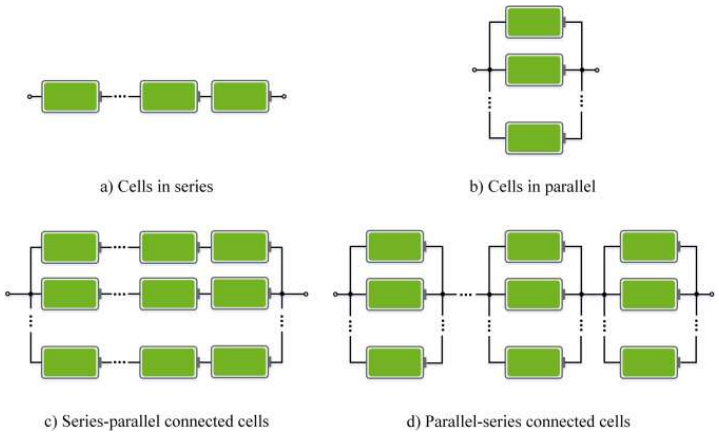

Figure 3: Four main cell connection methods. Reproduced from [18].

Kirchhoff's voltage and current laws dictate that in a series arrangement, all batteries will share the same current and the overall voltage of the assembly will equal the sum of individual battery voltages. Conversely, when batteries are placed in parallel they share equal voltages and the overall pack current is a summation of the individual battery currents. Depending on the application, different battery pack topologies may be appropriate. For instance, high current or long discharge applications may place more emphasis on increasing cells wired in parallel, while high voltage applications will utilize more series connections. The smallest unit in LIB applications is a cell, which is often wired with other cells to form assemblies called modules, which can be further connected to other modules to form battery strings and/or packs.

1.2 Applications and Future Outlook

LIBs are becoming increasingly ubiquitous in today's society due to their many applications and high volumetric and gravimetric power and energy density compared to other secondary battery types. LIBs are regularly used in a wide variety of portable electronic devices, including cell phones and laptops, as well as in electric and hybrid vehicles and large scale energy storage [19]–[21]. In terms of economic value, the global market for LIBs is expected to grow at a compounded annual growth rate of 18.5% until 2030 [19]. This is largely driven by rapid price decreases in LIBs over the past few decades (sans 2022 and 2023) coupled with a global increase of EV adoption, which is expected to continue [19]–[22].

With increased adoption worldwide comes an inherent increase in the retirement and disposal of LIBs. In the case of EV batteries, many are retired with significant remaining energy and power capacity. Dunn et al. [23] estimated EV batteries will be retired globally with a cumulative remaining capacity between 1000 and 2000 GWh in 2040. With the growth of this waste comes the opportunity for second-life LIB applications. The end of an EV battery's first-life (i.e., end of life, "EOL") is generally considered to be when the battery degrades to 80% of nominal energy or power capacity [24]–[29]. Batteries at this state of health ("SoH", see section 4.1) are often retired due to their inability to meet range or acceleration demands of EV users [30]. Stationary energy storage systems (ESSs) provide an excellent opportunity to reuse these batteries, as many ESS applications have much less physical space and weight limitations and therefore energy and power density requirements compared to EVs.

Efforts to improve the sustainability and resiliency of global energy systems is increasing the need for ESSs. Grid electrification is a key strategy policymakers are relying on to boost penetration of renewables and lower demand for fossil fuels [31]. Due to the innate intermittency of renewable energy sources such as solar photovoltaics and wind, battery-based energy storage systems will be indispensable assets to allow sporadic or diurnal energy supply to meet demand.

The high upfront cost of ESSs is one of the main barriers to their widespread adoption [32]. This crucial issue of ESS cost can potentially be addressed by the use of second-life batteries. Second-life batteries, specifically from EVs, present several advantages over new batteries for stationary ESSs. Their primary advantage is cost, with Casals et. al. [33] finding that a second-life battery pack for energy storage costs less than half as much as a similar pack made with new cells. An additional way in which second-life batteries may have a cost advantage in the future is by reducing the cost of their first life in EVs [34]. This could increase the sales of EVs, leading to an increased supply of second-life batteries and further driving down their cost [35]. Finally, the usage of second-life batteries offsets the need to produce new LIBs for applications like ESSs. Second-life energy storage is of increasing interest in LIB research, with several pilot studies already undertaken to test and prove its efficacy [36], [37]. The coinciding growth in ESS demand and second-life LIB supply offer an exciting opportunity to increase the sustainability of a renewable energy transition at reduced cost.

1.3 Battery Pack Management and Control Strategies

To ensure the safe, reliable, and cost-effective operation of LIBs, battery packs are often equipped with a number of hardware and software features that monitor and control pack operations. This network of features is commonly referred to as a battery management system (BMS), which ranges in complexity and effectiveness based on the value and nature of the LIB application. The primary purpose of a BMS is to monitor and ensure batteries are operating in a safe manner [38]–[41]. A BMS monitors the voltage, temperature, and current of a LIB pack at the cell-, module-, or pack-level. This information is compared against safe operating limits, and if any of these parameters indicate battery abuse or failure, the BMS may initiate intervention procedures (e.g., heating/cooling, electrical disconnection, (dis)charge stoppages, emergency service alerts, etc.). A BMS may also perform battery state or parameter estimations. Evaluations of SoC, SoH, power capability, and more crucially inform safe and efficient cycling procedures.

The numerous applications and substantial value of LIBs offers expanding opportunities to increase the sustainability of energy systems, usefulness of consumer products, and spur technological advancement. However, LIBs also produce substantial negative externalities over their life cycle, and the nature of current LIB technology contributes to inefficient and unsafe usage. The research outlined in this dissertation seeks to present and help address these issues.

2 Problem Definition

There are numerous negative impacts and challenges associated with the production and use of LIBs. These widely range from the financial and logistic difficulties of supplying and operating battery products to the societal and environmental costs of producing and disposing LIBs. Of the numerous issues associated with LIBs, many are critically exacerbated by poor diagnosis of battery SoH. Common examples of such issues will be briefly introduced in this section.

2.1 Unsafe and Inefficient Lithium-ion Battery Utilization

Operating LIBs while maintaining their performance and safety crucially relies on accurate diagnostics of constantly changing battery states and parameters. One of the most critical battery parameters that must be accurately identified is the SoH of a battery. Further explained in section 4.1, SoH is a key determining factor of battery performance, capability, and reliability. Improper accounting of SoH can lead to catastrophic safety failures, inefficient utilization, and decreased longevity of LIB systems.

Many of the causes of dangerous battery failure (i.e., fire and toxic gas release resulting from thermal runway) are the direct result of various battery aging features [42], [43]. Therefore, the likelihood of failure increases as batteries degrade over time. Quantifying the state of degradation is therefore essential to mitigate the risk of battery failure. Once battery SoH degrades below acceptable safety standards, a battery may be retired to avoid safety incidents. Furthermore, LIB failure modes that result

from electrical abuse (e.g., over charging and discharging) can be mitigated by accurate SoH quantification. Over charging or discharging may occur when the SoC of a battery is inaccurately calculated. The SoC of a battery is quantified in relation to battery capacity, therefore accounting for changes in battery capacity with aging is necessary for safe battery operation. Moreover, over charging and discharging increase battery degradation rates [44], which not only exacerbates safety risks, but also reduces the lifespan and utility of LIBs.

Beyond safety considerations, LIB product performance and reliability also relies heavily on accurate SoH calculation. The SoH of a battery will determine the remaining useful life (RUL) [45], power capability (i.e., “State of Power”, SoP) [46], SoC, and remaining energy (i.e., “State of Energy”, SoE) [45] of LIB products. RUL informs users and manufacturers the amount of time and the way in which a LIB may be operated before it will need to be retired. Overestimation of this may cause costly unanticipated battery performance losses or failure, while underestimated RUL could cause premature retirement of batteries. SoP, SoC, and SoE inform users of the power or energy capabilities of LIB products at a given time. Strategic battery charging and discharging procedures for products such as an ESS or hybrid electric vehicle (HEV) are severely hampered by imprecise estimations of these metrics. As a common example, in the case of an EV, SoH affects the vehicle’s anticipated lifetime (i.e., RUL), acceleration capability (i.e., SoP), range (i.e., SoC, SoE), and more. The problems arising from SoH estimation errors are numerous, and could cause users significant travel delays, reduced investment value, and overall product dissatisfaction.

With the consequences of improper SoH estimation in mind, the current state of LIB health monitoring in research and practice is ripe for improvement. For instance, in a study evaluating the accuracy of Nissan Leaf BMSs, differences between direct current measurements and those read by the vehicle BMS would attribute capacity estimation differences of up to 1.4% for a 2020 model [47]. Unfortunately, more studies validating commercially used EV BMSs are rare, as manufacturers maintain secrecy of their

proprietary battery monitoring procedures [48]. Mobile devices like cell phones have been known to offer poor SoH estimation in practice. Widespread complaints of sudden shutoffs when phones were showing 10-30% remaining charge caused manufacturers like Apple to offer free battery replacement programs in the past [49]. Some Android phones have been shown to lack even moderately accurate SoH estimation ability, reporting to users their batteries were still in "good health" at 25% SoH [49], [50]. Based on the computation or conditions required of SoH estimation methods, health monitoring has been significantly limited in these devices. Section 4.1.4 will detail common SoH estimation procedures, many of which require excessively large data sets, burdensome computation, or expensive specialty equipment. Accurate and accessible SoH estimation procedures are of paramount importance for proper battery management.

2.2 Lithium-ion Battery Life Cycle Issues

While LIBs are touted as playing a key role in mitigating fossil fuel usage and its associated impacts (e.g., climate change, air quality, etc.) via transportation and grid electrification [51], [52], the life cycle environmental and social impacts of LIB production and disposal are significant. The mining and processing of common LIB raw materials like lithium and cobalt are associated with considerable environmental degradation [51], in addition to abusive labor practices directly associated with the sourcing of these materials [53]. Solely in terms of energy input, the production of a single LIB requires 328 times the amount of energy than the battery itself can store [54]. Following retirement, LIB waste may cause serious environmental damage due to their environmentally toxic components and propensity to explosively combust [55]. Increasing LIB demand coupled with low recycling rates [56] of LIB waste means that these impacts will grow over time as more batteries are manufactured, used, and disposed of globally. Aforementioned issues with lifespan reduction and premature battery retirement associated with poor SoH estimation accuracy is therefore an imperative problem to address to reduce the need for new LIB production.

Though the problems accompanying the premature retirement or need for new LIB production may be alleviated through the reuse of retired batteries, there are many technical barriers that make second-life LIB applications prohibitively challenging. These include unknown usage history, lowered SoH, higher internal resistance, long reassembly time, and increasingly strict standards for battery reuse (e.g., UL 1974). Before any reassembly and reuse can begin, it is vital to accurately characterize the batteries in terms of their SoH, internal resistance, and physical integrity. This ensures that battery packs can be assembled and operated in a way that maintains optimal battery performance, safety, and remaining lifespan. Accurate SoH measurement of a single battery cell or module can require excessive amounts of time and resources. Anecdotally, it took over 10 hours to measure the SoH of each individual Nissan Leaf module repurposed for the ESS assembled by Lacap et al. 2021 [37]. Considering their ESS was composed of 864 modules, a subset of all modules tested, the process of ESS assembly was exceedingly laborious. If second-life batteries are to become more widespread, the process of SoH estimation following first-life retirement must be significantly expedited.

3 Research Objectives and Motivation

Overall, the primary objective of the research described in this dissertation is to provide a methodology to rapidly and accurately estimate battery pack SoH. For reasons outlined above and further expounded upon in Part II, SoH is one of the most vital parameters to understand for a battery. The SoH of a battery is a core determining factor in how it behaves under load, its capabilities to serve energy and power requirements, and its reliability in terms of safety and performance over time and usage. However, it can be difficult to accurately diagnose depending on the LIB application and available resources.

The motivation of this research is to address the issues outlined in section 2, which describe the consequences of inaccurate SoH estimation. By presenting a proven and reproducible methodology for

accurate rapid SoH estimation, this research hopes to provide a guide for battery researchers and providers to create useful and effective LIB SoH diagnostic tools. The success of this study, therefore, will contribute to accomplishing the following objectives:

1. Ensure the safe usage of LIBs
2. Improve efficient utilization of LIBs
3. Reduce LIB supply chain-related externalities

Advancements towards any one of these objectives would significantly increase the environmental, social, and economic value of LIB products.

This dissertation seeks to provide novel advancements in the study of LIB diagnostics. Part II will include a summary of the current state of literature along with critiques regarding the gaps and shortcomings of current pack SoH estimation methods. Major deficiencies in the literature are addressed in later parts with computationally expedient modeling of LIB SoH at the pack level.

Part II. Literature Review and Theoretical Approach

4 Theoretical Background and Relevant Literature

4.1 Battery State of Health

4.1.1 Defining State of Health

Battery aging (i.e., degradation) is an inevitable process that begins the moment a LIB is manufactured and continues throughout its lifespan. The SoH of a battery is a metric used to define the remaining capabilities or state of a battery following degradation. There is no standard definition of SoH, though it is usually defined as a ratio between the at-present parameters of a LIB compared to its nominal values and is reported as a percentage [57]. Most commonly, it is defined in terms of the remaining capacity of a battery cell compared to the manufacturer's rated capacity. The loss of battery capacity due to aging is referred to as capacity fade. Many other SoH definitions can be found in the literature, which include battery parameters such as internal resistance, impedance, cyclable lithium ions, diffusion rates, and more relative to their nominal values [29], [58]–[60]. Over time, battery degradation generally leads to an increase of battery impedance and internal resistance, limiting the power that a cell is capable of producing (or receiving via charging). The decrease in power capability of a cell is referred to as power fade, and is often simply identified in terms of an increase in battery impedance or internal resistance instead of a direct measurement of cell power capability. Equations 3 and 4 show frequently used calculations for cell SoH quantification in terms of capacity and internal resistance, respectively:

$$Cell\ SoH\ (\%) = \frac{Q}{Q_r} \times 100\% \tag{3}$$

$$Cell\ SoH\ (\%) = \frac{IR_{EOL} - IR}{IR_{EOL} - IR_r} \times 100\% \tag{4}$$

Where Q is defined as the capacity of a cell in Ah, Q_r is the nominal or rated capacity, IR is the current internal resistance, IR_{EOL} is the internal resistance at end of life, and IR_n is the nominal internal resistance of the battery cell.

Defining battery pack SoH is much less straightforward than at the cell level, though is generally defined using the same parameters as cell SoH (e.g., capacity, internal resistance, etc.). The added complication to characterize pack SoH is for several reasons, including variation between cells (see section 4.2), pack power and energy capabilities often being limited by the weakest cells, and overall complexity being introduced by cell-to-cell connections and interactions. Bi et al. [25] treated a battery pack as a singular lumped system, where pack SoH was defined by equation 4 using the overall pack internal resistance. A frequently applied method defines pack SoH based on the voltage or current-limiting individual cell(s) within a pack [61]–[63]. These metrics are reflected in equations 5 and 6 in terms of the capacity (Q) and internal resistance (IR) of the jth cell, where N_p is the total number of cells in a pack. Pack SoH may also be defined by the average SoH of cells within a pack, as shown in equation 7 [62]–[64]. Determination of which cell or cells determine overall pack capacity depends on several factors, including pack topology and any voltage equalization measures employed. This concept will be further discussed in section 4.2. Diao et al. [65] defined pack SoH using equation 8 in terms of the maximum available energy of pack (E_A) relative to the nominal total energy (E_{MO}). They defined E_A for each cell based on integrating the

open circuit voltage (U_{OCV}) multiplied by the current (I) over the whole SoC range and subtracting joule heating losses. E_{MO} for each cell was summed and defined by the average OCV of each cell over the entire SoC range multiplied by cell nominal capacity. Zhang et al. [66] defined pack SoH using equation 9 in terms of pack maximum energy storage (E_{PMES}) relative to its nominal value. E_{PMES} was calculated based on the summation of remaining maximum charge and discharge energy of each cell, integrating cell capacities multiplied by their OCV over the operating SoC range. Regardless of how cell or pack SoH is defined, the health of LIB systems must be accurately identified in order to ensure their safe and efficient management. The following discussions will describe the sources and implications of battery degradation and the current state of literature regarding SoH estimation.

$$Pack\ SoH\ (\%) = \min_{1 \le j \le N_p} (SoH_{Q,j}) \tag{5}$$

$$Pack\ SoH\ (\%) = \max_{1 \le j \le N_p} (SoH_{IR,j}) \tag{6}$$

$$Pack\ SoH\ (\%) = \frac{\sum_{j=1}^{N_p} SoH_{Q,j}}{N_p} \tag{7}$$

$$Pack\ SoH(\%) = \frac{E_A}{E_{MO}} = \frac{\sum_{j=1}^{N_p} \int_{SoC_j=0\%}^{SoC_j=100\%} U_{OCV}(t) \cdot I \cdot dt - \int R_j \cdot I^2 \cdot dt}{\sum_{j=1}^{N_p} Q_n(j) \times U_{OCV}|_{SoC=[0,100\%]}} \times 100\% \tag{8}$$

$$Pack\ SoH\ = \frac{\sum_{j=1}^{N_p} \int_{SoC_{t_1}^{j}}^{SoC_t^j} C_j U_{OCV,i}(SoC) dSoC + \sum_{j=1}^{N_p} \int_{SoC_t^j}^{SoC_{t_2}^{j}} C_j U_{OCV,i}(SoC) dSoC}{E_{PMES_n}} \quad (9)$$

4.1.2 Common Sources of Battery Aging

Battery aging occurs due to various physical and chemical side reactions that occur inside a LIB cell. The battery degradation literature broadly attributes the internal aging mechanisms of LIBs to two main aging modes: loss of lithium inventory (LLI) and loss of active electrode material (LAM) [44], [67]–[70]. Less discussed aging modes are also identified in the literature, including loss of electrolyte and further specification of LAM modes like loss of contact between electrodes and current collectors, loss of mechanical stability of electrodes, as well as cathode or anode-specific aging. LLI refers to a loss of cyclable lithium that participates in the intercalation and charge transfer processes that govern battery operation. LLI therefore directly causes capacity fade in LIBs. LAM refers to the reduction in electrode sites that can participate in these same reactions. LAM at either electrode can lead to both capacity and power fade. Han et al. [71] offered a useful analogy in conceptualizing LLI and LAM, likening LIB charging and discharging to the exchange of water between tanks. The intercalation and deintercalation of lithium ions between electrodes during cycling are analogous to pouring water (i.e., lithium ions) from one tank (i.e., electrode) to another back-and-forth. LLI is compared to a loss in water that can be transferred from tank-to-tank, while LAM is equated to a loss in tank volume.

4.1.2.1 Typical Cycle Aging

As a consequence of lithium ion insertion and extraction, electrode materials experience physical deformations and volume changes that lead to both capacity and power fade. The repeated swelling and contraction of the anode and cathode cause mechanical stress and ultimately damages the structure of electrode materials, leading to LAM. Structural changes to the electrodes can cause cracking, loss of

contact between the electrode and current collectors or internal binding agents, and reduce the ability for lithium transport through the bulk material through porosity changes [44], [72], [73]. Due to these concerns, special care is taken when selecting electrode materials that maintain their structural integrity over repeated cycling. Anode materials like graphite and LTO are often preferred due to their low volume changes and stability, with graphite experiencing approximately 10% and LTO negligible change in volume during cycling. In comparison, silicon anodes may experience 300-400% volume change; a major barrier to widespread adoption that researchers are attempting to address [44], [67], [71], [73], [74]. Cathode materials like NMC and LFP have long cycle lives due to their limited volume changes of approximately 2% and 7%, respectively, during charging and discharging [75], [76]. The addition of doping agents and combinations of cathode materials are an area of research interest in the LIB literature to increase the mechanical stability of electrode materials.

During the first few charge and discharge cycles following fabrication, a LIB undergoes rapid aging effects at the anode due to the formation of a passivation layer called the solid electrolyte interphase (SEI). The SEI forms due to electrochemical instability between the anode material and electrolyte, shown in Figure 4, causing side reactions and a reduction of the electrolyte. This reduced product forms the SEI film that coats the surface of the anode. SEI formation causes significant consumption of lithium ions (i.e., LLI) and electrolyte and is a relatively immediate and irreversible process [67], [77], [78].

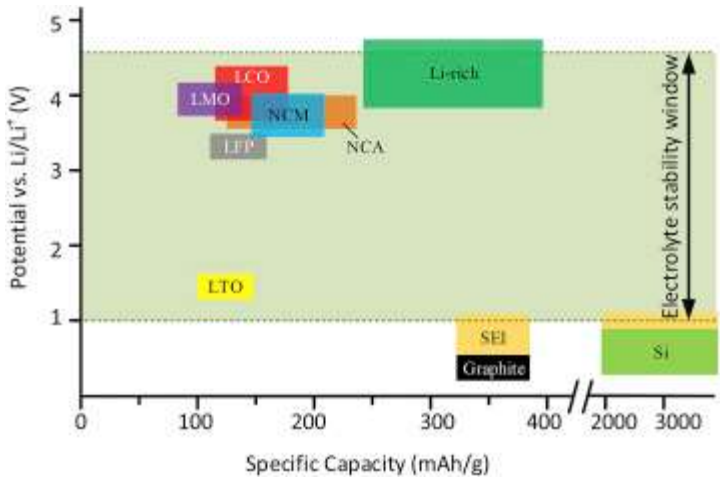

Figure 4: Electrochemical potential of common lithium-ion battery materials. The stable electrochemical potential range of common lithium-ion battery electrolytes shown. Reproduced from [67].

Once formed, the SEI serves as an imperfect passivation and semi-permeable layer that electrically insulates the anode and usefully prevents electrolyte permeation while simultaneously allowing for lithium ion transport into the anode. This protects the electrolyte from further reduction. Imperfections in this layer along with SEI cracking from physical deformation due to volume changes exposes the electrolyte to the lower voltage potentials at the anode, causing a thickening of the SEI over time, though at a much lower rate than initial formation [44], [67], [71], [78], [79]. The SEI layer can also cause LAM in the anode. SEI formation may cause gas formation, which can lead to mechanical stress, cracking, and exfoliation of the anode material [44], [78], [80]. This can expose the anode to the electrolyte, cyclically leading to further SEI formation and continued LLI and LAM. In addition, SEI layers are a source of internal resistance in the cell, which induces joule heating, leading to an Arrhenius-driven acceleration of SEI formation and other side reactions within the cell. SEI growth is also accelerated at high SoC. This is due to accelerated side reaction rates when anode voltage potential is low. The LLI, LAM, and internal resistance rise associated with SEI formation and growth is a source of both capacity and power fade.

4.1.2.2 Calendar Aging

Even when left idle, LIBs degrade over time due to a process called calendar aging. Calendar aging is commonly attributed primarily to SEI growth that occurs independent of battery cycling [10], [81]–[83]. The rate of calendar aging, therefore, is determined by the relationships between SEI growth rate and battery storage conditions. Schimpe et al. [84] produced a study that tracked the degradation of stored idle batteries under different SoC and temperature conditions. Their results showed that LIBs degraded faster as both storage SoC and temperature increased, independently. The inevitability of calendar aging ultimately means that degradation is always occurring in the background of any LIB experiment and merits consideration. To be truly accurate, studies that evaluate degradation rates over a number of charge and discharge cycles should also consider the amount of time elapsed during testing. For example, studies comparing the effect of C-rates on battery aging over a set number of cycles should consider that batteries cycled under high C-rates will reach more cycles in less time than those cycled at lower currents. In order to isolate the effects of C-rates on degradation rates, calendar aging effects should be taken into account.

4.1.2.3 Cycle Aging Acceleration Factors

The degradation sources due to cycling described thus far are merely a subset of the many ways in which LIBs age under normal usage. These sources along with others may be significantly exacerbated or introduced depending on harsher or more abusive environmental and cycling conditions. These cycling conditions are detailed in the following subsections.

High Temperatures

While there are some benefits to increased environmental and internal temperatures for batteries, including temporary lowered internal resistance and therefore increased power and energy capacity [85]–[88], these gains come at the cost of increased degradation rates and likelihood of battery failure

[44], [78], [85], [88]–[98]. The increased power and capacity fade rates of LIBs cycled under elevated temperatures can be attributed to changes in both electrodes and decomposition of electrolyte and other battery constituents like binding agents. However, higher degradation rates at elevated temperatures are mainly attributed to an Arrhenius-driven increased rate of SEI formation. Post-mortem studies like those conducted by Waldmann et al. [93] support this widely accepted dominant aging feature at elevated temperatures. Most studies looking at degradation rates at high temperatures, therefore, focus on aging in the anode. Cathode aging may also be increased at elevated temperatures as well, however. Situ et al. [85] imaged NMC cathode materials and found the batteries cycled under elevated temperatures showed damage to their crystalline structures. The damage was identified to hinder lithium insertion and extraction, and therefore power and energy capacity, and also weakened the future mechanical and thermal stability of the electrode.

Low Temperatures

Low temperature cycling of LIBs creates its own set of problems. While high temperature cycling increases electrochemical reaction rates, low temperature cycling significantly decreases reaction rates within the cell. Low temperature conditions increase the internal resistance within the cell. Charge transfer resistance at the electrode surfaces increases, diffusion rates into electrodes and through the electrolyte decreases, and overall ionic conductance and kinetics within the cell are lowered. Not only does this lead to temporary decreases in energy and power capacity, it also triggers irreversible aging processes.

A major aging mechanism attributed to low temperature conditions is lithium plating [44], [67], [89], [93], [94], [96]–[103]. Lithium plating occurs at low temperatures due to the slow diffusion of lithium ions into the anode bulk material. If charging conditions cause lithium to diffuse from the cathode to the anode surface faster than the ions can diffuse into the anode bulk material, an accumulation of lithium

ions at the surface of the anode will occur. If this accumulation remains too high for too long, two different plating mechanisms may occur [104]–[110]. Firstly, an accumulation of lithium ions at the surface of the electrode can cause local anode potentials to drop below the equilibrium potential where Li^+ reduces to lithium metal. Alternatively, and this is considered less common, the concentration of lithium ions at the anode surface may cause a local oversaturation in the graphite, causing lithium metal to deposit onto the electrode surface. These reactions cause a portion of reversible and irreversible LLI and LAM. In addition, the deposited lithium metal may react with the electrolyte, causing electrolyte consumption and both SEI growth and anode damage, leading to further LAM. Lithium plating may also lead to dangerous conditions within the cell, including the growth of dendrites due to repeated lithium metal deposition. Dendrite growth can lead to catastrophic battery failure if lithium metal dendrites grow too large and puncture the cell separator [111]–[113]. Low temperatures also lead to material embrittlement [67]. This can create significant damage to electrode structures, SEI layers, and other parts of the cell when the cell undergoes volume changes during operation.

Temperature dependent aging mechanisms have been extensively researched in the LIB literature. The ideal temperature at which to cycle a LIB is dependent on cell chemistry, charge and discharge rates, SoH, and more [89], [93], [94]. Studies consistently show that based on these variables, there does exist an ideal “crossover” temperature in which aging is minimized. Anything greater than that temperature accelerates aging primarily due to increased SEI growth rate. Anything below the crossover temperature increases aging mainly due to lithium plating mechanisms.

Overcharging

Overcharging a battery can cause significant safety concerns and rapid power and capacity fade. Overcharging is defined as applying (or continuing to apply) a charging current to a battery after it has reached its upper safety voltage cutoff limit. During overcharge, both electrodes experience abuse; the

anode becomes overly lithiated and the cathode becomes overly delithiated. It bears mentioning that when a battery reaches 0% SoC and 100% SoC, neither electrode is ever fully delithiated (i.e., electrodes still contain a relatively small concentration of lithium ions). These small concentrations of lithium ions are by design and maintain the structural and electrochemical integrity of the anode and cathode [114]. Lithium concentrations outside of the 0% to 100% SoC design window may cause significant damage to either electrode.

Overcharging results in heat generation, which helps catalyze other overcharging-induced degradation mechanisms as well [115]–[120]. The sources of heat include joule heating from the significant rise of internal resistance at extremely high SoC (>100%) and exothermic side reactions that occur at both electrodes. Excessive delithiation of the cathode causes various side reactions and structural changes. High SoC or overcharge conditions may lead to electrolyte reduction and LAM via the dissolution of transition metals (e.g., Mn, Co, Ni) due to high voltage potentials [121]. The resultant metal ions from the cathode have been shown to migrate and merge with the SEI layer on the cathode. Dissolution reactions may produce oxygen and heat, leading to more electrolyte oxidation and eventually thermal runaway. The dissolution of transition metals along with overall instability from extreme delithiation cause irreversible structural change to the cathode, causing LAM as well [67], [115], [116], [118], [119].

Excessive lithiation of the anode creates conditions that slow the diffusion of surface lithium ions into the bulk electrode, leading to lithium plating [67], [108], [115]–[119], [122]–[124]. Plated lithium at high temperatures may then react with electrolyte and further release heat and gas. Based on the various reactions that produce heat and gas in both the anode, cathode, and electrolyte, thermal runaway is a significant hazard associated with overcharging LIBs.

Over Discharging

When batteries are discharged past their lower safety voltage limits, aging mechanisms are accelerated in the overly lithiated cathode and delithiated anode. The abnormally high voltage potential on the anode side of the cell (see Figure 1) causes the copper current collector (the most common choice of anode current collector material) to oxidize. Positively charged copper ions resulting from this corrosion may then diffuse through the electrolyte, deposit onto the cathode and form dendrites. These dendrites may grow over time and puncture the cell separator, leading to an internal short circuit and subsequent thermal runaway. Overly high voltage potentials in the anode also leads to SEI decomposition. This process generates gasses that can damage cell structures and also exposes the graphite to electrolyte causing future SEI formation-induced degradation [125]–[131]. Extreme lithiation at the cathode may cause severe and permanent structural change. An overabundance of lithium ions inserted into the cathode has been shown to cause irreversible amorphization of the crystalline cathode structure, causing LAM [125], [132].

High Current Cycling

While high current cycling may be useful for various applications requiring high power or short charge times, it negatively affects LIB health. The ohmic voltage jumps from high currents lowers the usable energy capacity of a battery, as upper or lower safety voltage cutoffs are reached sooner during cycling. High C-rates also accelerate and introduce various battery aging mechanisms throughout the entire LIB cell. Ohmic voltage jumps may sustain batteries at very high or low voltages during cycling, inducing aging mechanisms associated with high or low voltage potentials. High currents also directly increase internal temperatures within the battery via ohmic heating. Increased side reaction rates and other temperature-associated degradation mechanisms previously discussed are therefore also introduced [67], [133].

As lithium ions are intercalated and deintercalated at accelerated rates, the rapid change in volume and inhomogeneous lithium concentration throughout the bulk electrode materials induces substantial mechanical stress that can lead to cracking (causing new SEI growth or contact loss) and distortions in anode and cathode structures. In addition, high surface concentrations of lithium ions that accumulate faster than they can diffuse into the anode can result in lithium plating [44], [67], [98], [105], [106], [110], [134]–[137].

High Depth of Discharge

Depth of discharge (DoD) refers to the SOC range under which a battery is operated. For instance, if a cell is cycled between 20% SoC to 80% SoC, its DoD for the cycle is 60% (80%-20%). High DoD causes accelerated LIB aging relative to lower DoD for several reasons [94], [98], [134], [138]–[141]. Firstly, a larger DoD means more lithium ions are being inserted and extracted from the electrodes, inducing greater volume change-related aging mechanisms. Secondly, a larger DoD means both higher and lower voltages and the ends of the SoC operating window. Degradation processes that trigger at particularly high or low electrode voltage potentials (see calendar aging, overcharge, and over discharge discussions) start to present at larger DoD. This also means that not only is the degradation of a LIB dependent on DoD, but also the midpoint of its SoC operating window. For example, two batteries operated at the same DoD of 60% will degrade differently if the SoC window is from 0-60% SoC than 40-100% SoC.

Overall, LIB aging is an incredibly complicated and dynamic nonlinear process that has still yet to be fully understood. The large network of interdependent variables that affect degradation rates and mechanisms often form complex positive feedback loops. For instance, high charge rates may cause anode and SEI cracking, which in turn leads to further SEI growth and subsequent gas and heat production, which then leads to electrode strain and faster side reactions and so on. The extent to which different degradation modes are introduced and affect overall battery performance and lifespan varies

considerably based on LIB chemistry, quality, SoH, and much more. The discussion in this section is merely a cursory review of the most commonly identified and understood LIB degradation modes and processes in the literature. As a rule of thumb, operating batteries under low currents, mild ambient temperatures, and low DoD is a widely accepted practice to increase the performance and lifespan of a battery. This is well demonstrated by Wang et al. [139], who cycled LFP batteries under various temperatures, DoD, and C-rates until they were degraded to EoL conditions.

4.1.3 Battery Aging Over Time

Barring any extreme or prolonged battery abuse conditions like those discussed above, the rate of degradation of a battery is often described in discrete linear and nonlinear phases [67], [81], [94], [142]–[149]. At the very beginning of battery life there is a period of rapid nonlinear capacity and power fade attributed to initial SEI formation. This phase is incredibly important for the longevity of the battery and initial cycling is typically performed by the manufacturer. The initial cycling procedures and conditions will determine the robustness and stability of the first SEI layers to passivate the anode surface over the lifespan of the battery [78]. Following this formation period, the battery will enter a phase of quasi-linear capacity and power fade. During this phase the SEI slowly grows over time, causing electrolyte consumption, LLI, and LAM.

Finally, the cell reaches an aging inflection point, where the rate of capacity and power fade increase dramatically and nonlinearly. This inflection point is often termed the point of “sudden death” or “rollover,” and the capacity loss and internal resistance rise curves see a respective “knee” and “elbow” point [147], [150], [151]. These points are often when batteries are considered to have reached EoL. Battery rollover is mainly attributed to a critical level of SEI growth that creates conditions for lithium plating [81], [98], [143], [148], [152]. Over time SEI growth reduces the porosity of the anode and increases the internal resistance of the cell, resulting in reduced lithium diffusion kinetics. The slowing

ionic intercalation eventually reaches a tipping point that causes lithium plating to occur. The plated lithium metal reacts easily to reduce the electrolyte and generates more anode film growth and subsequent pore clogging and internal resistance rise. A positive feedback loop forms, creating exponential power and capacity fade. Other studies have also attributed this rapid aging period, at least partially, to critical levels of electrolyte, contact loss, electrode mechanical strain, or dissolution of electrodes [146], [149], [150]. This characteristic transition from a slow, approximately linear, capacity and power fade to rapid nonlinear aging is demonstrated in Figure 5.

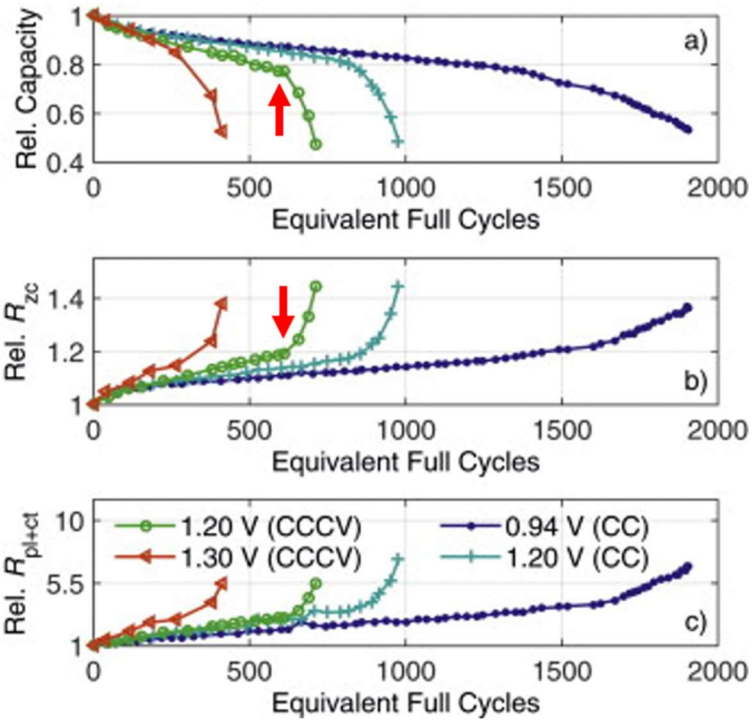

Figure 5: (a) Capacity fade and (b,c) resistance rise plots over battery cycling. Each line refers to different cycling current conditions. Adapted from [98], arrows have been added to demonstrate capacity fade "knee" and internal resistance rise "elbow" points. (b) Shows the ohmic resistance rise and (c) shows the resistance associated with passivation layers and charge transfer resistance.

Figure 5 underscores the close relationship between the internal ohmic resistance and battery capacity fade. Throughout the life of a LIB, this relationship maintains a strong linear relationship. Bao et al. [153] quantified the strength of this relationship in NCA cells and found a Pearson's correlation coefficient, ρ (see section 5.2), of 0.88. Chen et al. [154] performed similar analysis on NMC cells, with a calculated a

value ρ of 0.98. This strong linear relationship between capacity fade and ohmic resistance rise holds true for LFP cells as well [155], [156].

4.1.4 SoH Identification and Modeling Procedures

Considering the effects of degradation in limiting the safety, longevity, and capabilities of LIBs, it is vitally important to have the ability to accurately identify battery SoH. While battery SoH in terms of capacity or internal resistance can be directly measured, the process for doing so is often prohibitively time consuming or unavailable for many battery applications. It is often the case that SoH must be estimated from the limited amount of data commonly acquired by a BMS, such as current, temperature, and voltage. SoH estimation may be done in an online or offline manner. Offline estimation refers to contexts in which the battery is not under use, such as in a laboratory or at-rest setting. Online estimation occurs during battery operation, and parameter estimations are updated frequently based on battery load and usage conditions. Online estimations are especially favored for highly transient battery parameters like SoC and voltage. In comparison, slow changing battery states like SoH certainly benefit from online estimation, but the rate required for updated estimates is less crucial and therefore offline estimation may suffice.

SoH models vary considerably in accuracy and complexity, and depending on the required resolution of estimations for LIB end uses, different approaches may be appropriate. The general assumption is that battery models operate based on an inexorable tradeoff between high fidelity estimation and computational expediency [157]. Depending on the battery application, the appropriate balance between the two at-odds sides must be considered. In an EV application, for instance, a BMS must track the voltage of each cell placed in series to avoid exceeding safe operational limits [158]. The vast number of cells constituting EV packs therefore incurs significant computational burden for a BMS with limited computing power. Simultaneously, accurate SoH estimation is required for proper vehicle

maintenance, range estimation, and allowable acceleration. The requirements and limitations of battery systems like EVs creates imperatives for researchers to find modeling methods that produce SoH estimates at optimal frequency, accuracy, and computational complexity. The following discussion will describe common SoH identification procedures presented in the literature, as well as provide practical context to their usage.

4.1.4.1 Battery Testing Procedures for SoH Estimation

Coulomb and Ah Counting

One of the simplest methods to identify SoH is ampere-hour or coulomb counting. These methods involve a full battery discharge and recording the amount of charge removed by integrating the current over time [159]. The available capacity of a battery is dependent on factors such as discharge rate and temperature [160], so it is advisable to perform counting procedures at the same conditions used to originally rate the capacity of a battery for accurate comparison. Capacity fade may then be identified by comparing the capacity of a battery to its manufacturer-identified nominal capacity. This method is simple and easy to implement in an offline setting. However, error may be introduced depending on the quality of current measurements, and complete charge and discharge procedures at rated conditions are often unavailable in online settings.

Incremental Capacity and Differential Voltage Analysis

Incremental capacity analysis (ICA) and differential voltage analysis (DVA) are frequently used SoH estimation techniques that can be used to identify specific degradation modes. The basis of these analyses focuses on battery voltage change over ranges of SoC during cycling. The derivative of the battery voltage curve as a battery charges or discharges creates identifiable features that can be used to detect various internal battery characteristics. ICA looks at the change in charge or discharge capacity over the change in voltage (dQ/dV), whereas DVA focuses on the inverse (dV/dQ). Plateaus in the SoC-

OCV curve of a battery indicate a large change in incremental capacity relative to its resultant voltage change. These plateaus therefore create conspicuous features (i.e., large “spikes”) in incremental capacity (IC) curves. The shape, placement, and spacing between these features has been shown to correlate with LLI, LAM of either electrode, and other internal cell attributes [69], [161]. In an online application, the registering of large voltage changes as a function of applied current (or vice versa) may be used to estimate SoC, SoH, SoP, and more. The main benefits of the ICA and DVA methods include highly accurate SoH estimation and the ability to identify specific degradation pathways. These methods, however, are often very time consuming. The derivatives of voltage curves are highly sensitive to measurement noise and low current cycling and data smoothing is often required to produce functional ICA and DVA curves, limiting the ease of online usage [24], [57], [162].

Electrochemical Impedance Spectroscopy

Electrochemical impedance spectroscopy (EIS) is a common battery testing method used to characterize battery health. Testing includes the application of a wide spectrum of AC frequencies to a LIB and measuring the response. Most commonly, a constant voltage is applied at varying frequencies and the current response of the battery is measured [163]. A phase shift of the current response is used to indicate various battery aging features. EIS analysis is usually performed using a Nyquist plot, which deconstructs the battery impedance spectrum in terms of the resistive and reactive components. The impedance is defined by a complex number, and therefore the resistive and reactive components are plotted along a real and an imaginary axis, respectively.

Features of a Nyquist plot such as the placement and shape of the curves may directly identify battery parameters such as ohmic resistance or be used to create battery equivalent circuit models (ECMs, which are described in section 5.4) [163]. EIS results can also suggest specific internal aging pathways such as SEI growth or the slowing of ion diffusion [164]. The abilities to provide accurate non-destructive

battery characterization and specify degradation sources are major advantages to EIS. The disadvantages of the technology include high costs associated with testing equipment as well as long testing procedures [24], [162], [165]. EIS is also primarily performed at steady state conditions, limiting online applicability [166].

Pulse Testing

LIBs exhibit complex nonlinear voltage behaviors in response to applied current, as further discussed in section 5.4. The voltage response of batteries is a function of numerous internal and external battery parameters, including SoH. Current pulse profiles are frequently used to elicit LIB voltage responses that indicate internal battery states [57], [167]–[172]. Pulse testing procedures can be a rapid and easy to implement to characterize simple parameters like the internal resistance of a battery, but produce limited information regarding specific degradation mechanisms. Pulse testing trades the sophistication and resolution of measurement techniques like ICA and EIS for ease of implementation and more heuristic solutions to battery characterization. Methods like coulomb counting, ICA, or EIS may require testing times of several hours, whereas some of the most common pulse testing profiles operate in the order of minutes or seconds [57], [169]–[172]. Results from pulse testing can be applied to a diversity of model types to produce accurate online or offline SoH estimation. The tradeoffs inherent to pulse testing have led researchers to focus on pulse profile optimization to achieve maximum accuracy of resultant models while still maintaining the advantages of these techniques [173]–[176].

4.1.4.2 Modeling Approaches

Ultimately, data gathered from the testing procedures described thus far needs to be processed and applied to models to assign useful meaning to results. SoH modeling practices used in the literature can be loosely classified into three broad categories: empirical, adaptive-filtering, and data-driven methods.

These methods are often used in concert with one another to effectively produce estimations of battery SoH.

Empirical Models

Empirical models involve a range of approaches for utilizing battery test data to estimate SoH. They often use data- or curve-fitting techniques with battery test results to derive parameter values for pre-defined model structures. Common categories of empirical models include statistical, physics-based electrochemical, and equivalent circuit models, which may be used in combination. Statistical SoH models identify statistical relationships between SoH and properties of test data. Once statistical relationships are identified, they may be leveraged to create empirical equations to produce SoH estimates from future test data. More information regarding basic statistical modeling procedures can be found in sections 5.1 and 5.2. Statistical models may be applied to ICA, EIS, and pulse test results. For instance, Zheng et al. [177] used statistical analysis to quantify a relationship between battery capacity and the distance between ICA curve features to create a capacity estimation equation. Zhang et al. [178] estimated ECM parameters from EIS measurements using statistical regression equations. The estimated parameters were then further analyzed to create a probabilistic SoH model. Hu et al. [179] applied the hybrid pulse power characterization (HPPC) profile, a commonly used pulse test for LIB characterization, to create a probabilistic SoH model based on voltage sampling entropy. Another major advantage of statistical battery models is that they can quantify and control for the interactions of multiple parameters with model input data, like temperature and SoC, to maintain SoH estimation accuracy [180]–[182]. Overall, statistical modeling is a powerful tool that can produce accurate SoH estimations and identify relationships between external battery behaviors and internal aging processes.

Physics-based electrochemical SOH models focus on the internal processes that govern battery behavior and how they would theoretically evolve due to aging. These models usually rely on partial differential

equations and range significantly in granularity, from describing a LIB electrode as a single particle [183], to quantifying lithium diffusion rates in electrolyte [184]. The benefit of electrochemical modeling is that it provides direct physical understanding of internal battery aging processes. However, these models generally require significant computation and a large number of parameter assumptions and optimization. This limits their online SoH estimation ability significantly and also leads to overfitting concerns [27], [185], [186].

Basic ECMs used widely throughout SoH estimation literature are described in section 5.4. The basis of these models is to usefully analogize a LIB as a combination of simple circuit elements, such as resistors and capacitors. The equivalent circuit helps describe the complex voltage evolution of a LIB resulting from applied current. Circuit parameter values, like resistance and capacitance, are usually calculated based on an optimized fitting of empirical voltage data. Calculated parameter values change as a battery ages and may therefore be used to estimate SoH [165], [181], [187], [188]. The value of certain circuit parameters is often attributed to internal battery processes, but in a much more indirect or vague manner than electrochemical models. While the complexity of ECMs can range significantly, they are generally considered to be moderately accurate and computationally expedient SoH estimation methods with easy online applicability [162], [186]. The accuracy of ECMs, along with other empirical modeling methods, may be enhanced with the addition of adaptive filtering methods.

Adaptive Filtering Methods

The complexity and continuous nature of battery degradation makes accurate SoH estimation a challenging task. Adaptive filters are widely used for SoH estimation to allow for updating estimations as more data becomes available. Among the most common adaptive filters used for battery modeling is the Kalman filter and its variants, such as an extended or unscented Kalman filter[38], [57], [58], [162], [185], [186]. Current and voltage sensor noise that is inherent to battery model input data makes

stochastic methods like Kalman filters advantageous in creating accurate SoH estimates. The basic operations of a regular Kalman filter involve recurring state estimations, like capacity, that inform estimates of system measurements, like voltage. In this example, a voltage estimation is produced by a battery capacity model like the empirical models described above. The difference between the voltage estimate and measurement, along with the variability of recent capacity estimations and assumed Gaussian sensor and process noise, generates a correction factor that will be applied to produce a new capacity estimate. As new voltage data is received the process recursively repeats and quickly creates stable estimates of SoH [38], [189]. The basic Kalman filter assumes a linear system, though based on the nonlinear aging characteristics of LIBs, Kalman variants that allow for nonlinear systems are frequently employed.

Particle filters are also very common adaptive methods used for SoH estimation [57], [162], [185], [186]. Similarly to Kalman filters, particle filters estimate battery states that recursively update based on system prediction errors and assumed uncertainty due to noise. Particle filters, however, do not assume Gaussian noise and make predictions using Monte Carlo sampling of a Bayesian probability distribution based on previous estimates and measurements [190]. Deterministic adaptive filtering methods like recursive least squares or observer filtering methods are also found throughout the literature. These also rely on measurement feedback and assumed uncertainty to update state estimations [162], [185], [191], [192]. Adaptive filtering methods can substantially increase the accuracy of SoH estimation, and may also conveniently be used for co-estimation of parameters like SoC [191]–[195]. However, these methods can significantly increase the computational load of calculations, requiring optimization to simplify these feedback structures for online applications.

Data-Driven Models

Highly accurate data-driven modeling methods are widely used throughout the SoH estimation literature [27], [57], [58], [162], [185]. Data-driven methods are generally considered “black-box” systems, where the model logic does not rely on a working knowledge of internal battery dynamics and processes. This offers an advantage in eliminating the need to characterize the physical and electrochemical complexities that drive battery degradation behavior. These methods rely on large sets of high-quality battery degradation data. Data is processed through computationally rigorous algorithms to produce high-fidelity SoH estimation structures. Machine-learning methods, like artificial neural networks and support vector machines, are among the most popular data-driven methods for SoH estimation [58], [185], [196]. While these methods can produce highly accurate SoH estimations, the models themselves lack interpretability and may not provide detail regarding degradation mechanisms. The availability of data that is required for these methods may also serve as an impediment to their use, and the computational burden of processing large data sets with these methods can be much greater relative to other modeling methods [162], [185], [197]. Furthermore, data-driven methods commonly fall under increased risk of overfitting and may poorly generalize to new data [27], [185].

The vast experimental literature on SoH estimation and the nuances of individual studies makes it difficult to quantify the relative accuracies or computational resources required for the modeling methods described in this section. Analysis of dozens of review papers and individual studies show a large diversity of reported accuracies, with SoH estimation errors ranging from tenths of a percent to double-digit percentages for the same methods. With that in mind, in order to supply a modicum of context Table 2 has been included to offer examples of modeling results synthesized from a comprehensive literature review article [45].

Table 2: SoH estimation prediction errors of studies using various modeling methods. Adapted from [45].

Modeling Method	Prediction Error (%)	Reference
Coulomb Counting	<10	[198]
EIS + Neural Network	<2.1	[199]
Neural Network	<0.5	[200], [201]
Support Vector Machine	<2	[202]
Kalman Filter	≤5	[203]
Fuzzy Logic	1.4-9.2%	[204]

4.1.4.3 Pack Level Modeling

The vast majority of studies focusing on LIB SoH modeling are based on cell-level estimations, rather than at the pack-level, as supported by several comprehensive literature review papers [27], [57], [162], [186], [196], [205]. Pack SoH estimation is complicated for many reasons. Firstly, as described in section 4.1.1, defining pack SoH is a challenge in and of itself. Secondly, cells within a battery pack can vary significantly from one another in capacity, SoC, and more. This is referred to as cell-to-cell variation (CtCV) in the literature and will be further discussed in section 4.2. Taking into consideration the challenges of computational complexity on cell-level SoH estimation, applying modeling structures to each cell within a pack massively compounds these issues. Still, it is most common that pack SoH models simply consist of aggregations of cell-level models[18], [61], [62], [66], [206], [207]. Of course, this approach provides useful granularity to pack health, but imposes significant computational concerns when scaling to larger packs.

Single-Cell Models

Few studies model pack SoH using only pack-level measurements and models. These types of models are often called “single-cell models,” as they treat an entire pack as one lumped cell [18]. Modeling strictly at the pack-level can be very useful for gaining a high-level understanding of pack health while

limiting the computation required of a BMS. Bi et al. [25] used a simple cell ECM coupled with a genetic particle filter to estimate pack SoH in terms of resistance rise. The rate at which their model produced stable predictions was reported, but not the actual estimation accuracy. Huotari et al. [208] also modeled the capacity of a battery pack using only pack-level measurements. Their data-driven models used large data sets containing multi-year usage data of 45 forklifts. They were able to achieve a mean absolute error of 0.15% SoH. Zhou et al. [209] modeled the capacity of an EV bus battery pack using Kalman filtering methods. Though the accuracy of their estimations could not be verified they were estimated to have less than 8% error. Dubarry et al. [210] modeled pack capacity using a single cell ECM, but measurements from all individual cells had to be incorporated to achieve reasonable accuracy. Studies like these are relatively scarce in the literature, and more research is needed in the area of pack-level data collection and subsequent model building.

4.2 Cell-to-Cell Variation

4.2.1 Causes and Effects

Cell-to-cell variation (CtCV) refers to inconsistencies between individual battery cells in a pack. Cell SoH, SoC, internal resistance, temperature, and more can deviate considerably within a pack. This creates challenges for a BMS to accurately monitor cells to ensure the safe and efficient utilization of a battery system. The literature commonly identifies CtCV in terms of the range or standard deviation of cell parameters within a battery pack [18], [161], [206], [211], [212]. CtCV exists in battery packs from the moment of pack assembly and increases over time. Two main categories describe the causes of CtCV: intrinsic and extrinsic sources [17], [145], [213]–[215]. Intrinsic sources refer to cell inconsistencies that result from manufacturing processes. Based on the intricacies of LIB fabrication, complete consistency between all produced cells is unachievable. Batteries leaving manufacturing facilities contain disparities in internal cell components, including electrode porosity and composition, material purity, and layering

consistency. When cells are cycled these material inconsistencies present themselves in terms of varied cell capacity, internal resistance, temperature gradients, and more. Several studies show that brand new cells exhibit normal distributions in these parameters when initially characterized [145], [210], [214]–[216]. Once assembled in packs, further CtCV is introduced extrinsically. Extrinsic sources refer to CtCV that is induced due to pack design and environmental cycling conditions. These include factors like inconsistent contact or wiring between cells or temperature gradients induced by inadequate thermal management.

CtCV has been shown to increase significantly over time, irrespective of cycling conditions. In an experimental study performed by Baumhöfer et al [217], 48 new LIB cells were characterized and showed a typical normal distribution in capacities. The cells were all cycled under equal conditions and deviations in their capacities grew significantly over time. The increasing CtCV was attributed to intrinsic sources based on all other conditions being equal. Interestingly, throughout the experiment degradation rates dramatically fluctuated for most cells. Some cells that started with the relative lowest capacities ended up with the highest at the end of testing, while some cells with average capacities were highest mid-testing and ended up being the most degraded in the end. Results underscore the complex nonlinear aging behaviors of LIBs, as well as the need to consistently model SoH based on erratic degradation behaviors. Schuster et al. [145] characterized over 900 LIB cells from retired vehicle battery packs and compared the capacity distribution to a new pack from an identical vehicle. Cell capacity was shown to follow a normal distribution for the new pack, but was significantly skewed in the older packs, as some cells experienced relatively extreme degradation compared to others. The source of increased CtCV over time was not determined. These results were consistent with a similar study performed by Baumann et al. [215].

4.2.1.1 CtCV in Parallel Packs

Current and voltage behaviors in packs can be attributed to increased CtCV over time. In parallel packs, distributions of cell internal resistances cause inhomogeneous currents to flow through cells. Cells with the lowest resistances will experience higher currents compared to low resistance cells. Resistance variability can both cause and result from intrinsic cell properties or imbalances in SoC, temperature, contact resistance, and more. Higher local currents cause further temperature and SoC imbalance and can affect degradation rates and mechanisms, further exacerbating CtCV. However, variations in parallel packs are considered to be less problematic than series arrangements [213], [218]. This is due to a self-balancing phenomenon identified in parallel cells. Inhomogeneous currents form due to resistance variation of aged and new cells. As the SoC and temperature of the high current cell increases, the balance of internal resistances shifts, causing SoC convergence. Pastor-Fernández et al. [218] looked at aging rates of cells placed in parallel and found significant convergence of SoH over time due to the self-balancing phenomenon. Initial capacity fade and power fade distributions of 40% and 45%, respectively, converged to 10% and 30% over 500 cycles, respectively. However, convergence of CtCV in parallel packs should not allay pack inconsistency concerns. Song et al. [158] found capacity variation convergence as well, though noted initial variation caused overall pack degradation to increase compared to packs that started off homogenous. Gogoana et al. [219] tested two-cell parallel packs and found that a pack with a 20% difference in internal resistance between cells reduced the pack cycle life by 40% compared to a homogenous pack. Baumann et al. [215] cast further doubt regarding parallel pack resiliency to CtCV, claiming to disprove the commonly believed self-balancing effect when experimental parallel packs grew in variation over testing. Based on the ability to distribute current amongst cells placed in parallel, the maximum overall capacity of a parallel pack is equal to the sum individual cell capacities [12], [62], which is not the case in series packs.

4.2.1.2 CtCV in Series Packs

Regardless of the extent self-balancing occurs in parallel packs, series packs certainly do not exhibit these behaviors whatsoever. As equal current flows through series packs, variation between cells causes inhomogeneous voltages throughout the pack. This can have serious repercussions on pack utilization efficiency, as the weakest cells in series can determine the power and energy capabilities of the entire pack [206], [220]–[222]. Charge and discharge procedures must be terminated once cells reach their upper or lower safety cutoff limits. In a series arrangement, this means the first cell to reach either limit imposes a complete cessation of current to the pack, leaving all other cells with remaining charge capacity underutilized. Paul et al. [222] modeled the discharge capacity of a pack with 96 cells in series. Results showed that model estimation error declined from 300mAh to 50mAh when considering capacity CtCV instead of treating all cells equal. Furthermore, beyond available capacity and efficiency issues, underutilized cells will experience variations in DoD, SoC, and more, causing varying aging rates [18]. Differing aging rates can further exacerbate pack utilization issues and propagate other forms of CtCV in a cyclic fashion.

Cell Voltage Equalization in Series Packs

CtCV in series packs may be partially alleviated with voltage equalization, which is also referred to as cell balancing. When a BMS detects differences in voltages between cells, balancing controls may be activated to reduce these variations. Voltage equalization techniques are commonly classified as passive or active cell balancing [223]. Active balancing involves transferring charge from higher voltage cells to charge lower voltage cells. The redistribution of charge will cause all cells to reach an equal voltage equivalent to the average voltage before balancing [224]. Thus, with active balancing the maximum capacity of a series pack is the average capacity of all cells [62], [63].

Passive balancing accomplishes pack voltage equalization by discharging higher voltage cells in a pack until they reach the minimum cell's voltage. When a BMS detects voltage inconsistency in a pack, high voltage cells are discharged, often through a resistor network, to dissipate excess energy in the form of heat. For this reason, passive equalization is often referred to as "dissipative" equalization or balancing. Passive balancing reduces the overall maximum capacity of the pack to that of the minimum capacity cell in series [61]–[63]. This reduces the overall efficiency of the system, but is a much cheaper and simpler balancing technique compared to active equalization and therefore more common in EVs [61], [225], [226].

Depending on battery application, topology, or size, no voltage equalization systems may be included with a pack. In this instance, the capacity of a series pack depends on the first cells to hit either upper or lower cutoff voltages during cycling. This can significantly limit pack capacity. The maximum pack capacity for series arrangements is shown in equation 10, where j is the index for a cell in a series of N_p total cells [61]–[63].

$$Q_{pack}(Ah) = \min_{1 \le j \le N_p} \left(SoC_j \cdot Q_j\right) + \min_{1 \le j \le N_p} \left(\left(1 - SoC_j\right) \cdot Q_j\right) \quad (10)$$

Whether or not balancing techniques are used in a pack, these procedures only partially alleviate SoC and DoD CtCV, as they are triggered based on voltage differences and are not responsive to SoC imbalance. Furthermore, these techniques do not address other forms of pack inconsistency, and can even cause temperature gradients in a pack based on dissipative balancing [226]. Therefore, accurate diagnosis and efforts to reduce CtCV are still of major importance for efficient and sustainable pack usage.

4.2.2 SoH CtCV Detection Methods

Outside of individually identifying cell parameters in a pack, there are a few methods used in the literature to detect SoH CtCV. Several studies discovered discrepancies in IC curves of packs with varying CtCV. Krupp et al. [227] identified heterogeneity by tracking the IC curve of a series module containing four cells that were degraded at different C-rates. The module showed a progressive distortion in its IC curve as cells degraded and CtCV increased. This was attributed to variations in both SoC and SoH within the pack, as no cell balancing procedures had been applied during the full pack charge used to produce the IC curves. The authors claimed that they had proven their method to be suitable to identify capacity variation within a pack. However, what the study did not address were variables other than cell capacity that could induce SoC CtCV in practical applications, like temperature or resistance inconsistency. Their analysis is therefore flawed based on the assumption that their methods could directly identify SoH CtCV, when there are a multitude of confounding variables that could create similar results. These other influencing variables would need to be controlled to strictly isolate capacity variation.

Tanim et al. [228] compared both ICA and EIS results of packs with 10 new cells in series versus packs with up to three new cells being replaced by 80% SoH cells. There were growing distinctions from the new packs in ICA and EIS results as more new cells were replaced with degraded ones. Tests were performed at multiple SoC levels, where all cells were held at equal SoC. Results of the EIS measurements created shifts in the Nyquist plots of each pack, which showed consistency with similar studies [229].

Discrepancies between curves were less apparent at different SoC levels, limiting CtCV detection at 50% SoC, for instance. The study showed promising results for CtCV detection through EIS and ICA. Nonetheless, considering the large differences in overall pack SoH amongst tests, it is unclear if discrepancies in EIS and ICA results are due to SoH CtCV specifically or a change in overall pack health.

Controlling pack SoH or performing testing where the highest capacity cells were lower than 100% SoH would be useful to further explore the efficacy of these methods.

Wang et al. [230] were able to identify SoH CtCV by detecting inhomogeneous currents in parallel branches of a pack via magnetic field monitoring. This is useful based on the lack of individual cell current sensors in EV packs [158], [230]. While the authors were able to identify capacity variation and even locate the most degraded cell, this approach wouldn't work in series arrangements where current is equal for all cells. Further, this does not address reasons other than capacity that create inhomogeneous current, like SoC or temperature gradients, and requires specialized equipment. Based on an extensive review of the literature, there is a significant need for studies that isolate the effects of SoH CtCV for diagnostic purposes. In addition, the critiques of ICA and EIS analysis described in section 4.1.4.1 remain valid, and CtCV detection methods that are simpler to perform online would be valuable.

4.2.3 Pack SoH Estimation Literature Critique and Response

Through a thorough analysis of the current LIB SoH modeling literature, there are several key areas of research that require further exploration. There is a significant lack of studies that focus on pack-level SoH estimation. Of the studies that do, the vast majority simply aggregate individual cell models that create significant computational burden for a BMS. The very few studies identified that create SoH models solely using pack-level data either require large historical use data sets or lack clear accuracy validation. Furthermore, these pack-level models do not consider the overall makeup of cells within the pack. SoH CtCV diagnosis is also an area of research that requires further expansion, especially in the case of series-connected packs. Isolating the degree to which capacity variation affects pack behavior and the usage of accessible modeling and data collection techniques can provide further insight into CtCV detection.

In response to these critiques, this dissertation provides novel pack SoH estimation procedures. Models created are primarily based on pack-level measurements and define pack SoH considering the health of all cells comprising a pack. Emphasis is placed on simple repeatable modeling procedures and rapid testing protocols. The models built for this study do not require historical battery pack usage data and use relatively small data sets, quick pulse tests, and computationally inexpensive methods. The following section will provide the necessary context to these modeling procedures.

5 Research Methods Background

5.1 Model Training and Testing

The research outlined in this dissertation is centered around the building of a predictive statistical battery model. Therefore, it may be prudent to provide the conceptual background of basic modeling procedures. To begin, predictive model building is based on the assumption that a dependent variable, which is termed a "response" variable, is a function of one or several independent, or "predictor," variables. A model is "trained" using data from a set of observations that contains all assumed predictor and response variables. Various modeling methods may be employed to quantify the relationships between these two sets of variables. This relationship is then leveraged to produce predictions of the dependent variable for observations in which the independent variables are available and data of the response variable is not.

The ability of a model to produce accurate predictions is often validated using a "testing" data set. This data set consists of new observations that were not used to train the original model, but contain the same predictor and response variables. The independent variables from the testing data set are fed into the trained model to produce predictions of the response variable. These predictions are then compared to the known value of the dependent variables from the testing data set to determine the error of the

model. This process is an example of cross-validation, and is used to estimate how accurate model predictions will be for data where the independent variable is unknown. The error of a prediction is commonly referred to as a "residual," and is the difference between a model prediction and the actual value of the variable predicted. This is shown in equation 11, where ϵ is the residual, y is the actual value of an observation, and $\hat{y}$ is the prediction of the same observation.

$$\epsilon = y - \hat{y} \tag{11}$$

Cross-validation may be used to compare the accuracy of different models or to determine the presence of data "overfitting" [231]. Data overfitting occurs when a model accurately describes a training data set, but does not generalize well to predict new data outside of the training data set. A common cross-validation technique is known as "leave-one-out" cross-validation (LOOCV), which is used in the study outlined in this dissertation. This technique involves training a model using data from all but one of the available observations. The left-out observation is used as the testing data set and the prediction error is collected. This process is repeated, leaving out a new observation for testing while returning the previous iteration's unincluded observation back into the training data set. This iterative process repeats until all observations have been used as the testing data set and the average error of all iterations is identified. The average errors of different models may then be compared for appropriate model selection. Also, LOOCV results may also indicate overfitting issues if the errors from each iteration fluctuate significantly. Error fluctuation would indicate a high sensitivity to which data is used for training and unreliable model performance. Highly generalizable models should operate consistently to provide confidence in the expected error of the model when applied to new data.

LOOCV is just one of many cross-validation techniques used to interpret the accuracy and generalizability of a model. For instance, the "k-fold" cross-validation method operates similarly to LOOCV, where a different portion of data is systematically "left out" for validation from the rest of the training data. For example, for a 5-fold cross-validation approximately one fifth of the data is left out for

validation, and the process is repeated five times until all observations have been left out once. When the number of folds is equivalent to the number of observations in the data set, the k-fold method simply becomes LOOCV. LOOCV is more suitable for smaller data sets, since there is little data available for model training. Lower-order folds are appropriate for larger data sets to reduce the computation time of the cross-validation procedures [232].

The overall accuracy of a model may be identified by using several common metrics that quantify the average error of predictions. These include mean absolute error (MAE), maximum absolute error (MaxAE), mean squared error (MSE), root-mean squared error (RMSE), and mean absolute percent error (MAPE). These metrics are calculated using equations 12-16, where ϵ, y, and $\hat{y}$ share the same definitions as equation 11 and n is the number of observations predicted.

$$MAE = \frac{1}{n}\sum_{i=1}^{n}|\epsilon_i| \tag{12}$$

$$MaxAE = \max\sum_{i=1}^{n}|\epsilon_i| \tag{13}$$

$$MSE = \frac{1}{n}\sum_{i=1}^{n}\epsilon_i^2 \tag{14}$$

$$RMSE = \sqrt{MSE} \tag{15}$$

$$MAPE = \frac{1}{n}\sum_{i=1}^{n}\left|\frac{y_i - \hat{y}_i}{y_i}\right| \tag{16}$$

5.2 Statistical Relationship Metrics

The ability to process and glean meaning from the experimental data used in this dissertation heavily relies on the understanding of several key statistical properties. Correlation and partial correlations are identified in this research and are used to quantify the statistical relationships between variables. Correlation measures the extent to which two variables are linearly related and is commonly quantified using Pearson's correlation coefficient (ρ). Equation 17 shows how the unitless Pearson correlation coefficient is calculated. In this equation x and y are random variables with averages of $\bar{x}$ and $\bar{y}$, and n is sample size. Equation 17 also shows that ρ is equivalent to the covariance of x and y divided by the product of their standard deviations.

$$\rho_{xy} = \frac{cov(x,y)}{\sigma_x \sigma_y} = \frac{\sum_{i=1}^{n}(x_i - \bar{x})(y_i - \bar{y})}{\sqrt{\sum_{i=1}^{n}(x_i - \bar{x})^2 (y_i - \bar{y})^2}} \quad (17)$$

A maximum ρ value of 1 indicates a perfect positive linear relationship between two variables, meaning a positive change in x is exactly proportional to a positive change in y [233]. Conversely, a minimum ρ value of -1 indicates a perfectly negative linear relationship, where an increase in x corresponds to a decrease in y. The closer ρ is to the -1 and 1 extrema, the stronger the linear relationship between two variables. Considerations for what is judged to be a strong, moderate, or weak correlation is somewhat subjective and application-based.

In instances where there is a random variable or set of random variables that influences both x and y, a Pearson's correlation coefficient may give misleading results. It may be the case that x and y are not directly related, even when they are shown to have a strong correlation. This is called a spurious relationship. Spurious relationships may occur when an outside variable's influence on both x and y cause an inadvertent statistical relationship between x and y. In order to control for the impact of the

influencing (i.e., “confounding”) variable on the relationship between x and y, a partial correlation may be performed. A Pearson’s partial correlation coefficient can be interpreted the same way as a standard Pearson’s correlation coefficient, with values ranging from -1 to 1. The equation for a Pearson’s partial correlation coefficient that isolates the relationship between x and y while controlling for the influence of a confounding variable z is shown in equation 18.

$$\rho_{xy \cdot z} = \frac{\rho_{xy} - \rho_{xz} \cdot \rho_{yz}}{\sqrt{(1 - \rho_{xz}^2)(1 - \rho_{yz}^2)}} \tag{18}$$

It is important to note that statistical relationships such as the ones discussed above are often based on a sample of observations from a population. These statistics are therefore estimations of the true statistics that describe the entire population. In the case of this research, parameters from experimental battery cells and packs are analyzed to provide evidence of the relationships between the parameters of all LIBs that share the same specifications (e.g., chemistry, capacity, etc.). Thus, the experimental cells and packs should be considered a sample of the larger population of similar LIBs. In instances when statistics from a sample are meant to describe a population it is necessary to perform significance testing.

Significance testing is a practice that determines the likelihood sample statistics are representative of the population. This is performed through hypothesis testing, where a probability is calculated that a given hypothesis is correct. In the case of correlations and partial correlations, the tested (i.e., “null”) hypothesis states that the true correlations of variables in the population are equal to 0, meaning there is no linear relationship whatsoever between x and y. A statistic is considered significant if the probability of the null hypothesis being true is found to be less than a specified threshold. Frequently, this threshold is set at 5% probability, which corresponds to a 95% confidence interval that the

calculated sample statistic is representative of the population statistic. This probability threshold is often reported by the letter α, where a 95% confidence interval corresponds to α equaling 0.05. The probability that the null hypothesis is true is determined by using a traditional t-test, where a t-statistic is calculated and corresponds to a probability identified by the t-distribution of appropriate degrees of freedom. The t-statistics for the Pearson's correlation and partial correlation coefficients are calculated using equations 19 and 20, respectively. The letters n and k correspond to the sample size and number of confounding variables, respectively.

$$t_{xy} = \frac{\rho_{xy}\sqrt{n-2}}{\sqrt{1-\rho_{xy}^2}} \tag{19}$$

$$t_{xy \cdot z} = \rho_{xy \cdot z}\sqrt{\frac{n-2-k}{1-\rho_{xy \cdot z}^2}} \tag{20}$$

5.3 Relevant Regression Modeling

Partial least squares (PLS) regression is a useful tool to model the linear relationships between independent and dependent variables. PLS regression is a dimension-reduction technique that takes large sets of variables and reduces them to a smaller number of "latent variables" that are then fed into a typical multiple linear regression equation. In order to understand PLS regression, it is therefore necessary to understand the basic principles of multiple linear regression.

5.3.1 Multiple Linear Regression

Multiple linear regression (MLR) is a fundamental statistical modeling procedure that uses basic linear algebra to find the linear relationships between variables. It operates as an extension and under the principles of ordinary least squares (OLS) regression, where independent variables are assigned coefficients to predict a dependent variable with minimized error. Equation 21 shows the linear regression model for an individual observation. Equations 22 and 23 show the linear model in matrix form when it is used to produce predictions for multiple observations simultaneously.

$$y = \beta_0 + \beta_1 x_1 + \beta_2 x_2 + \cdots + \beta_n x_n + \epsilon \tag{21}$$

$$\begin{bmatrix} y_1 \\ y_2 \\ \vdots \\ y_d \end{bmatrix} = \begin{bmatrix} 1 & x_{1,1} & x_{1,2} & \cdots & x_{1,n} \\ 1 & x_{2,1} & x_{2,2} & \ddots & x_{2,n} \\ \vdots & \vdots & \vdots & \ddots & \vdots \\ 1 & x_{d,1} & x_{d,2} & \cdots & x_{d,n} \end{bmatrix} \begin{bmatrix} \beta_0 \\ \beta_1 \\ \vdots \\ \beta_n \end{bmatrix} + \begin{bmatrix} \epsilon_1 \\ \epsilon_2 \\ \vdots \\ \epsilon_d \end{bmatrix} \tag{22}$$

$$Y = X\beta + \epsilon \tag{23}$$

The variable y is the dependent variable, β are the coefficients, x are the independent variables, n is the number of independent variables evaluated, d is the number of observations, and ϵ is the residuals of the model. The expanded matrix in equation 22 may be visually condensed for legibility to produce equation 23, where Y, X, β, and ϵ refer to the underlying expanded matrices.

The MLR process involves collecting d number of observations that include all independent and dependent variables under analysis. The data is then organized into the matrix form seen in equation 22. The basis of the regression is to solve for β coefficients that, when multiplied by the variables in the X

matrix, produce a prediction of Y that minimizes ϵ. The β matrix is solved for using the least squares method [234], as shown in equation 24.

$$\hat{\beta} = (X'X)^{-1}X'Y \tag{24}$$

The " ^ " symbol above the β indicates that it is a predicted value, while the " ' " symbol refers to a transposed matrix. Once MLR is performed, the estimated coefficient values may be applied to new sets of observed data, where the unknown y value is predicted.

For many applications, MLR can produce accurate predictions and is a computationally efficient method to model the relationships between variables. However, the ability of MLR to produce accurate predictions requires several assumptions and conditions to be met regarding the data in X and Y. One of these key conditions is that the predictor variables used in MLR should be uncorrelated with one another. When collinearity exists between independent variables there are different types of modeling procedures that may be used to produce accurate predictions of response variables. PLS regression is a technique that is well suited in instances of multicollinearity, as well as when there are a large number of independent variables relative to the number of observations available to produce the model [235], [236]. The basic function of PLS is to transform raw data sets that have a large number of collinear predictor variables into a smaller set of uncorrelated variables.

5.3.2 Principal Component Analysis

PLS may be best understood by first describing a technique that is closely related to PLS: principal component analysis (PCA). PLS and PCA share the same basic principles, where data structures are transformed to decompose multiple variables into components or latent variables that reduce the dimensions of the data set while maintaining the critical information contained in the original data. Both methods utilize the functionality of scores and loadings vectors.

The usage of the scores vector in PCA is to project the original data along the dominant eigenvectors of the covariance matrix of X. Each projection creates a principal component. Each eigenvector of the covariance matrix is orthogonal, removing any issues of collinearity from the original data. The loadings vector applies weights to the scores that correspond to the correlations between the original data variables and the principal component. These are calculated by taking an eigenvector of the covariance matrix and multiplying it by the square root of the corresponding eigenvalue. The purpose of this process is to decompose X into smaller components that maintain the maximum amount of variance found in the original data. The variance of the original data should be considered as the minimum amount of useful information that can be used to describe the data for the purposes of regression or categorization.

In order to further understand PCA, a basic visual representation of the process is helpful. Consider a two-dimensional data set, as illustrated in Figure 6. The PCA approach to this data set would be to consider if the data could be usefully described in one dimension or categorized in some way to summarize meaningful properties about the data.

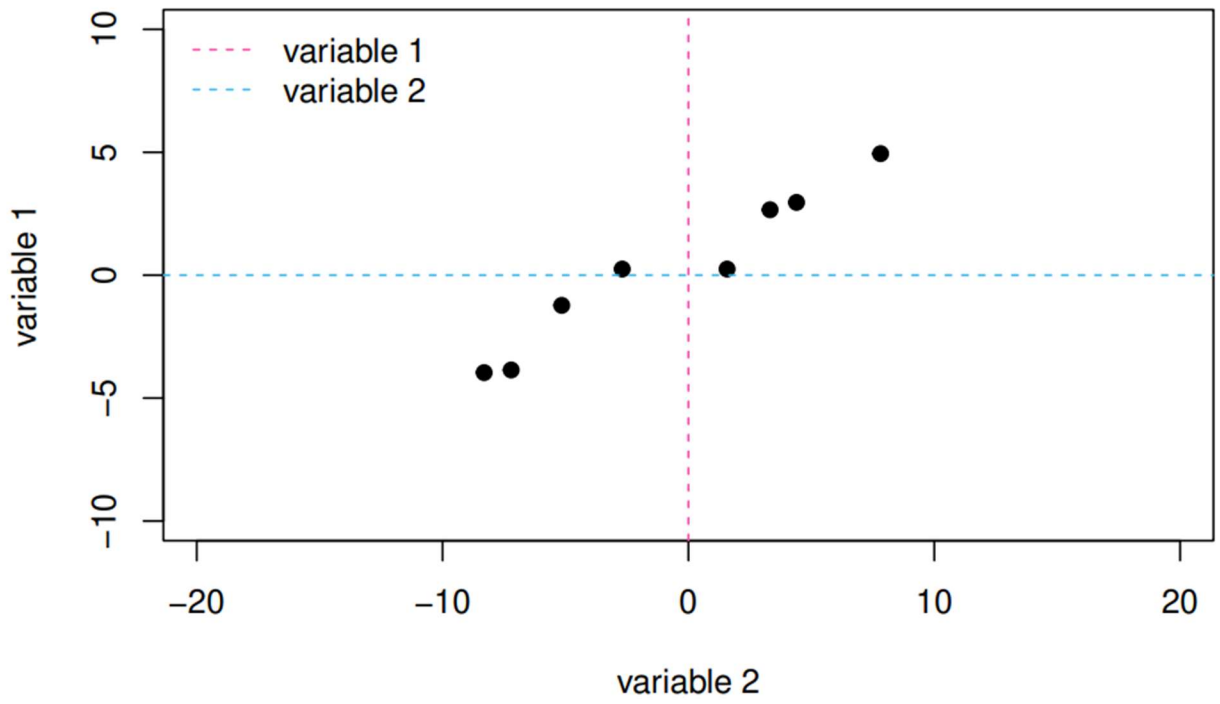

Figure 6: Example two-dimensional data set for principal component analysis discussion. Reproduced from [237].

Inspection of the data shows that there is a large variance of data along an imaginary positive-sloping diagonal axis. This axis is the dominant eigenvector (the vector associated with the largest eigenvalue) of the covariance matrix between variable 1 and variable 2. Multiplying the data by this eigenvector (i.e., the scores vector) has the effect of rotating the axes that the data lies on, changing the perspective of the viewer to show the dimensions where the data contains the most variance. Considering the two-dimensional data, there are a maximum of two eigenvectors of the covariance matrix and therefore two principal components that may be extracted. The second eigenvector will be orthogonal to the first and will orient the data along the axis and dimension where the second-most and remaining amount of variance in the data lies. The scores vector for each component offers the coordinates of the data in relation to the new axis.

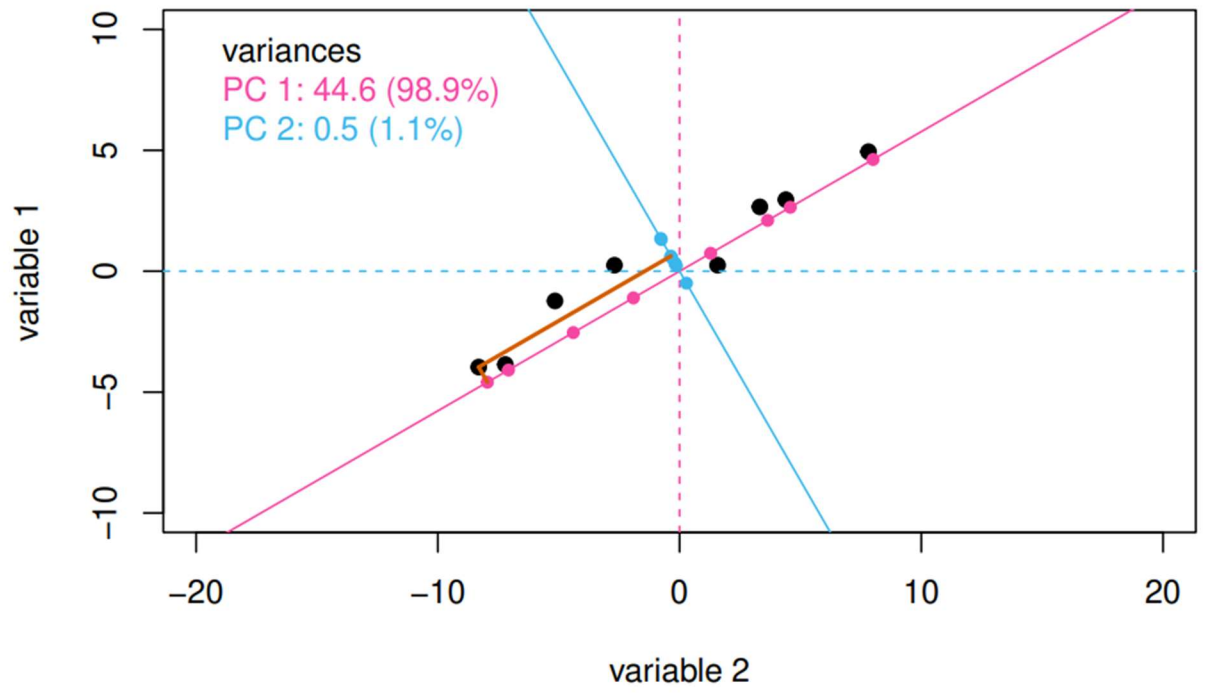

Figure 7: The data shown in Figure 6 is projected along the dominant eigenvectors of the variables' covariance matrix. Reproduced from [237].

For instance, the furthest data point in the top right of Figure 7 is located far along the first eigenvector from the intersection of the rotated axes. In terms of the first eigenvector and principal component (shown in pink), it would have the most positive score of any data point. The same data point is not located far along the second principal component axis and would have a very small score associated with that data point in the second principal component. PCA may be used for data categorization when there are clear groupings of data points shown in the rotated coordinate system.

The loadings matrix serves to identify and translate the importance of certain variables in their contribution to the overall variance captured in a principal component. The contribution of variance is quantified as the correlation between a variable and the principal component. Multiplying the scores and loadings associated with an eigenvector creates a singular component which may serve as an independent variable in a regression model. In summary, the scores rotate the data towards the

direction of maximum variance and the loadings apply weights to the most influential variables that describe the variance of the data along the eigenvector.

In the example described above, a principal component basically packages (or decomposes) the two independent (potentially collinear) variables into a singular variable that is a useful translation of the original data. A maximum of two components (two separate ways to combine the two original independent variables) may be created based on the number of eigenvalues for the covariance matrix. Figure 7 shows that 98.9% of the variance of the original data is contained within the first principal component (i.e., "PC1"). In this instance, a regression to predict Y may be performed on the first principal component alone, considering the marginal contribution of the second component in describing the original data. In this way, the PCA has reduced both the dimensions of the data and the resultant computation required of the regression model.

Just as in MLR, principal component regression models are built by estimating β coefficients that can be applied to new data to produce predictions of Y. Through PCA, the original X matrix has been translated into scores and loadings matrices for each principal component, taking the form shown in equation 25. T is the scores matrix and P is the loadings matrix.

$$X = TP' \tag{25}$$

After solving for T through equation 26 , the result can be used in the regression model, shown in equation 27. $\hat{\beta}$ can then be calculated using equation 28.

$$T = XP \tag{26}$$

$$Y = T\beta + \epsilon \tag{27}$$

$$\hat{\beta} = (T'T)^{-1}T'Y \tag{28}$$

Considering the inputs of the principal component regression model, new data of the same form as X, X_{new}, will need to be transformed into principal component form to produce estimations of Y. In order to transform X_{new} into the proper form, free from collinearity and at reduced dimensions, new scores will be calculated. Plugging X_{new} into equation 26 will produce an estimate of T. The estimate of T can then be multiplied by the $\hat{\beta}$ coefficient (that was estimated from the original data) to produce new predictions of Y.

5.3.3 Partial Least Squares Regression

PLS works in a very similar way, yet is generally more advantageous than PCA in creating accurate predictive models. This is because PCA is considered an unsupervised learning method, while PLS is considered a supervised learning method. PCA operates on information solely based on independent variables (the X matrix), while the PLS process considers data from both independent and dependent (the Y matrix) variables. Since the PLS model is trained with data that includes the response variable(s), it will most likely be better at accurately predicting the response variable(s).

Instead of orienting the data towards directions of maximum variance in X, like in PCA, PLS orients both the data in Y and X in the directions of maximum covariance between the two sets of variables. It then decomposes the X matrix into "latent variables," which are analogous to principal components. It is for this reason that PLS is often referred to not only as "partial least squares," but also "projection on latent structures" [236].

There are several algorithms used to perform PLS regression. The choice of which algorithm to use will depend on the structure of the data set being used, as well as the desired level of computational complexity. All algorithms share the same basic approach, with some finding statistical shortcuts to speed up the computation depending on the nature of the data set. This discussion will focus on the classical PLS regression algorithm known as the non-linear iterative partial least squares (NIPALS) method.

The NIPALS algorithm consists of a series of iterative regressions that ultimately orients and weights the raw data in such a way that maximizes the predictive accuracy of the final regression model. To start, the raw data matrices Y and X are mean-centered and normalized. This means that for each column, the average of the column is subtracted from each observation. The data may then also be scaled by dividing every observation by the variance of that column. Once the data has been prepared, the PLS process may begin.

Akin to PCA, the final transformation of the X and Y matrices in PLS are described in terms of scores (T, U) and loadings (P, Q), shown in equations 29 and 30. E and F are the matrices of residuals, similar to ϵ in MLR.

$$X = TP' + E \tag{29}$$

$$Y = UQ' + F \tag{30}$$

The NIPALS process accomplishes the realignment of the X and Y matrices towards maximum covariance by first exchanging the score vectors of both matrices. The algorithm then iteratively solves for the other equation variables via regression until stable values are reached. For reasons explained later, the loading

matrix P will be replaced by the weightings matrix W to begin. The NIPALS process proceeds as follows [238]–[240]:

1. To begin the iterative process, initialize matrix U as a random vector the same length as Y.

2. Replace T with U in the updated equation 29, where W is in place of P. Solve for W via least squares regression.

$$W = (U'U)^{-1}U'X \tag{31}$$

Larger values in W will correspond to variables in X that are highly correlated with values in U, while low correlation variables will have values close to zero.

3. Normalize W to unit length.

$$W'_{new} = \frac{W'_{old}}{\|W'_{old}\|} \tag{32}$$

4. Solve for T in the updated (W is still in place of P) equation 29.

$$T = (W'W)^{-1}XW \tag{33}$$

The relative magnitude of values in T will follow a similar pattern to W. Larger values in T correspond to stronger correlations between X and W variables. Based on these initial steps, the original Y scores (i.e., U) that were highly correlated to X influenced the creation of W, and subsequently the creation of X scores (i.e., T). The process will resume to create a similar alignment, where the updated X scores that correlate strongly with Y will influence the creation of updated Y scores and loadings.

5. Substitute the calculated T for U in equation 30. Solve for Q, then normalize Q.

$$Q' = (T'T)^{-1}T'Y \tag{34}$$

6. Solve for U in the original equation 30.

$$U = (Q'Q)^{-1}YQ \tag{35}$$

7. Check for convergence of T. After several iterations T will cease to change, meaning U, Q, and W have also converged to stable values. At this point in the process, the respective influences between X and Y that have updated both of their scores and loadings has created maximal alignment between X and Y. The scores and loadings for each project the original data towards the direction of maximum covariance. If T has not converged, repeat steps 2-7.

8. Calculate P, the loadings matrix of X, using the original equation 29.

$$P' = (T'T)^{-1}T'X \tag{36}$$

The key difference between P and W is that W represents and is built based on features in X that are related to the original data in Y. On the other hand, P is created based on the inner relationship between T and X. It is created solely based on X, and not on Y. The weightings (W) impart influence from Y onto the X scores at the beginning of the process, but they themselves are not the loadings of X.

9. Rescale T, W, and P. Store for future use.

$$T_{new} = T_{old}\|P'\| \tag{37}$$

$$W'_{new} = W'_{old}\|P'\| \tag{38}$$

$$P'_{new} = \frac{P'_{old}}{\left\|P'_{old}\right\|} \tag{39}$$

10. Calculate the scalar coefficient B, store for later use.

$$B = (T'T)^{-1}U'T \tag{40}$$

All X and Y scores and loadings for the first latent variable have been created at this point. Considering the eventual goal of this process is to create predictions of Y given X_{new}, Y will be unavailable to project towards the direction of maximum covariance with X_{new}. It is therefore necessary to convert the calculated Y scores, that align Y towards the respective X alignment, to be in terms of X alone. The coefficient B serves as conversion factor of Y scores in terms of X ($U = BT$). At this point, all steps to create the first latent variable have been completed.

To create a new latent variable, one must "deflate" the X and Y matrices. Analogous to a principal component, each latent variable created only represents a portion of the variance in X and Y. All remaining variance data from the original X and Y matrices not captured in the first latent variable are held in the residual matrices E and F from equations 29 and 30. The deflation process calculates the residual matrices, which will then replace the respective X and Y matrices in the next iteration of steps 1-10 to create the next latent variable. The subsequent latent variable after that will be similarly found. The residuals from the previous latent variable calculation will serve as the independent and dependent variable matrices in the following iteration. The deflation process for calculating the latent variable residuals is shown in equations 41 and 42, where k is the number of latent variables calculated.

$$E_k = E_{k-1} - T_k P_k' \ ; \ X = E_0 \tag{41}$$

$$F_k = F_{k-1} - B_k T_k Q'_k \ ; \ Y = F_0 \tag{42}$$

Once all desired latent variables are calculated, the predictive regression model can be created. The final matrices used for regression contain each latent variable's weightings, scores, loadings, and B coefficient matrices that are stored for each iteration of latent variable creation. The process is similar to principal component regression, where a coefficient will be calculated that, when multiplied by the X scores, produces a prediction of Y. The issue in PLS regression, however, is that the scores and loadings of latent variables are in terms of the residual matrices of the preceding latent variable. An adjusted loadings matrix R may be created to put the X loadings in terms of the original X matrix. This calculation is shown in equation 43.

$$R = W(P'W)^{-1} \tag{43}$$

Similarly to equation 26, adjusted scores can now be calculated using the adjusted loadings, R, using equation 44.

$$T = XR \tag{44}$$

This allows a final regression model to be used easily without concern for the deflation of matrices over the course of the PLS process. The final PLS regression model is shown in equation 45.

$$Y = T \cdot diag(B) \cdot Q' = X \cdot R \cdot diag(B) \cdot Q' = X \cdot \beta_{PLS} \tag{45}$$

In review, the X scores (T) multiplied by the coefficients in B are effectively equivalent to the Y scores. These are then multiplied by the Y loadings (Q) to define Y. Further expansion shown in equation 45 alludes to the straightforward solution for β_{PLS}, shown in equation 46. Future predictions of Y when given X_{new} can be accomplished by simply multiplying X_{new} by the calculated $\hat{\beta}_{PLS}$.

$$\hat{\beta}_{PLS} = R \cdot diag(B) \cdot Q' \tag{46}$$

The number of latent variables to include in the final model is often decided based on cross-validation results. For example, a large number of latent variables can be initially created. LOOCV may be performed to find the average error of predictions when only one latent variable is included in the model. This would then be repeated, incrementally adding latent variables to the model. Eventually, adding more latent variables will either create insignificant increases to prediction accuracy or a decrease in accuracy due to overfitting. The optimal number of latent variables to include may then be decided. This will be exemplified in the results sections 11 and 13.

5.4 Battery Equivalent Circuit Models

In order to estimate various battery parameters and ensure efficient and safe operation of battery systems, researchers have investigated numerous methods to model battery voltage behavior. One of the most common and useful methods to accurately conceptualize and model battery voltage behavior uses the concept of equivalent circuits. When current is applied to a LIB, the internal charge transfer processes present themselves in a nonlinear dynamic voltage response, as shown in Figure 8. The physical and electrochemical reactions that govern these behaviors may be accurately analogized to various electrical circuit elements. Depending on the accuracy required of a model, ECMs may vary in complexity. The following discussion will use a bottom-up approach, starting at the most basic form of

ECM and will incrementally introduce more circuit elements and complexity used in common ECMs. The contents of this discussion have been largely informed and closely follow the structure found in [12].

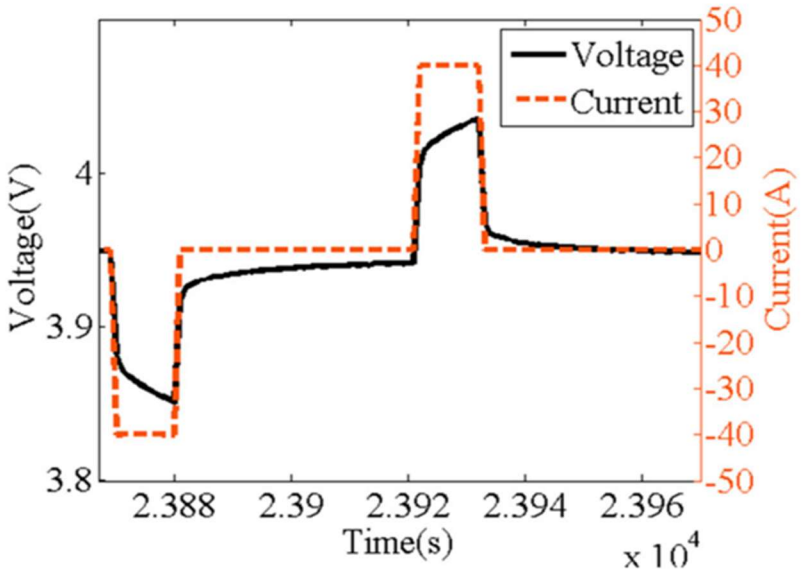

Figure 8: Typical LIB voltage response to current input. Reproduced from [241].

5.4.1 OCV Model

The most basic ECM treats a LIB as an ideal voltage source. In this circuit, as current is applied to a battery the voltage response is exclusively based on a change in OCV as a function of SoC change. Equation 47 shows how SoC changes with time based on the current applied and coulombic efficiency of the battery. In the following equations z is defined as SoC, η is coulombic efficiency, Q is the battery capacity, i is the current, and t is time. The equation shows that from a starting SoC at t_0, SoC changes based on the magnitude, sign (charging is negative, discharging is positive), and how long a current is applied to the cell multiplied by its charge efficiency. The amount of Ah charged or discharged from the cell, minus efficiency losses, divided by the total Ah capacity of the cell is the SoC change. For reference, the coulombic efficiency of LIBs is around 99% or higher [12]. Equation 48 shows the continuous voltage response equation for the overall OCV model, introducing the new variable, v, for voltage. Figures 9 and 10 depict the equivalent circuit and OCV-SoC curves for common battery chemistries, respectively.

$$z(t) = z(t_0) - \frac{1}{Q}\int_{t_0}^{t} \eta(T)\, i(T)\, dT \tag{47}$$

$$v(t) = OCV(z(t)) \tag{48}$$

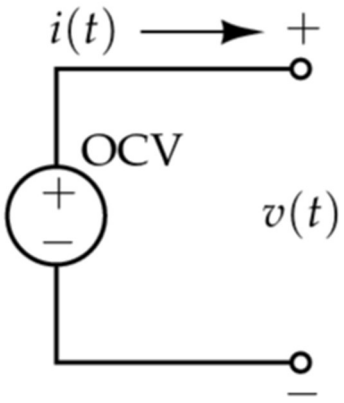

Figure 9: Basic equivalent circuit model where battery terminal voltage is solely a function of OCV. Reproduced from [12].

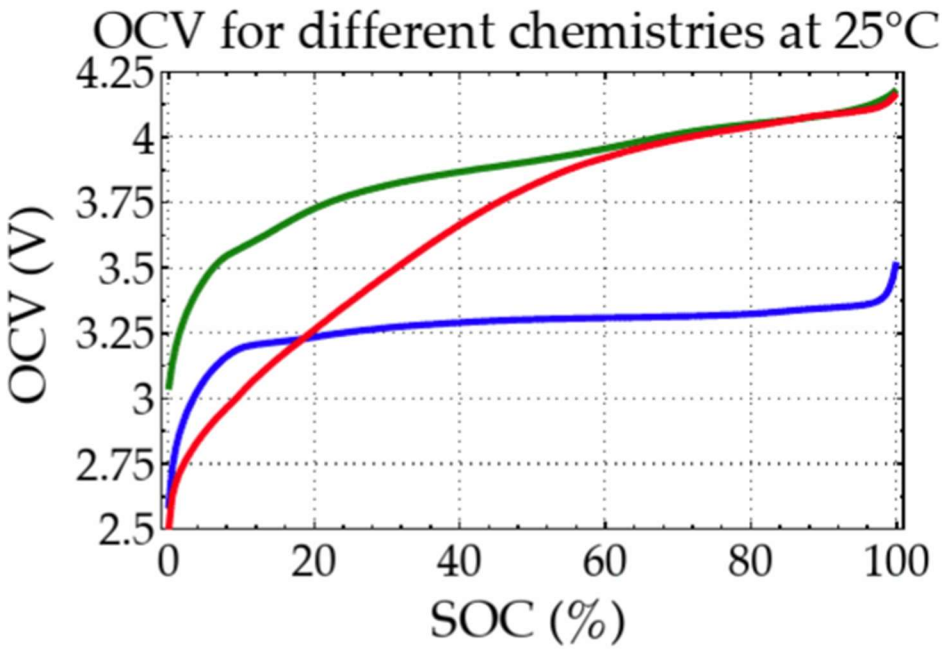

Figure 10: SOC-OCV curves for common lithium-ion cell chemistries tested. Reproduced from [12].

5.4.2 Rint Model

Considering the OCV of a battery is reached only after long periods of rest, the previous model is quite limited in its usefulness. The concept of cell polarization, which is the departure of a cell's terminal voltage from OCV, shall be introduced. To describe the immediate voltage response of LIBs to current, a series resistor element is added to ECMs, as shown in Figure 11. This model is commonly referred to as the "Rint" model. The series resistance creates an instantaneous response in voltage based on the magnitude and sign of the current, as dictated by Ohm's law. The voltage change over the series resistor is added to the OCV model, as shown in equation 49. R_0 is the series resistance value, which models the total ohmic internal resistance of the battery. R_0 models the sum of resistances from cell components like the electrolyte, current collectors, separators, and more [242]. Using Ohm's law and measuring the instantaneous change in voltage based on the change in current, one can easily calculate the value for R_0. The Rint model not only describes a LIB's immediate voltage change in response to current, it also introduces ohmic heating and power dissipation implications.

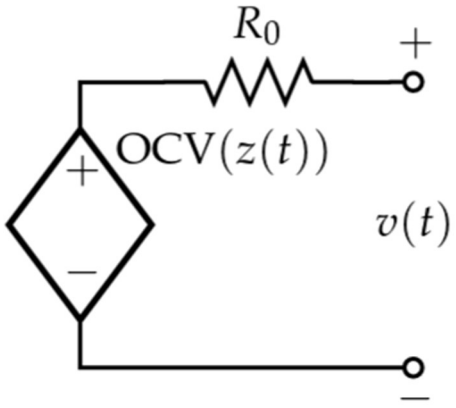

Figure 11: "Rint" equivalent circuit model where battery voltage is a function of OCV and series resistance. Reproduced from [12].

$$v(t) = OCV\big(z(t)\big) - R_0 i(t) \tag{49}$$

5.4.3 Thévenin Model

The characteristic complex nonlinear voltage behavior of LIBs is still not described by the Rint model, hence more circuit elements are required to describe this phenomenon. This nonlinear behavior is demonstrated in the voltage response curvature in Figure 8 during both periods of applied current and rest. Focusing on the extended period where no current is applied in the figure, the immediate voltage change associated with a series resistor is followed by an extended voltage relaxation period, where cell voltage slowly decays towards OCV. This slow voltage evolution is attributed to the diffusion of lithium ions in the electrolyte and bulk electrode materials and charge transfer reaction kinetics [243]–[247]. The nonlinear portion of the voltage response of a LIB is therefore often termed a "diffusion voltage," and may be also labeled as the dynamic effects of the battery. The dynamic voltage effects begin to be described with the introduction of a parallel resistor-capacitor (RC) subcircuit. The addition of an RC pair to the Rint model creates what is called the Thévenin model, which is illustrated in Figure 12.

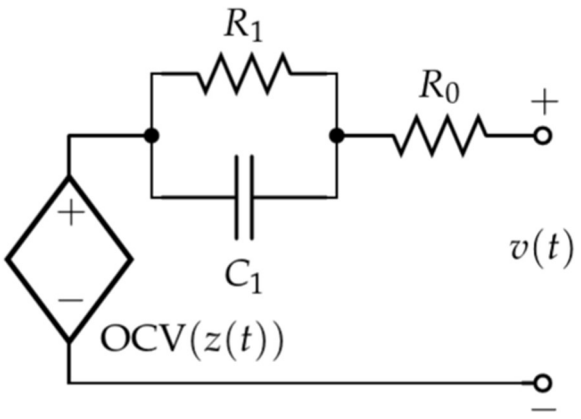

Figure 12: Thévenin equivalent circuit model where battery voltage is solely a function of OCV, series resistance, and polarization resistances. Reproduced from [12].

Equation 50 shows the voltage evolution over time explained by the Thévenin model. The voltage change across the capacitor, C_1, is a function of the parallel resistor in the subcircuit, R_1, and is shown in equation 51.

$$v(t) = OCV\big(z(t)\big) - v_{C_1}(t) - i(t)R_0 \tag{50}$$

$$v_{C_1}(t) = v_{C_1}(t_0)e^{-\frac{t}{R_1C_1}} - \ i(t)R_1(1 - e^{-\frac{t}{R_1C_1}}) \tag{51}$$

In the capacitor equation there is the inclusion of the subcircuit time constant, which is the product of R_1 and C_1 and is commonly replaced with the variable τ. The time constant of the battery indicates the rate that the diffusion voltage evolves. Specifically, it is the amount of time it takes for the diffusion voltage to decay to 36.8% of its initial value. Figure 13 depicts a curve that exemplifies the dynamic effects of a LIB once a charge pulse has ceased, showing the voltage relaxation period that occurs following an immediate ohmic voltage drop. The time constant of the battery is specified, showing a 63.2% voltage loss from the initial Uo voltage. τ may be calculated directly by timing the voltage decay or may be estimated using the battery voltage model.

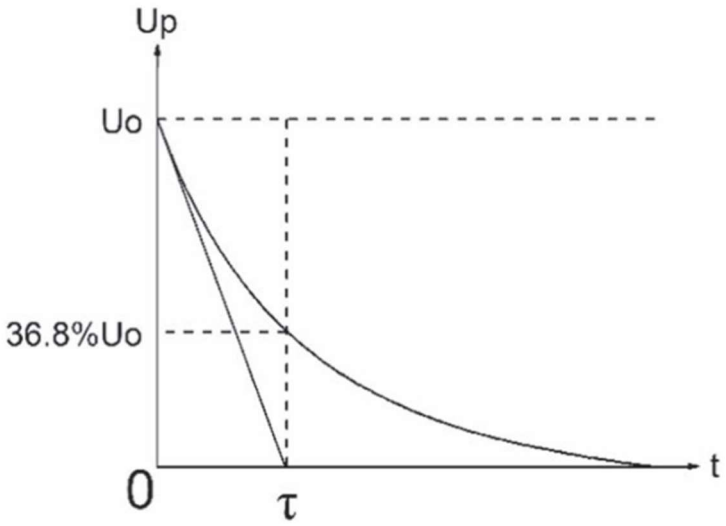

Figure 13: The diagram shows the appearance of a typic voltage relaxation curve and its time constant. Reproduced from [248].

The Thévenin model is often modified by adding more RC pairs to the equivalent circuit. This increases the accuracy of the model in describing diffusion voltages, but also increases the computational complexity of the model. Studies have shown that there are diminishing returns in model accuracy as more RC subcircuits are included in an ECM [246], [249]. With additional RC circuits, more time constant values may be calculated to ascribe more specific battery diffusion processes to voltage response curves. For instance, in a model with two RC pairs the first time constant is often tied to the "fast dynamics" or "activation polarization" of charge transfer processes, while the second time constant describes the "slow dynamics" or "concentration polarization" of diffusion processes [157], [246], [247]. Multiple-order time constants can be measured by timing a 63.2% voltage decay from the voltage value at the end of the previous time constant, or estimated based on voltage models. The increasing accuracy of including multiple RC pairs in an ECM is illustrated in Figure 14.

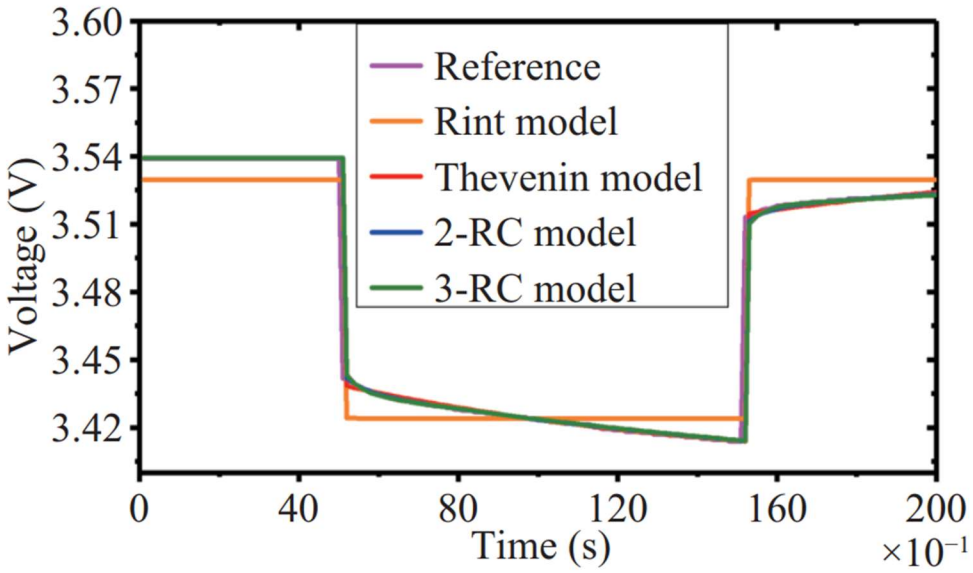

Figure 14: The voltage response estimations produced by various ECMs. Reproduced from [250].

There are numerous other ECMs commonly used in the literature to describe battery voltage behaviors. Some use different circuit elements, like inductors and constant phase elements, while others use stand-in components that characterize battery hysteresis or Warburg impedance [187], [251]–[253]. Ultimately, the selection of which ECM is appropriate to use will depend on the application, data availability, and computational capacity.

Part III. Research Methodology

The following sections in Part III describe the methods used to create PLS regression models for pack SoH and SoH CtCV prediction. All battery cell and pack testing procedures were performed using an Arbin Instruments BT-2043 Battery Test System at room temperature. For the purposes of this study, the SoH of a battery cell and battery pack consisting of four cells in series is defined by the following equations, respectively:

$$Cell\ SoH\ (\%) = \frac{Q}{Q_r} \times 100\% \tag{52}$$

$$Pack\ SoH\ (\%) = \frac{\sum_{i=1}^{4} Q_i}{\sum_{i=1}^{4} Q_{r,i}} \times 100\% = \frac{\sum_{i=1}^{4} (Cell\ SoH_i)}{4} \tag{53}$$

Where Q is defined as the at-present capacity and Q_r is the nominal or rated capacity of a cell in Ah. Pack SoH is defined in terms of the cumulative cell capacities divided by their cumulative nominal capacities, which is equivalent to the average cell SoH. This definition is useful for series packs with active balancing, as well as to describe overall pack health with respect to every cell.

6 Experimental Cell Characterization and Setup

Prior to pack-level experimentation, it was necessary to degrade and characterize the experimental battery cells that would be used to form various experimental packs. New NCA cells were purchased for this experiment. The LFP cells used for this study were borrowed from another experiment, many of

which had already been partially degraded. The nominal capacities of the NCA and LFP cells was 2.5 Ah and 1.5 Ah, respectively. Cell capacities were characterized by constant current constant voltage (CCCV) charging the batteries to 100% SoC at 0.5 C with a 0.01 C cutoff current followed by a 5-minute rest. The capacities were then directly measured via Ah counting during a 0.5 C discharge until they reached their lower cutoff voltages.

Following initial capacity measurements, several cells for each chemistry type were cycled to degrade their capacities to four SoH setpoints. For the NCA cells, four cells were cycled to approximately 80%, 85%, and 90%, and five were cycled to approximately 95% SoH for each chemistry, totaling 17 experimental cells. The LFP cells were degraded similarly, though an extra 80% SoH cell was used based on an inadvertent over-degradation of a cell. There were 18 total experimental LFP cells. The setpoints and number of cells were chosen to allow a variety of battery packs to be formed with different pack SoH and CtCV, as described in the following section. 80% was chosen as the minimum cell SoH used due to the fact that EV battery packs are often retired once they degrade to 80% SoH [24]–[28] and an EV's pack SoH is often defined by its lowest capacity cells [61], [62]. The degradation cycling procedures involved repeated 2 C CCCV charges and 2 C discharges with resting periods between steps for safety. Intermittently, the cells were allowed to rest for several hours and their capacities were then measured using the same testing procedures as their initial capacity characterizations. Once a cell reached its approximate SoH setpoint the degradation cycling was concluded.

Following degradation cycling, each cell was charged to 5% SoC (reasons for which are explained later) and tested to characterize their ohmic resistance and time constant. The test included a 10-second 2 C charge pulse followed by a 2-minute rest. A typical voltage profile of an LFP cell during characterization testing is shown in Figure 15. The ohmic resistance was calculated by recording the voltage change after one second from the start of the 2 C charge (V2-V1 in the figure) and dividing it by the applied current. The cell time constants (τ) were determined by measuring the amount of time it took voltages to

degrade (from V3, following ohmic voltage drops at the end of the 2C charge pulse) approximately 63.2% towards their values at the end of the rest period (V4). The results of these characterizations are shown in Table 3 and analyzed in section 9.

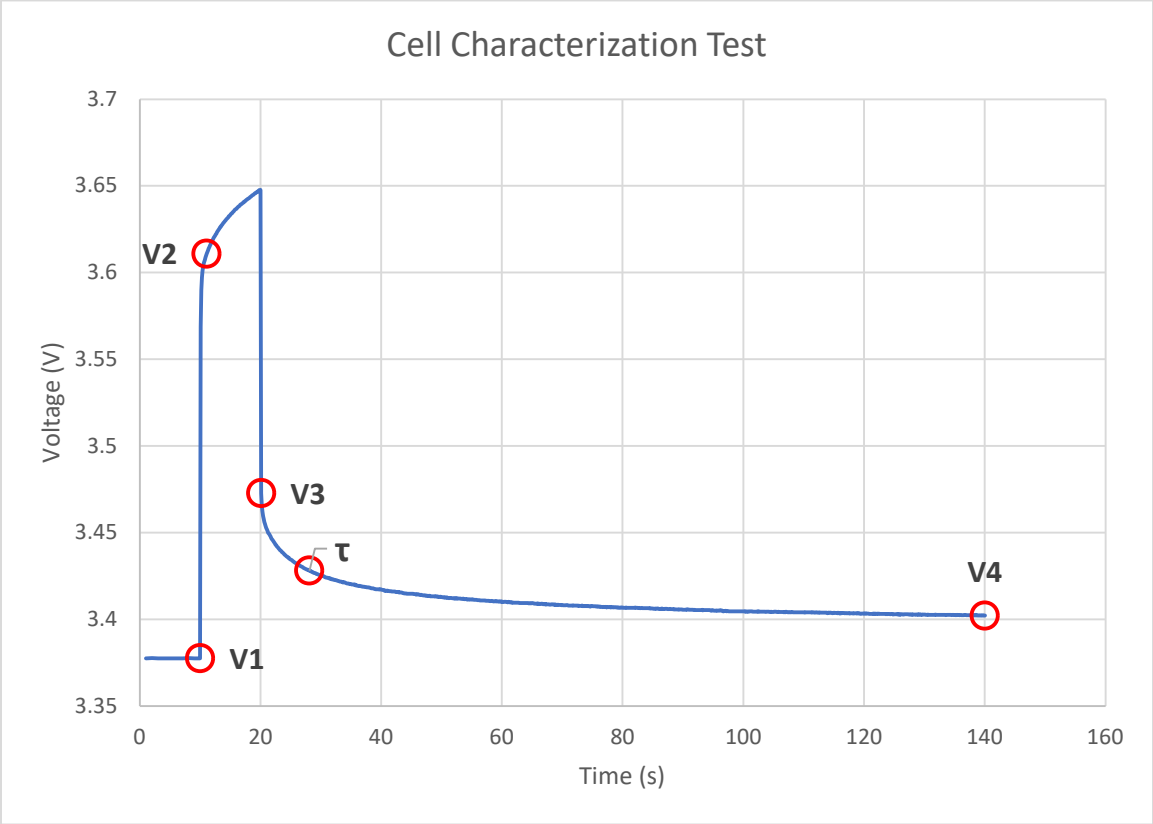

Figure 15: Experimental cell characterization test.

7 Pack Testing Procedures and Setup

Using the experimental cells described in the previous section, packs consisting of four cells in series were formed and tested for this study. Series packs consisting of four cells were chosen due to the voltage limits of the Arbin system. Experimental cells were assembled to form packs that ranged from a pack SoH of 80% (four cells at 80% SoH) to 95% (four cells at 95% SoH) in increments of 1.25% SoH. For each pack SoH setpoint, except for 80% and 95%, there were a multitude of cell SoH combinations that could be used to form a pack. For instance, a pack with four cells at 85% SoH would have the same pack

SoH as a pack with two cells at 90% and two cells at 80% SoH. The number of cells degraded to each setpoint was chosen to allow redundancy to improve the robustness of models and provide the ability to produce various SoH CtCV at each pack SoH setpoint.

In pursuit of increasing the accuracy of the models, the goal was to administer testing procedures that would elicit substantially different pack voltage responses to current pulses among different pack SoH and SoH CtCV. All cells were charged to 5% SoC before testing due to results published by [254] that showed a larger divergence of differently aged cells' SoC-OCV curves for LFP cells at low SoC ranges. A study performed by Nikolian et al. [255] also showed high battery parameter divergence at low SoCs for NMC cells, which have shown to exhibit similar voltage behavior to NCA batteries [249]. A 5% SoC also corresponds to a steeper portion of SoC-OCV curves for both chemistries [256], which would provoke more substantial pack voltage responses to applied current.

Figure 16 shows the 170-second test profile of current pulses applied to the experimental packs. It should be noted that the total Ah charged during the 10-second 2 C pulse were equivalent to the Ah removed during the 80-second 0.25 C discharge pulse. This ensured a 5% SoC was maintained among the cells. The choice of pulse profile was due to the safety constraints of the batteries as well as the desire to produce enough of a divergence in voltage response of the different pack types in a short amount of time. Figure 17 shows the 3D printed test fixture that was designed to quickly form and test the experimental battery packs.

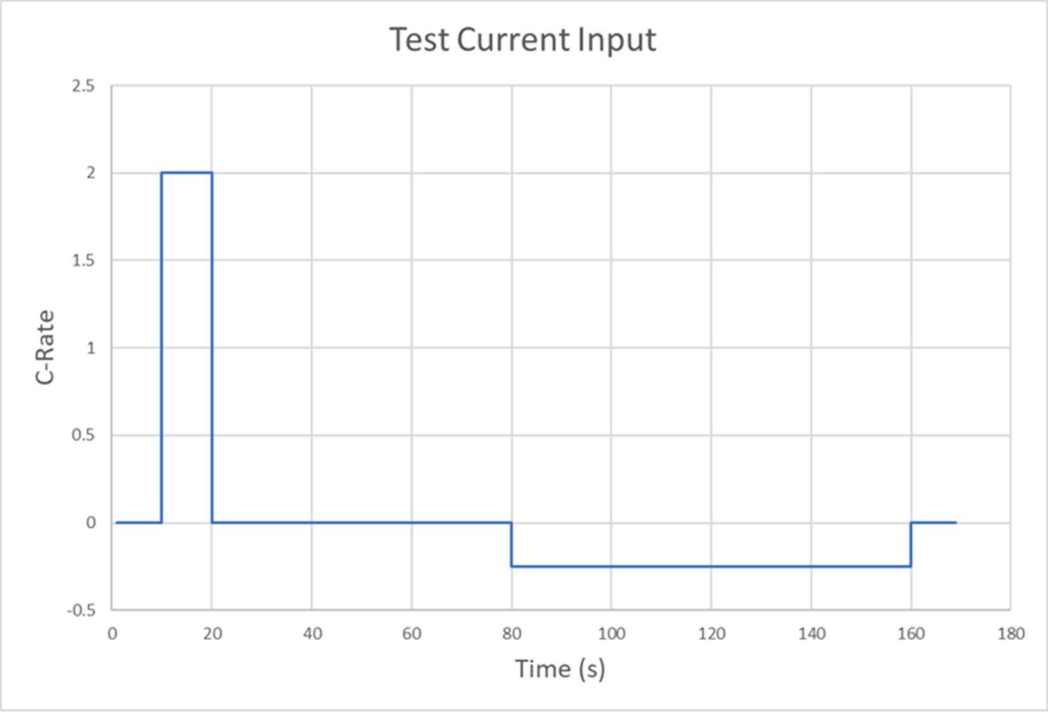

Figure 16: Test profile of current pulses for NCA and LFP packs. A positive C-Rate refers to a charging pulse.

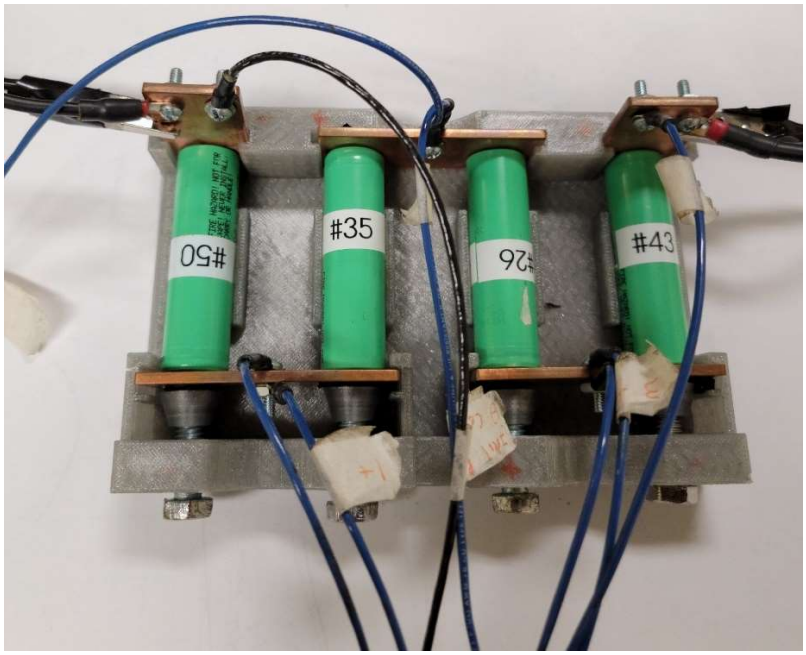

Figure 17: The battery pack test fixture.

8 Pack SoH and CtCV Modeling Procedures

8.1 Data Setup and Processing

There were a total of 140 pulse tests conducted on a variety of packs with different pack SoH and SoH CtCV for each of the NCA and LFP chemistries. The 140 tests were split into 100 tests for training the models and 40 tests for validation (i.e., “testing data set”). The number of tests used to train and test the models at different pack SoH setpoints is illustrated in Figures 18 and 19. The 100:40 ratio of training to testing data is based on the observations in empirical studies which have shown that accurate models can be optimally trained with reduced risk of overfitting when the data is split in a ratio of 70-80% for training and 20-30% for testing [257].

The voltage data for each of the 140 tests was recorded at 100 Hz and then rounded to the nearest second. All voltage readings rounded to the same second were then averaged, producing 170 voltage data points (one for each second of the test) to train and test the models. This was done to reduce the large amount of data points as well as fix any misalignment issues between tests due to the imperfect sampling rates of the Arbin system. Finally, the respective at-rest pack voltage for each test was subtracted from all data points within the test. This made the voltage response used to train and test the models the change in voltage from rest, and not the absolute voltage of the packs. All modeling was performed in RStudio software [258]. Using the same cell characterization methods previously described, raw voltage data from the initial 2 C charge pulse and following rest of the pack test profile was used to determine both pack ohmic resistance and the pack time constant.

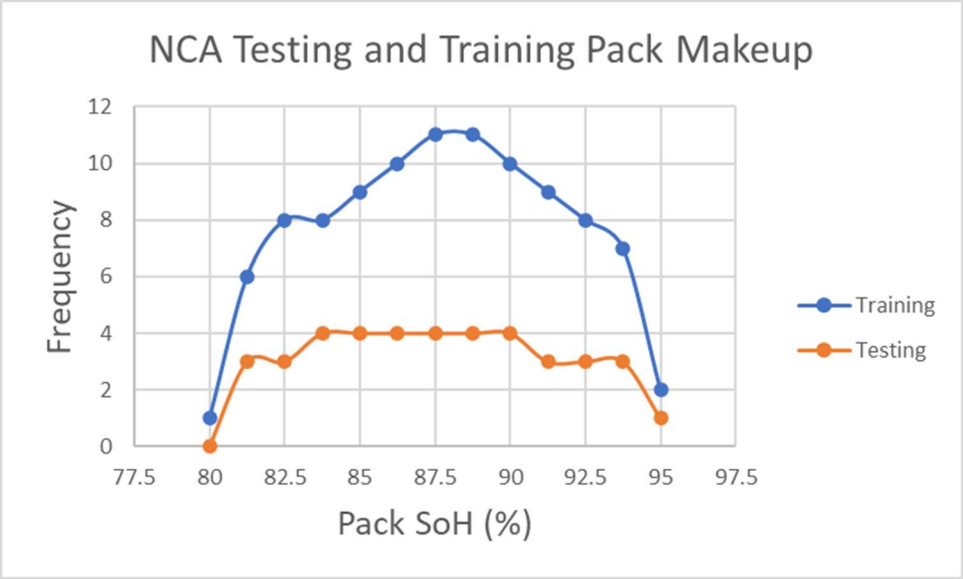

Figure 18: Frequency of different SoH packs used for training and testing data sets for NCA packs.

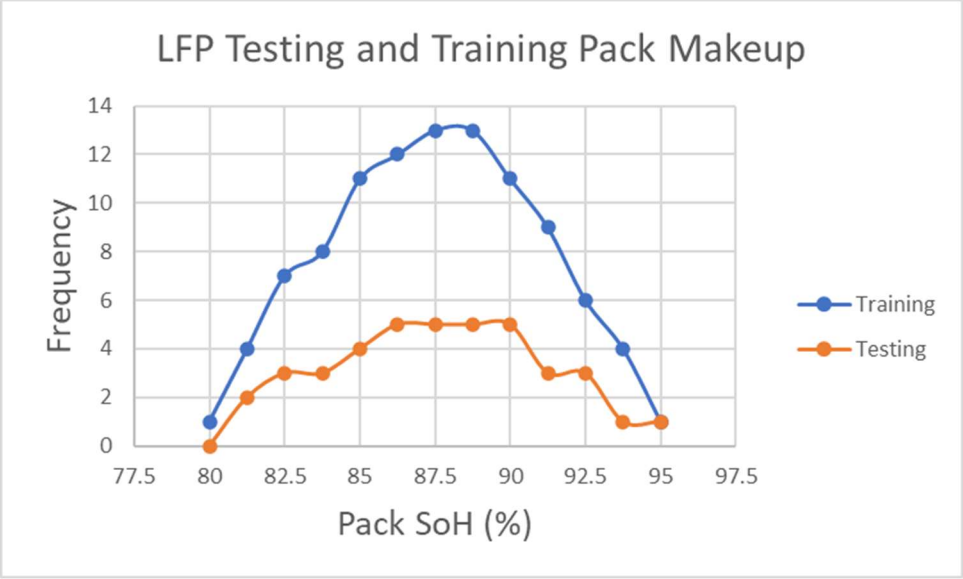

Figure 19: Frequency of different SoH packs used for training and testing data sets for LFP packs.

Pearson's correlation and partial correlation coefficients were calculated to determine the extent of linear relationships between various cell and pack parameters. These were calculated using equations 17 and 18 for the testing data set. All reported correlation metrics were tested for significance at a

confidence level of 95%, using t-statics calculated from equations 19 and 20. An n value of 100 and k value of one was used for these calculations.

8.2 Model Selection and Parameters

Amongst the various modeling methods used in literature this study used empirical models for several reasons. Physics-based models give us details which are easily interpretable, though they require a large number of parameters to be estimated and assumed to build a model [259], [260]. Errors due to inaccurate assumptions are compounded when applied to a pack of several cells in series instead of just one. ICA models on the other hand tend to be quite accurate, but even models optimized for partial discharge still require several minutes to estimate the SoH of a single cell [27], [261]. In comparison, pulse tests such as those used in empirical models and some data-driven models can be completed in a much shorter time duration [27], [262]. Finally, data-driven models generally require a large amount of data and substantial parameter tuning for optimization [196]. Empirical models are more suitable for smaller data sets and there are certain modeling techniques which can be implemented swiftly and easily [29]. For this study, a partial least squares (PLS) regression model was selected.

The independent variables of the model consisted of the voltage response measurements for each pack at each second of the 170-second test. Two main factors which favored the use of PLS models were the fact that there are more variables (170) than number of observations (100) and the large degree of collinearity between the voltage responses at different times in the test [236].

Beyond pack SoH, additional modeling of the SoH CtCV of the packs was performed. As a measure of SoH CtCV, the standard deviation of cell SoH within a pack was modeled using the same variables as the pack SoH model. The pack standard deviation was calculated using equation 54, where σ_{pack} is defined as the pack standard deviation, x_i is an individual cell SoH, and μ is the average cell SoH in a pack.

$$\sigma_{pack}(\%) = \sqrt{\frac{\sum_{i=1}^{4}(x_i - \mu)^2}{4}} \tag{54}$$

The PLS regression models for both SoH and SoH CtCV are represented in equation 55. The 100 observations from the training data set are indicated by the row in the variable subscripts. V is the voltage response at a given second denoted by the column in the subscript, "MinCell" is the minimum cell SoH within a pack, and y is either the pack SoH or σ_{pack} for the corresponding models.

$$\begin{bmatrix} y_1 \\ y_2 \\ \vdots \\ y_{100} \end{bmatrix} = \begin{bmatrix} 1 & V_{1,1} & V_{1,2} & \cdots & V_{1,170} & MinCell_1 \\ 1 & V_{2,1} & V_{2,2} & \ddots & V_{1,170} & MinCell_2 \\ \vdots & \vdots & \vdots & \ddots & \vdots & \vdots \\ 1 & V_{100,1} & V_{100,2} & \cdots & V_{100,170} & MinCell_{100} \end{bmatrix} \begin{bmatrix} \beta_0 \\ \beta_{PLS,V_1} \\ \vdots \\ \beta_{PLS,MinCell} \end{bmatrix} + \begin{bmatrix} \epsilon_1 \\ \epsilon_2 \\ \vdots \\ \epsilon_{100} \end{bmatrix} \tag{55}$$

Models predicting pack SoH and σ_{pack} for both chemistries were designed both with and without the inclusion of the MinCell variable. This was for several reasons. Firstly, in efforts to produce a model as simple as possible, the efficacy of solely using pack terminal voltage data was explored. Secondly, considering all cells maintained the same SoC throughout testing, it is reasonable to assume MinCell to be the power- and capacity-limiting cell in the series pack. Comparing models with and without MinCell would quantify the significance of including the impactful cell.

8.3 Model Validation

The number of PLS latent variables selected for all final models were determined based on the minimum MSE found using LOOCV on the training data sets for models containing up to 20 latent variables. LOOCV was employed due to the small size of the training data set. Once the number of latent variables to include was determined, the models were trained using the training data sets. These trained models were then used to provide pack SoH or σ_{pack} estimations for the testing data sets. The final accuracy of

the models' predictions for the testing data sets were reported in terms of the MAE, RMSE, and MaxAE. Additionally, for increased interpretability the standard deviations of the packs were categorized into low, medium, and high (L/M/H) standard deviation packs.

L/M/H categorization was performed by dividing the training set packs' standard deviations into terciles. Packs with standard deviations in the lower third of all training pack standard deviations were defined as having "low" standard deviation and so on for "medium" and "high" standard deviation packs. The accuracy of the standard deviation models was also reported as a function of how often the models' predictions on the testing data sets correctly corresponded to their L/M/H ranking. The models did not directly predict a pack's L/M/H classification, however. For example, if the lowest tercile of the training data set was from 1% to 3%, and the model predicted a testing pack's standard deviation as 4% (corresponding to a medium ranking) when the testing pack's actual standard deviation was 2% (corresponding to a low ranking), the prediction would be considered incorrect. If 30 out of 40 packs in the testing data set were correctly categorized in the proper L/M/H rankings, the model would be reported to have a categorization accuracy of 75%.

Part IV. Results and Discussion

9 Cell-Level Analysis

The results of the cell characterization tests are shown in Table 3. The correlative relationships between the extracted cell parameters and cell SoH were analyzed and are presented in Table 4. Results show a statistically significant negative linear relationship between the cell ohmic resistance values and SoH for both chemistries, as evidently shown in Figures 20 and 21. This result was expected and confirmed by the literature, which is detailed in section 4.1.3.

Table 3: Experimental cell characterization results.

	NCA			LFP		
Cell Number	SoH (%)	Ohmic Resistance (mΩ)	Time Constant (s)	SoH (%)	Ohmic Resistance (mΩ)	Time Constant (s)
1	95.5	34.3	11.8	95.1	78.3	11.8
2	95.4	53.0	11.9	94.7	82.2	12.4
3	94.9	36.0	10.0	94.6	80.7	11.2
4	94.8	33.5	11.7	94.6	83.3	12.0
5	93.8	38.6	10.2	94.6	77.0	12.8
6	91.1	33.5	10.1	90.3	80.3	14.3
7	91.1	42.9	9.3	90.0	80.1	14.6
8	91.1	38.2	11.5	89.9	85.6	14.0
9	90.5	45.9	9.5	88.9	84.6	12.7
10	86.5	52.1	9.1	86.5	89.3	14.0
11	85.7	44.0	8.3	85.1	82.4	13.5
12	85.3	52.4	7.6	85.1	88.5	14.5
13	85.2	46.7	8.1	84.8	90.8	13.2
14	81.2	66.8	5.9	83.4	89.7	13.3
15	81.0	54.0	5.8	81.1	92.8	15.1
16	81.0	54.3	7.9	80.4	86.8	12.7
17	80.0	94.3	4.0	79.6	99.8	12.3
18	-	-	-	79.6	94.7	12.7

Table 4: Experimental cell parameter correlations. (NSS = Not statistically significant at 95% confidence level)

Correlations	NMC	LFP
Cell SoH vs Cell Ohmic Resistance	-0.74	-0.85
Cell SoH vs τ	0.92	NSS

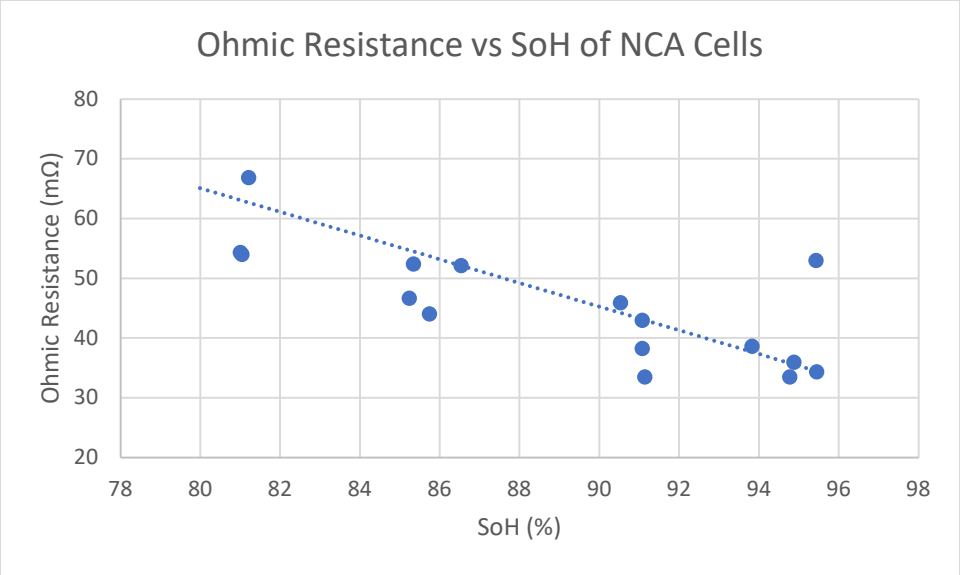

Figure 20: The ohmic resistance of experimental NCA cells vs SoH. A line of best fit included to show the linearity of the relationship.

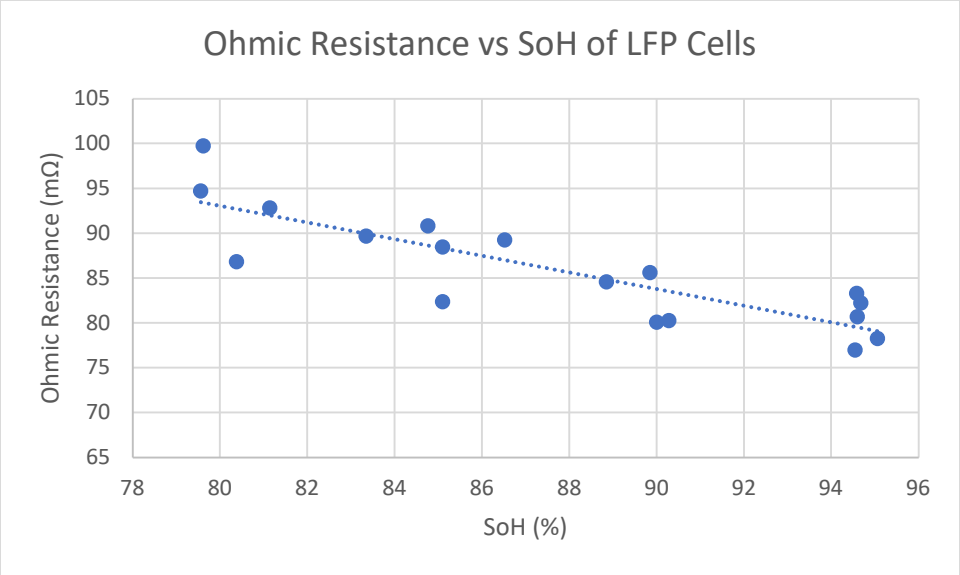

Figure 21: The ohmic resistance of experimental LFP cells vs SoH. A line of best fit included to show the linearity of the relationship.

The NCA cell time constant values showed a strong positive linear correlation with SoH, meaning as the cells aged their time constant values decreased. Figure 22 shows this trend clearly. These findings are in agreement with the results from Attidekou et al. [242], who looked at the time constant values of NMC

voltage relaxation curves. Voltage relaxation curves refer to the nonlinear voltage response that occurs as a battery slowly approaches OCV after the cessation of a current pulse. While Attidekou et al. [242] used NMC cells and not NCA cells, there has been a noted similarity in the shape and magnitude of the relaxation curves of NMC and NCA cells in the literature [249].

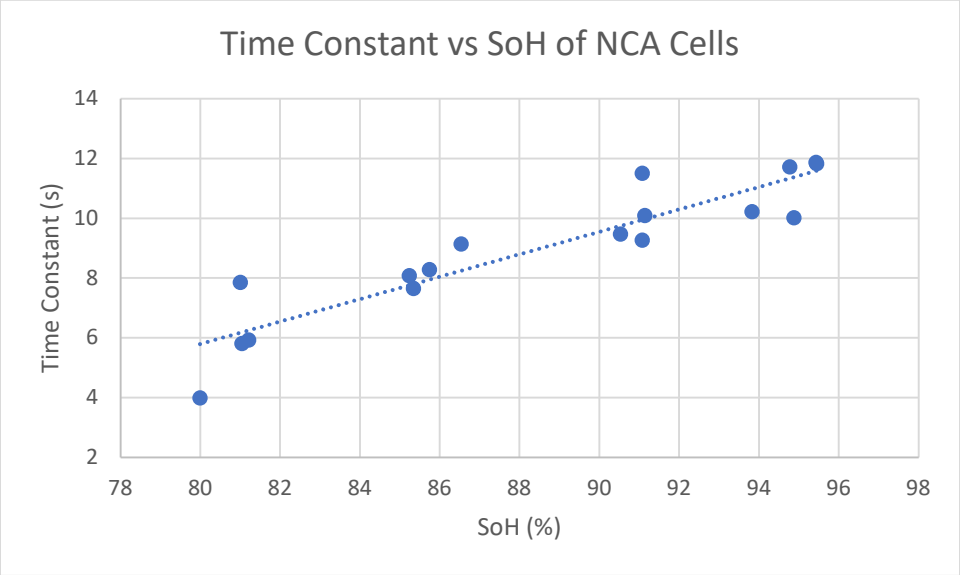

Figure 22: The voltage relaxation curve time constant of experimental NCA cells vs SoH. A line of best fit included to show the linearity of the relationship.

Figure 23 shows the voltage relaxation curves of a representative subset of the experimental NCA cells used in this study. These curves show the cell voltage response over time following the initial ohmic drop after the removal of a 2 C charge pulse. The existence of a relationship between cell SoH and the shape and magnitude of voltage relaxation curves is evident. The rapid initial voltage decay and overall magnitude of the voltage change in relation to cell SoH is consistent with the literature [50], [263]–[266]. The steepening slope of the initial voltage response as SoH decreases explains the positive relationship between the time constant and SoH. The steeper slope of a highly degraded cell means that its voltage decays 63.2% towards OCV over a shorter period of time.

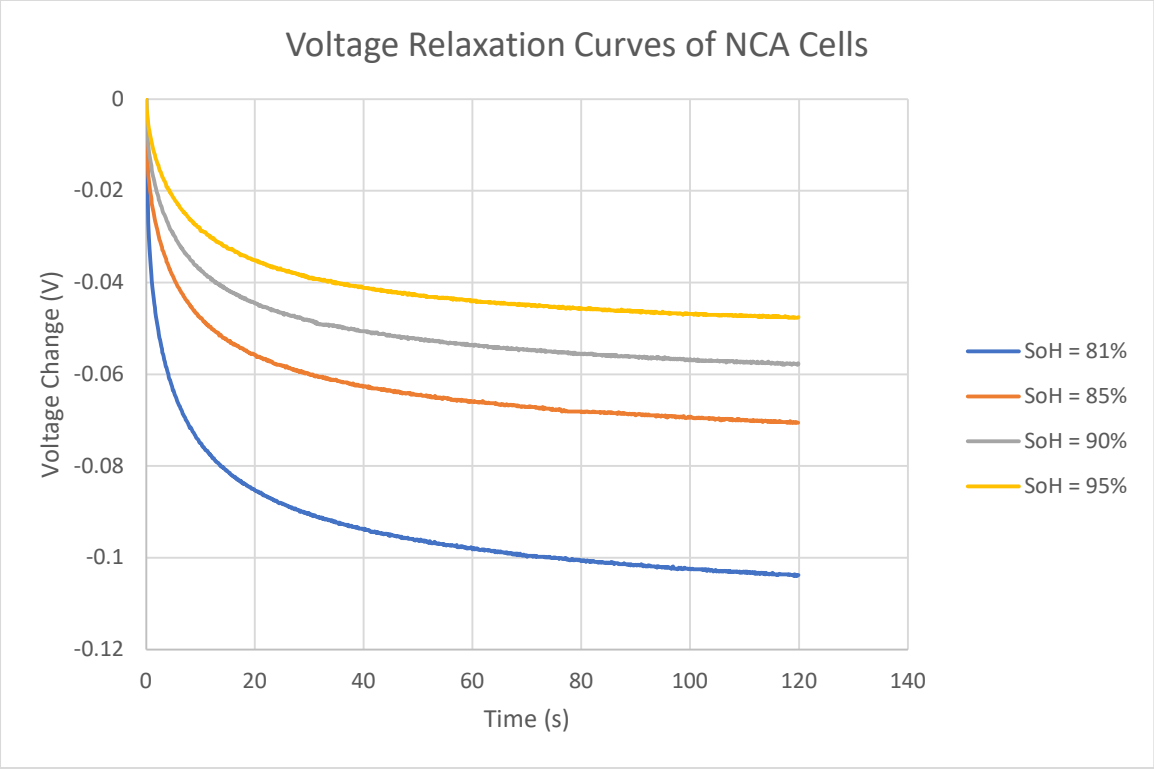

Figure 23: Voltage relaxation curves over time of experimental NCA cells of various SoH. The y-axis shows the voltage change of the cells following the ohmic drop after the cessation of a 2C charge pulse.

The LFP cells did not show a statistically significant linear correlation between cell SoH and time constant values. This makes sense when looking at Figure 24 and the representative LFP voltage relaxation curves in Figure 25. The lack of clear correspondence between cell SoH and the relaxation curves is also supported by the literature [264].

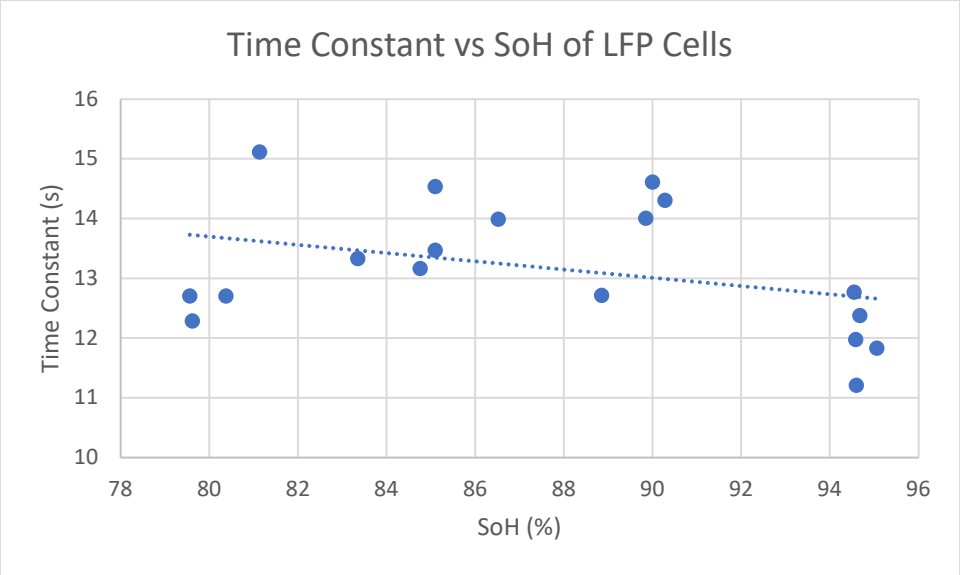

Figure 24: The voltage relaxation curve time constant of experimental LFP cells vs SoH. A line of best fit included to show the linearity of the relationship.

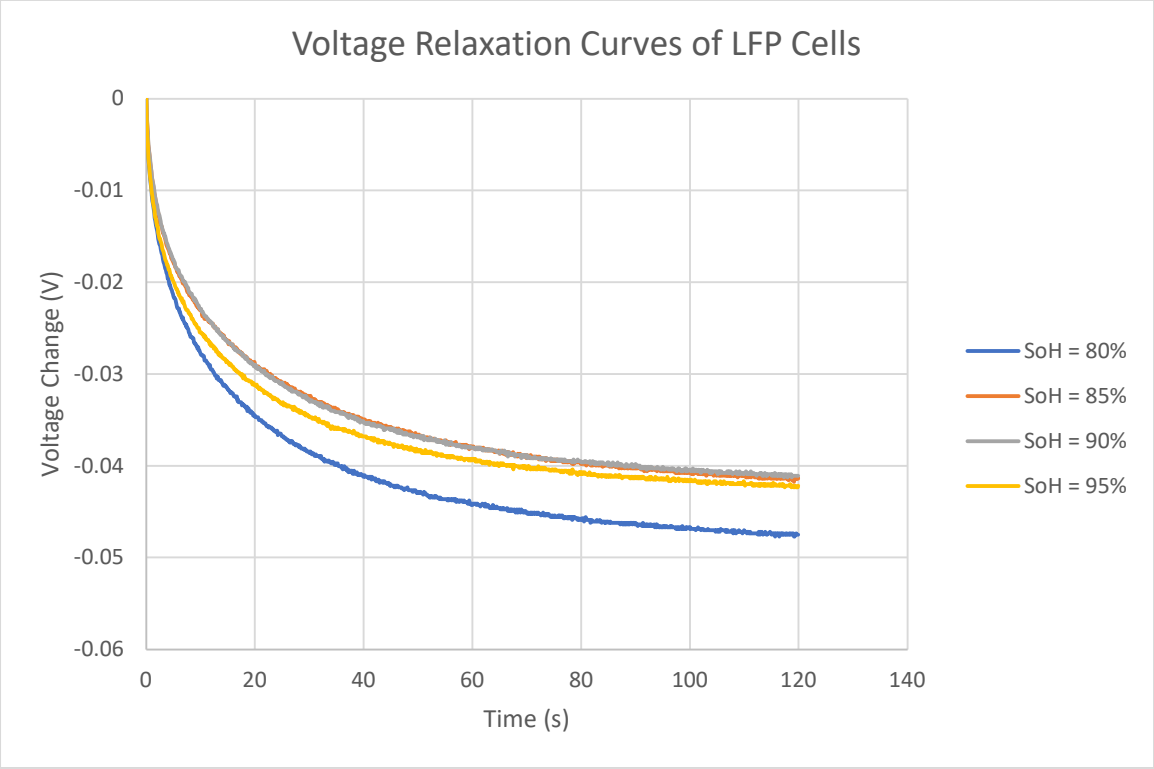

Figure 25: Voltage relaxation curves over time of experimental LFP cells of various SoH. The y-axis shows the voltage change of the cells following the ohmic drop after the cessation of a 2C charge pulse.

In order to anticipate how the cell battery parameters will affect pack-level voltage behaviors upon assembly, it is useful to conceptualize the battery pack as a series of individual cell equivalent circuits. In the Thévenin model (described in section 5.4.3), the ohmic resistance and battery time constant can be analogized to a series resistor and RC subcircuit, respectively. Therefore, when cells are placed in series the expectation should be that the ohmic resistances have an additive effect, and the relationships between SoH and ohmic resistance should map closely from the cell to the pack-level. The RC pairs, however, would have a more complicated voltage response when placed in series, and the SoH-time constant relationship at the cell level would not clearly translate to the pack-level.

10 Pack SoH vs Voltage Response

The average voltage response of packs with various pack SoH setpoints is illustrated in Figures 26 and 27. Both the NCA and LFP chemistries show significant deviations in voltage response across the various pack SoH setpoints during the test profile. The voltage response of the packs can be attributed generally into three categories: a change in OCV due to a change in SoC, an immediate voltage jump from a change in current due to the ohmic resistance, and the dynamic diffusion voltage response of the cells. The extent to which these mechanisms play a role in the voltage response of NCAs and LFPs varies and is exhibited in differences between Figures 26 and 27.

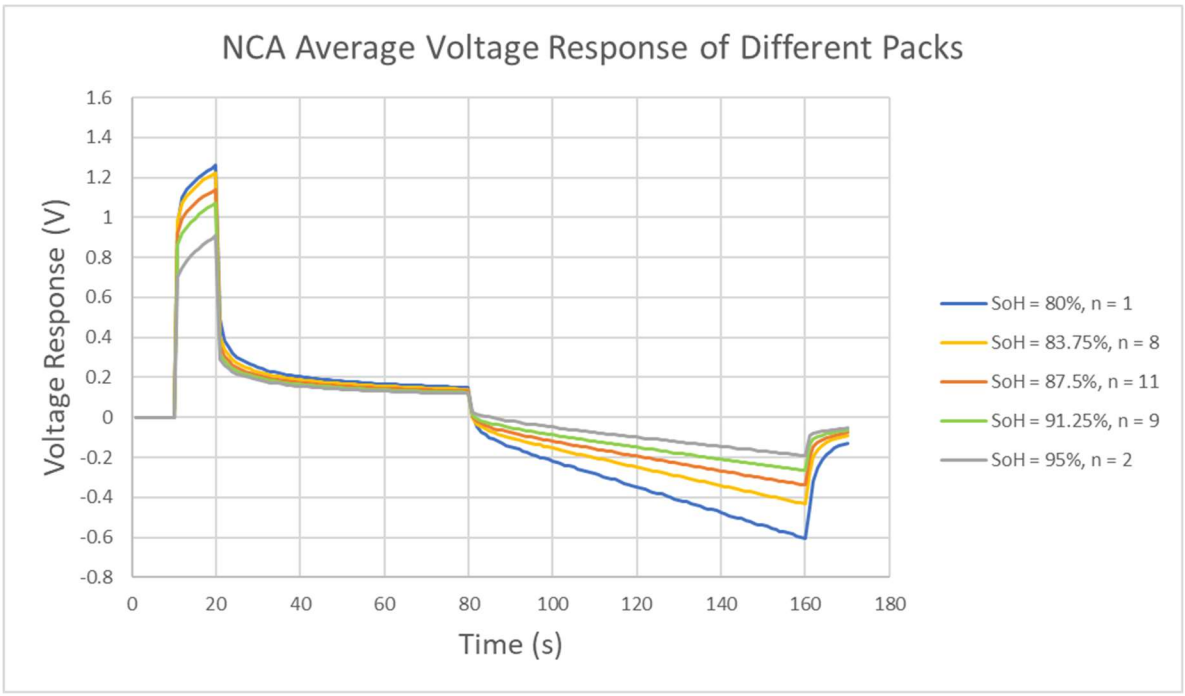

Figure 26: Average voltage response, relative to at rest voltage, of NCA packs from testing data set with various total SoH. Number of packs included in averages, n, specified in figure legend.

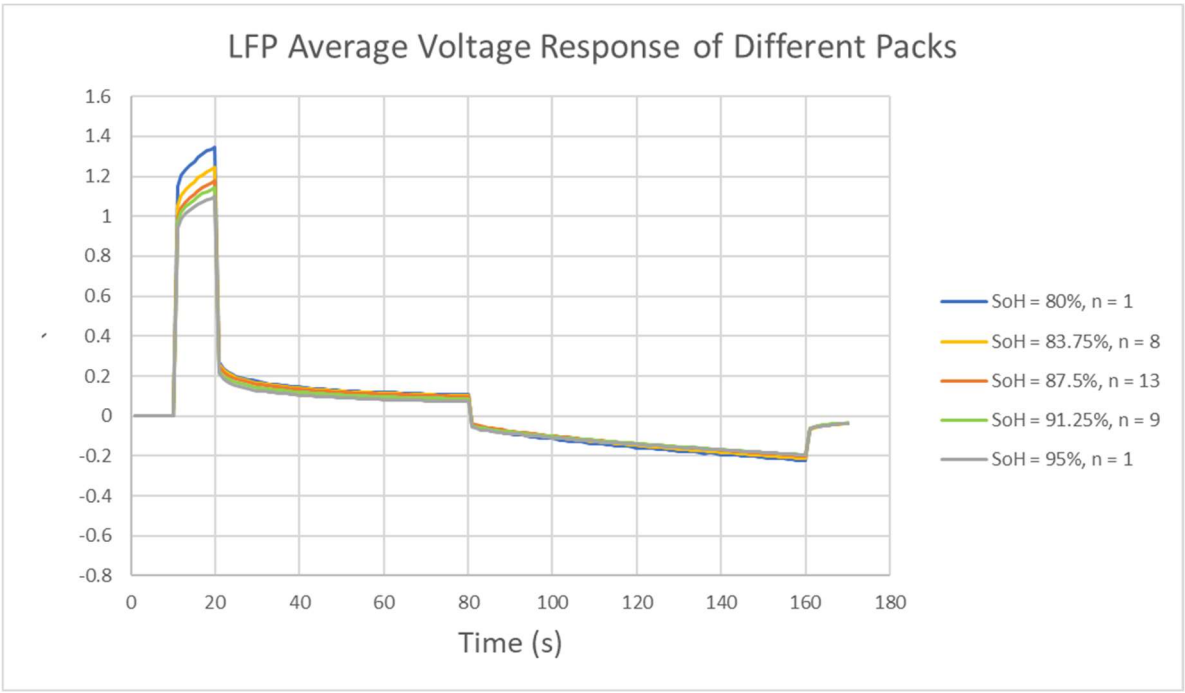

Figure 27: Average voltage response, relative to at rest voltage, of LFP packs from testing data set with various total SoH. Number of packs included in averages, n, specified in figure legend.

There are several similarities, however, shown among the voltage responses of the different chemistries. Firstly, close examination of Figures 26 and 27 shows the NCA and LFP packs having minimal voltage deviation after an extended rest period (near 80 seconds into the test). This would allude to the voltage changes between packs in OCV due to SoC change being minimal for both chemistries. Next, Figures 26 and 27 show a variation between pack SoH setpoints in immediate voltage changes as current is applied or removed at seconds 10, 20, 80, and 160. This exemplifies the inverse relationship between ohmic resistance and SoH for NCAs and LFPs, which did indeed maintain the same relationships identified at the cell-level, as shown by the pack-level correlation data in Table 5 and Figures 28 and 29. The extent to which these relationships weakened from the cell- to pack-level may be due to experimental error, such as inconsistent contact resistance between cells in the pack test fixture. Nonetheless, these relationships were found to be significant and the difference in the strength of correlation amongst the two chemistries remained consistent from cell- to pack-level.

Table 5: Pack-level parameter correlations. (NSS = Not statistically significant at 95% confidence level)

Correlations	NMC	LFP
Pack SoH vs Pack Ohmic Resistance	-0.54	-0.68
Pack SoH vs τ_{pack}	0.91	NSS
τ_{pack} vs |Discharge Slope|	-0.90	0.28

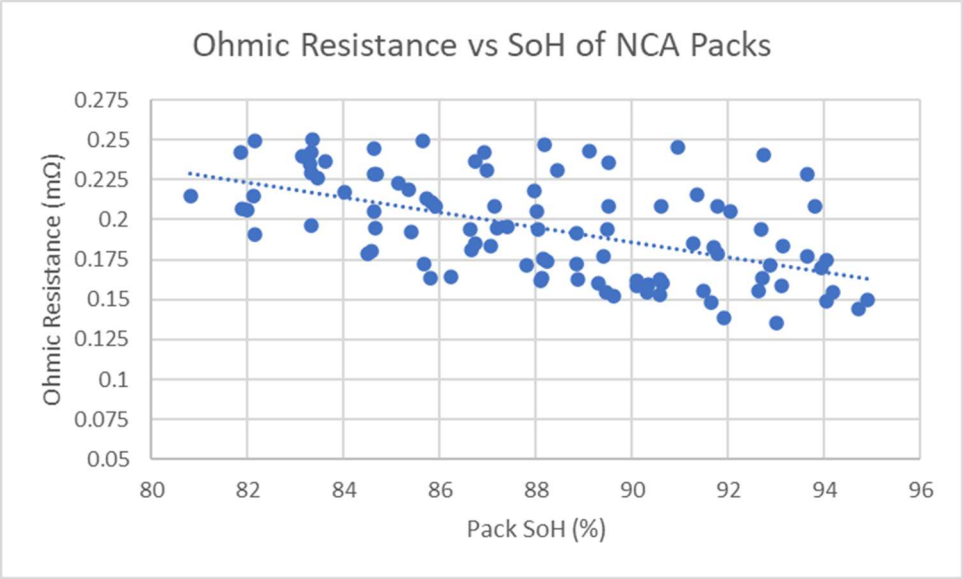

Figure 28: The ohmic resistance of experimental NCA packs vs SoH. A line of best fit included to show the linearity of the relationship.

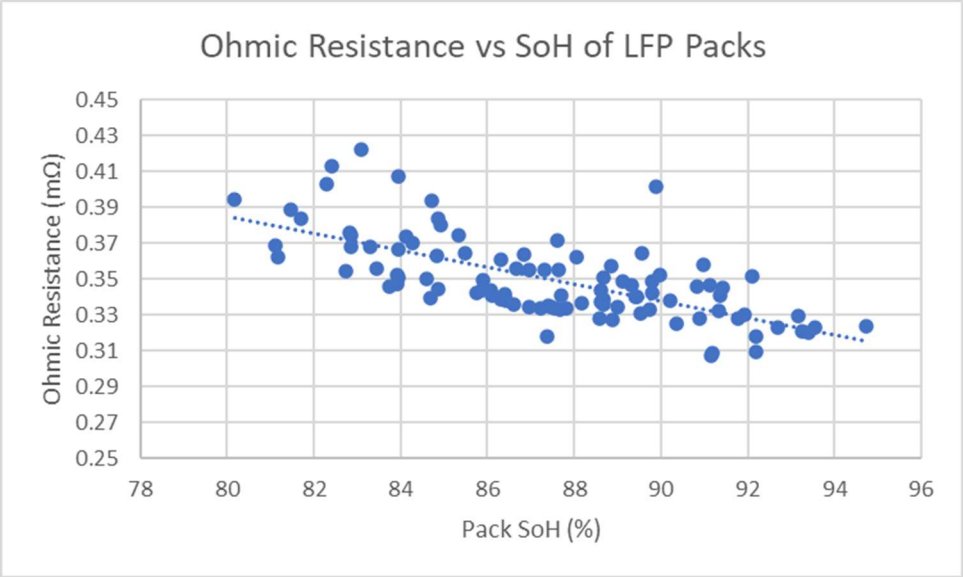

Figure 29: The ohmic resistance of experimental LFP packs vs SoH. A line of best fit included to show the linearity of the relationship.

The most glaring differences between the chemistries occurs during the extended low-current discharge from seconds 80 to 160. The NCA packs show a wide deviation in voltage response during this time, while the LFP packs show minimal differences amongst the different pack SoH setpoints. This is

explained by the calculated correlation coefficient values for pack SoH and a pack's time constant (a proxy for pack dynamics), τ_{pack}. The ρ value describing the relationship between pack SoH and τ_{pack} was 0.91 for the NCA packs, while this relationship was statistically insignificant for the LFP packs. Figures 30 and 31 provide supporting context to these results, which show consistency with the cell-level parameter relationships previously discussed. Additional analysis showed that the absolute slope of the voltage response from seconds 85 to 160 for NCA packs has a strong correlation to τ_{pack}, with a ρ value of -0.90. In contrast, this relationship showed very weak for LFP packs with a corresponding ρ value of 0.28. In summary, the slope of the pack voltage response appears to closely represent the pack dynamics.

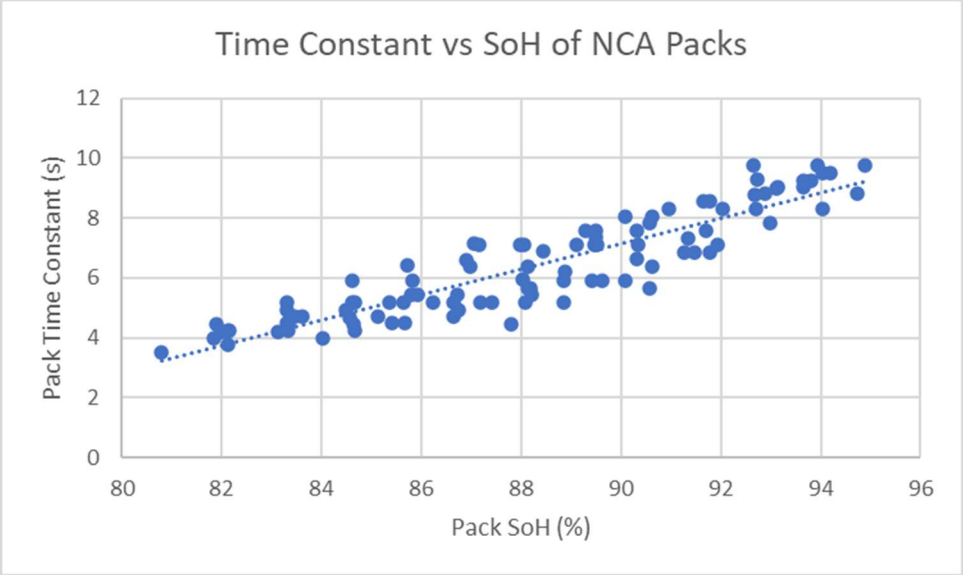

Figure 30: The voltage relaxation curve time constant of experimental NCA packs vs SoH. A line of best fit included to show the linearity of the relationship.

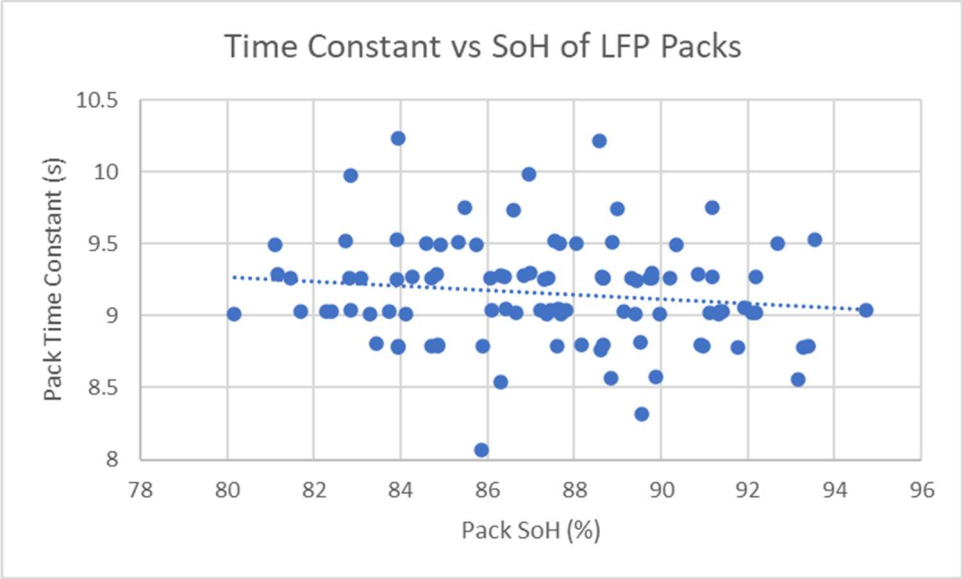

Figure 31: The voltage relaxation curve time constant of experimental LFP packs vs SoH. A line of best fit included to show the linearity of the relationship.

11 Pack SoH Model Results

The final pack SoH PLS models including MinCell for the NCA and LFP packs contained 9 and 4 latent variables, respectively. The results of the cross-validation procedures for both chemistries are shown in Figures 32 and 33.

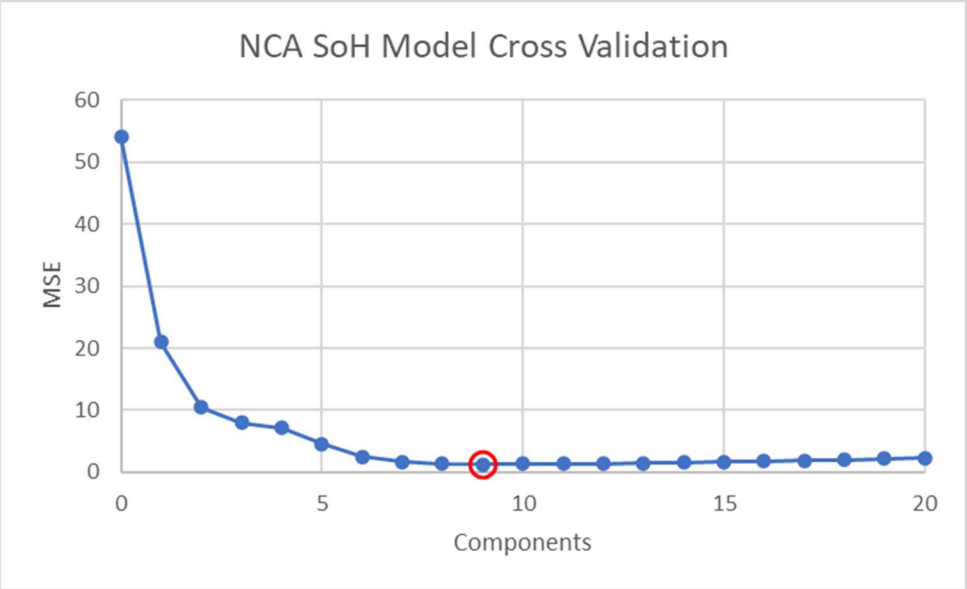

Figure 32: Results from leave-one-out cross-validation procedure for NCA pack SoH model. The MSE of the packs is shown to change as more latent variables are included in the model. The minimum MSE for the number of latent variables tested is circled in red. This corresponds to the number of latent variables included in the final NCA pack SoH model.

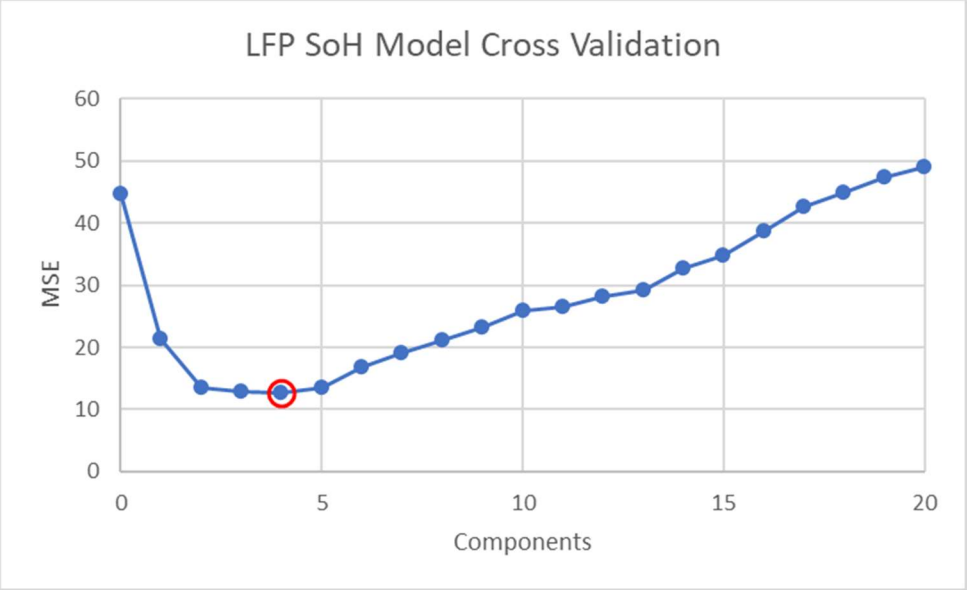

Figure 33: Results from leave-one-out cross-validation procedure for LFP pack SoH model. The MSE of the packs is shown to change as more latent variables are included in the model. The minimum MSE for the number of latent variables tested is circled in red. This corresponds to the number of latent variables included in the final LFP pack SoH model.

The accuracy of the NCA and LFP SoH models' predictions for the testing data sets are reported in Table 6. Results show that the NCA pack SoH model is substantially more accurate when compared to the LFP model. This appears reasonable, considering the NCA packs had a much more diverse voltage response amongst different pack SoH compared to the LFP packs. With a stronger association between pack SoH and pack voltage response the model was able to leverage these relationships to produce higher accuracy estimates.

Table 6: Pack SoH and Pack Standard Deviation model results for NCA and LFP packs. Mean Absolute Error (MAE), Root mean squared error (RMSE) and Maximum Absolute Error (MaxAE) reported. Categorization Accuracy refers to the percentage the model correctly estimated if a pack was in the Low, Medium, or High standard deviation ranking.

		Pack SoH Model			**Pack Standard Deviation Model**			
		MAE (% SoH)	RMSE (% SoH)	MaxAE (% SoH)	MAE (% SoH)	RMSE (% SoH)	MaxAE (% SoH)	Categorization Accuracy (%)
MinCell Included	NCA	0.38	0.47	1.09	0.69	0.84	1.83	72.5
	LFP	1.43	1.92	6.58	0.77	1.02	2.35	65
MinCell Excluded	NCA	0.41	0.51	1.12	1.43	1.7	4.74	43.59
	LFP	8.50	10.99	26.67	12.62	15.14	31.18	20

Including MinCell in the model drastically improved the accuracy for the LFP packs and only marginally improved the NCA pack SoH model. To contextualize the accuracy of these SoH models, various studies in the literature have set a threshold of acceptable accuracy under 3-5% cell SoH error [154], [267], [268]. In addition, the model performed very well in comparison to the studies reported in Table 2. Considering these studies and the thresholds of acceptable error were based on cell SoH models, the accuracy of the pack SoH models are especially impressive. For the LFP packs, including MinCell was required to meet the threshold standard. Even so, the ability to produce an accurate model using the data from pack voltage terminals and the weakest cell in the pack is substantially less burdensome than modeling the SoH of all individual cells in the pack. In practical applications, the pack performance-

limiting cell(s) can be easily identified based on the weakest cells reaching upper and lower cutoff voltages first. The added computational resources required for SoH estimation of the weakest cells may be reasonable to accommodate for a BMS, especially considering the simplicity of the PLS estimation procedure. The NCA pack SoH model that solely relied on pack-level voltage data was extremely accurate. Results indicate that these modeling procedures may work especially well for cell chemistries in which dynamic behavior is strongly affected by cell aging and may not require any information at the cell-level.

The under 3-minute testing time makes these procedures immensely advantageous over other testing methods, such as EIS or ICA. The ease of data collection and lack of reliance on historical battery usage data provides additional advantages over pack-level models found in the literature and various data-driven methods. While the size of the experimental packs pale in comparison to that of an ESS or EV pack, the results and methodology outlined in this dissertation provide a roadmap for further experimentation. Moreover, given the modularity of large battery packs that are a combination of smaller battery strings and modules, these techniques may offer critical simplification to estimate SoH at resolutions above the cell-level.

12 Pack CtCV vs Voltage Response

The average voltage response of NCA and LFP packs with the same SoH setpoints, but different standard deviation rankings (i.e., L/M/H), was investigated. Representative illustrations of the apparent relationship (or lack thereof) between σ_{pack} and voltage response for both chemistries are shown in Figures 34 through 37.

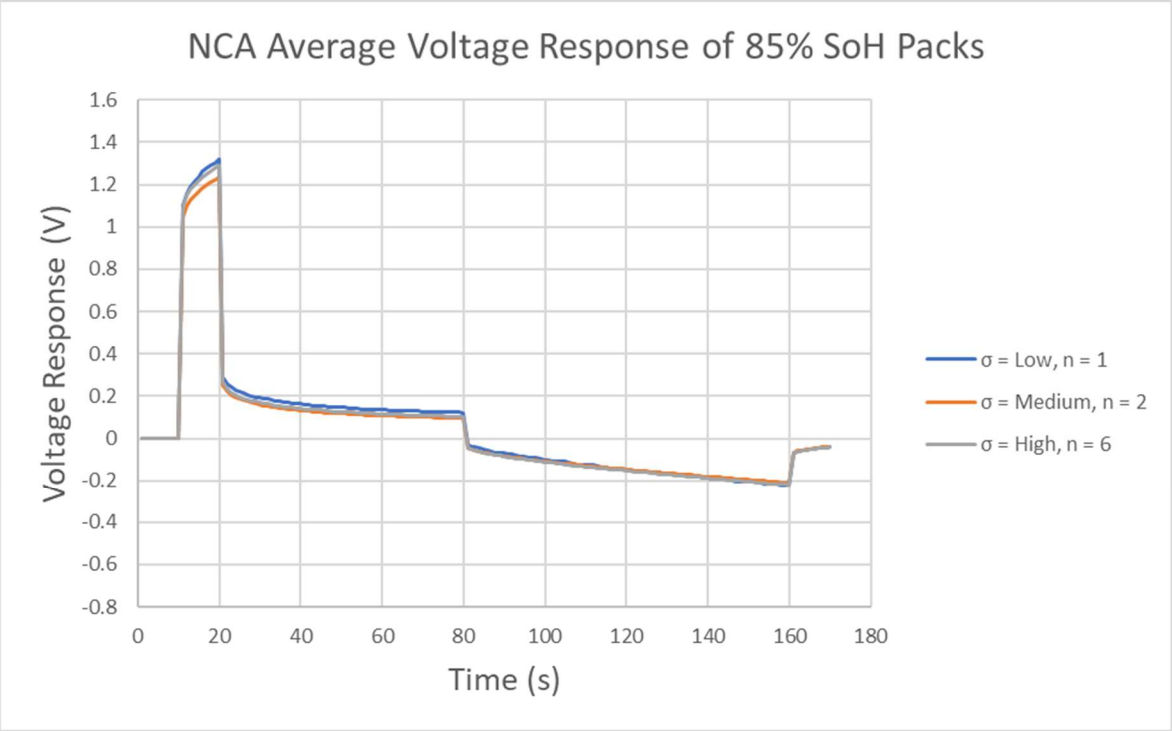

Figure 34: Average voltage response, relative to at rest voltage, of 85% SoH NCA packs with different standard deviation (σ) rankings. Number of packs included in averages, n, specified in figure legend.

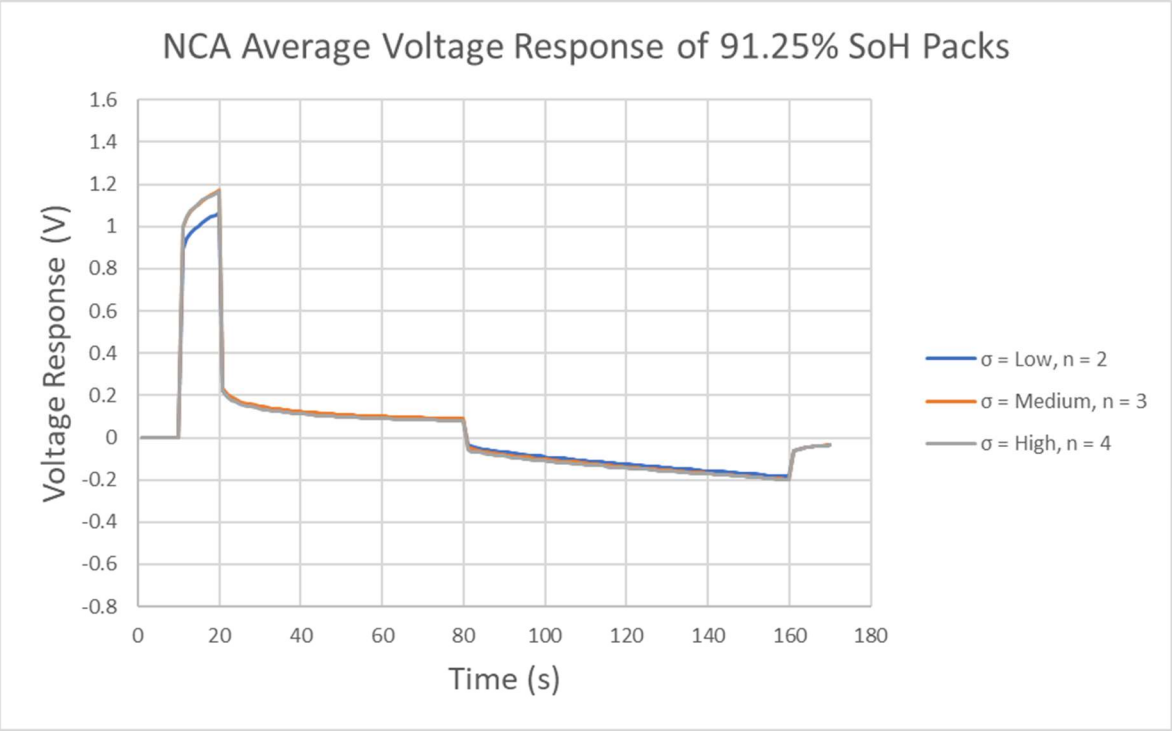

Figure 35: Average voltage response, relative to at rest voltage, of 91.25% SoH NCA packs with different standard deviation (σ) rankings. Number of packs included in averages, n, specified in figure legend.

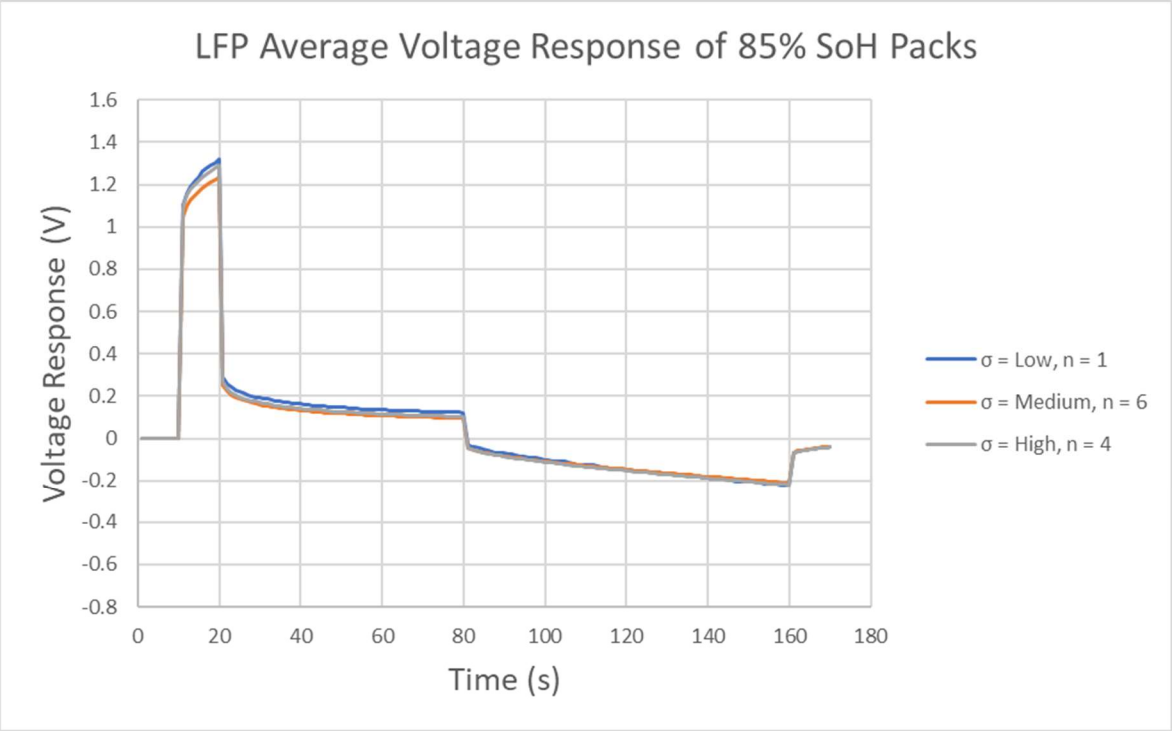

Figure 36: Average voltage response, relative to at rest voltage, of 85% SoH LFP packs with different standard deviation (σ) rankings. Number of packs included in averages, n, specified in figure legend.

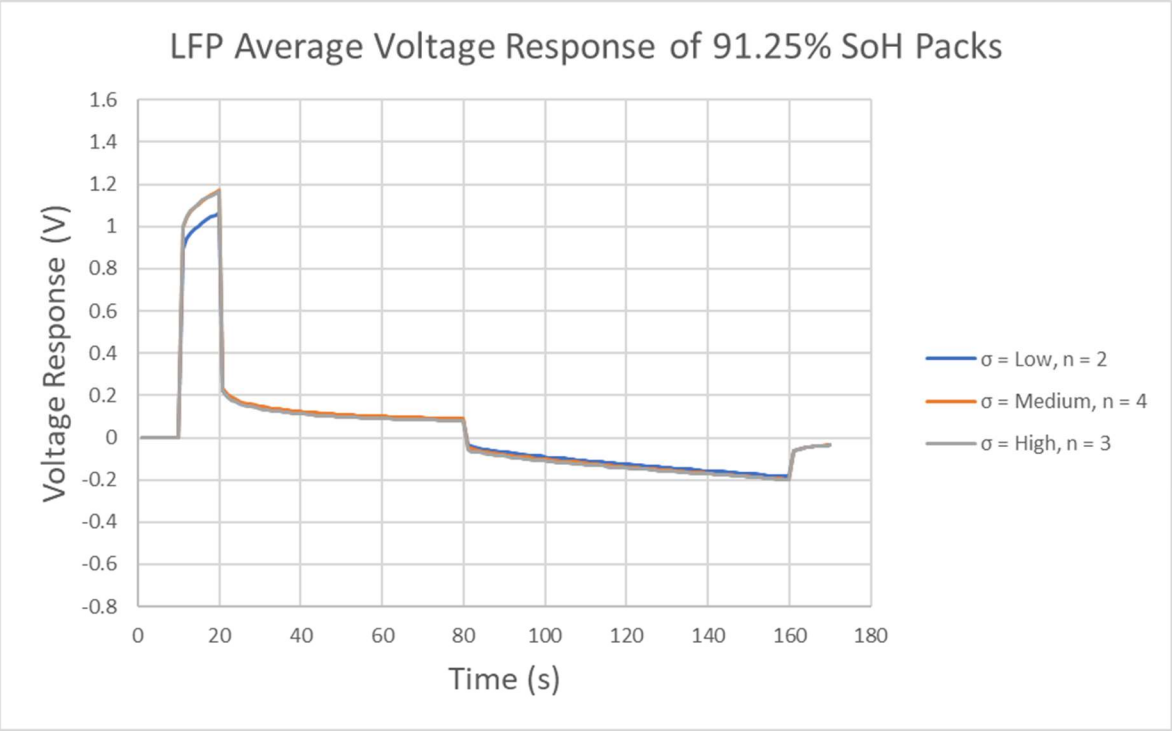

Figure 37: Average voltage response, relative to at rest voltage, of 91.25% SoH LFP packs with different standard deviation (σ) rankings. Number of packs included in averages, n, specified in figure legend.

While the relative magnitude of voltage response was seemingly random between L/M/H packs for both chemistries across multiple pack SoH setpoints, one parameter did consistently behave in accordance with pack ranking for NCA packs. For NCA packs, regardless of which pack ranking had experienced the largest average voltage response during the 10-second charging pulse, the slope of the voltage response during the discharge pulse was always in rank order. Specifically, the smallest absolute slope corresponded to the "Low" standard deviation ranked packs (i.e., the most homogenous packs), the next highest were "Medium" packs, and the steepest slopes corresponded to "High" standard deviation packs. This relationship was always true during the discharge pulses across all pack SoH setpoints where each L/M/H ranking was represented. This relationship did not extend to the LFP packs, most likely due to the aforementioned weak relationship between discharge slope and LFP pack dynamics.

In order to further investigate the relationships between pack voltage response and pack standard deviation (i.e., SoH CtCV), it was necessary to isolate and parse out the relationships between pack voltage response and pack SoH established in section 10. To that end, partial correlations were calculated for various pack parameters, controlling for the parameters' relationships to pack SoH. Key findings of this analysis are demonstrated in Table 7.

Table 7: Partial correlation coefficient values for NCA and LFP packs, controlling for pack SoH interactions. (NSS = Not statistically significant at 95% confidence level)

Partial Correlations	NMC	LFP
ρ (τ_{pack}, $\tau_{MinCell}$)	0.68	0.26
ρ (τ_{pack}, τ of 2nd lowest SoH cell in pack)	NSS	0.21
ρ (τ_{pack}, τ of 3rd lowest SoH cell in pack)	-0.32	0.31
ρ (τ_{pack}, τ of highest SoH cell in pack)	-0.50	NSS
ρ (σ_{pack}, $\tau_{MinCell}$)	-0.65	NSS
ρ (σ_{pack}, τ_{pack})	-0.70	NSS
ρ (σ_{pack}, Pack ohmic resistance)	0.02	NSS
ρ (|Discharge slope|, σ_{pack})	0.24	-0.23
ρ (|Discharge slope|, τ_{pack})	-0.41	0.25
ρ (|Discharge slope|, $\tau_{MinCell}$)	-0.56	0.20
ρ (|Discharge slope|, Pack ohmic resistance)	NSS	NSS

Results showed that for NCA packs the lowest SoH cell (i.e., MinCell) dominated the overall pack's dynamics, with a partial correlation coefficient value for τ_{pack} and $\tau_{MinCell}$ of 0.68. This correlation was much stronger compared to τ_{pack} and any other cell's time constant. This therefore may explain the moderately strong relationship found between σ_{pack} and $\tau_{MinCell}$, which had a partial ρ value of -0.65 for NCA packs. Considering packs with higher standard deviation will inherently have a lower minimum cell SoH compared to homogenous packs of the same total SoH, the dynamics of the packs will be different due to the substantial influence of the minimum SoH cell. Therefore, the time constant of a pack can offer insight into the SoH CtCV of an NCA pack relative to other packs of the same SoH. Given the outsized influence of the weakest cells on pack power and energy capacity in series packs, it would appear the impact of these cells extends even further. These findings provide novelty to the CtCV diagnostic literature, as SoH CtCV has seldom been truly isolated as a variable for inspection, especially at multiple pack SoH.

Regarding the voltage response slope and σ_{pack} relationship observed, the partial ρ value showed a weak relationship between the two with a value of only 0.24 for NCA packs. Given the moderately strong ρ value for the NCA pack's absolute discharge slope and $\tau_{MinCell}$ (controlling for pack SoH) of -0.56, it would appear that while $\tau_{MinCell}$ correlates with σ_{pack} and discharge slope individually, σ_{pack} and discharge slope are relatively independent of one another directly. All of the relationships described in this section were weak or statistically insignificant for the LFP packs, most likely due to the weak relationship between cell dynamics and SoH described in section 10.

13 CtCV Modeling Results

Table 6 details the accuracy of the pack standard deviation models for both chemistries. Without the inclusion of MinCell both models performed extremely poorly in properly categorizing pack standard deviation. The inclusion of the minimum SoH cell increased the accuracy of both substantially. This is likely due to the fact that the training data for the standard deviation models was the same as the SoH models. If the information present in the data alluded to overall pack SoH, then the inclusion of the SoH of one of four cells, and specifically the minimum SoH cell, provided enough data to produce modestly accurate categorization. The NCA model was more accurate, perhaps primarily due to the higher accuracy of NCA pack SoH estimation, though the relationship between dynamic voltage response and σ_{pack} being stronger in NCA packs than LFP packs may have played a minor role as well.

The NCA and LFP standard deviation PLS models that contained the MinCell variable were created with 8 and 3 latent variables, respectively. The results of the cross-validation procedures for both chemistries are shown in Figures 38 and 39.

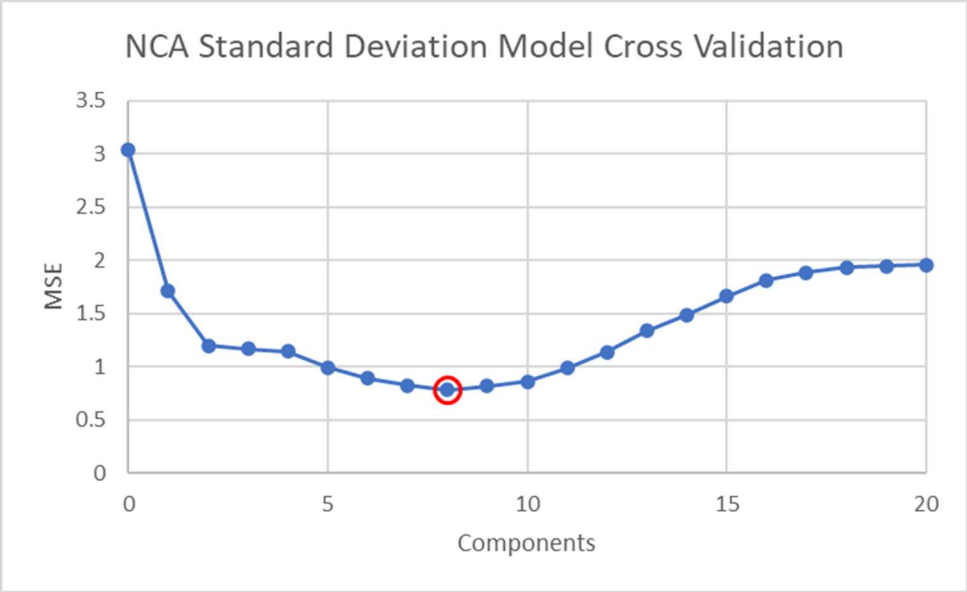

Figure 38: Results from leave-one-out cross-validation procedure for NCA pack standard deviation model. The MSE of the packs is shown to change as more latent variables are included in the model. The minimum MSEP for the number of latent variables tested is circled in red. This corresponds to the number of latent variables included in the final NCA pack standard deviation model.

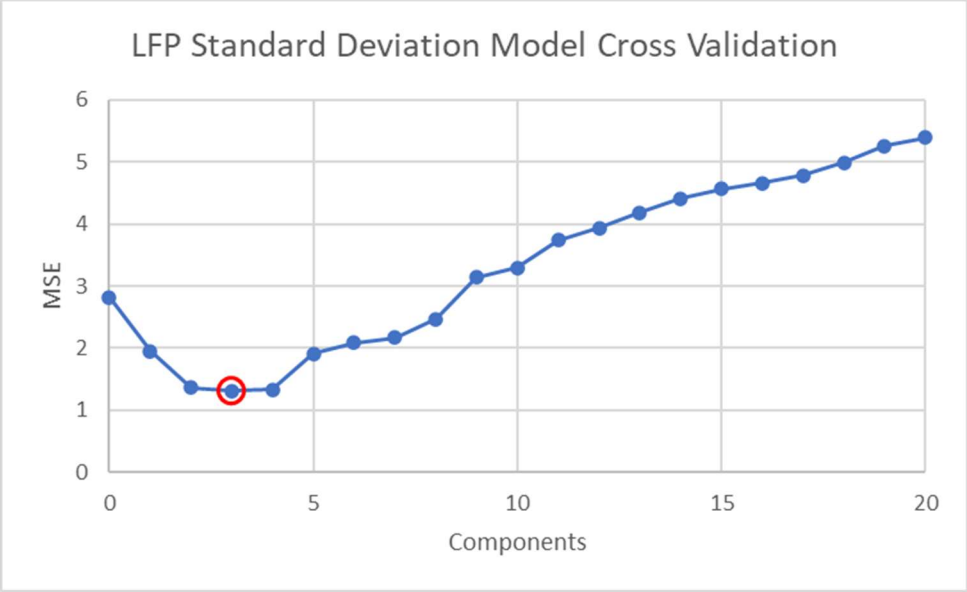

Figure 39: Results from leave-one-out cross-validation procedure for LFP pack standard deviation model. The MSE of the packs is shown to change as more latent variables are included in the model. The minimum MSEP for the number of latent variables tested is circled in red. This corresponds to the number of latent variables included in the final LFP pack standard deviation model.

Figures 40 and 41 detail the models' classification predictions with MinCell included. For both chemistries no "High" standard deviation packs were predicted "Low" and vice versa, but packs were often mis-classified as having "Medium" standard deviation. Results indicate that pack-level voltage data and the minimum SoH cell in a pack can provide a basic understanding of SoH CtCV. Experimentation on larger packs will need to be undertaken to establish the limits of this premise.

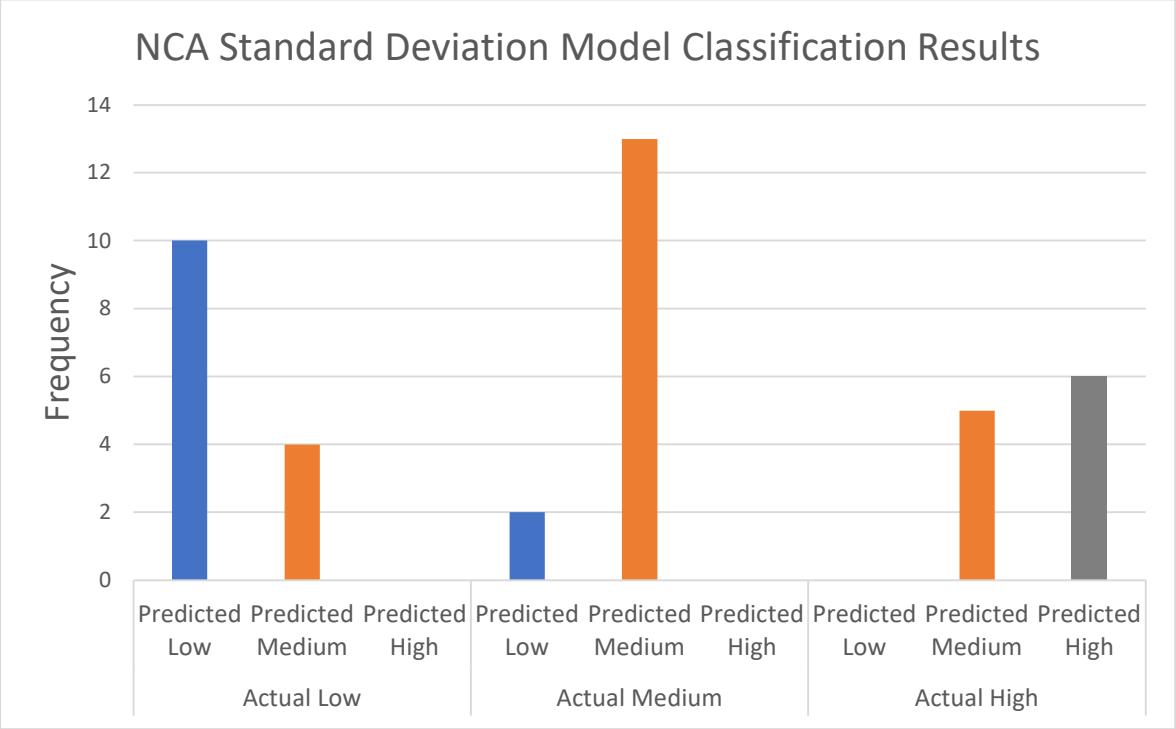

Figure 40: Pack standard deviation model classification results for NCA testing data set. The actual pack standard deviation classifications and the model's predicted standard deviation classification are specified.

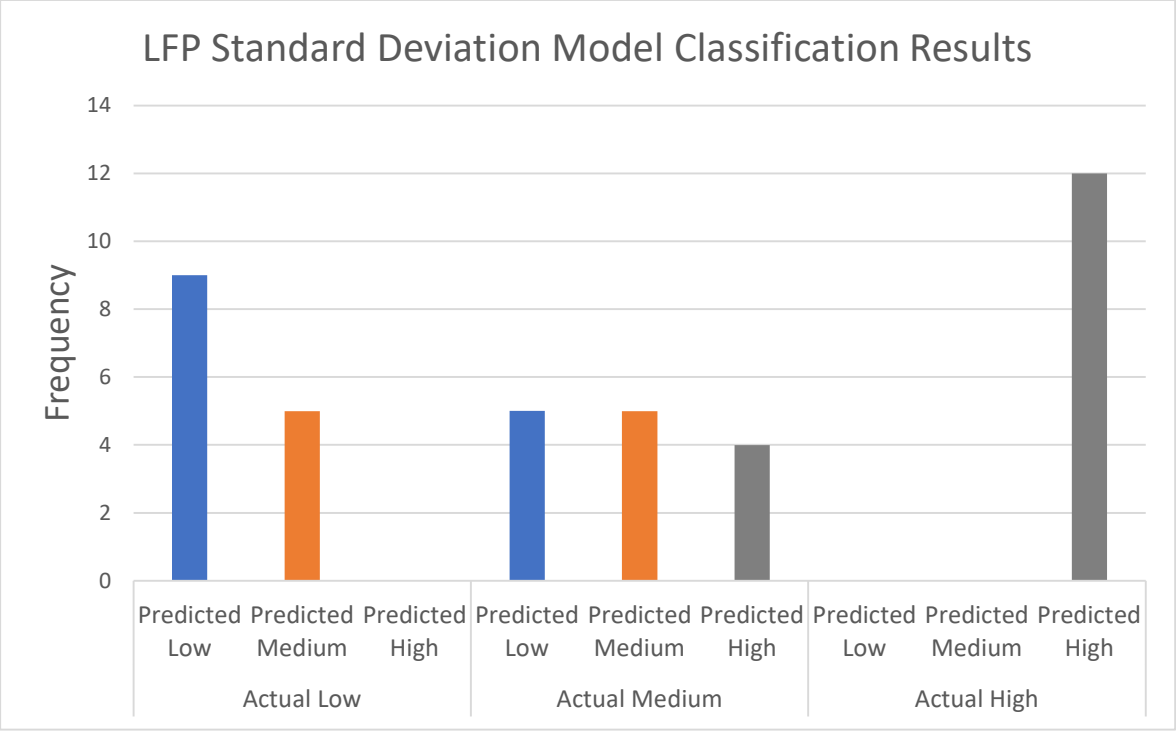

Figure 41: Pack standard deviation model classification results for LFP testing data set. The actual pack standard deviation classifications and the model's predicted standard deviation classification are specified.

14 Experimental Sources of Error

Despite diligent care taken to maintain experimental integrity and reproducibility, there are a number of sources of error in this study worth mentioning. Based on the relationships dictated by Ohm's law, consistent contact resistance between battery terminals and electrical load is critical to produce comparable voltage responses of experimental battery cells and packs. In response, cell and pack test fixtures were strategically designed with the purpose to produce uniform contact pressure and surface area to the experimental batteries. However, it is possible that 3D printing tolerances and unobserved strain in test fixtures would produce imperfect consistency between tests.

Unintended variation between cells may also be a source of error for this study. Intrinsic variations, of course, are always present in battery experimentation. Efforts were made to limit these effects by using multiple redundant cells and packs with the same approximate SoH and SoH CtCV for model training and

testing. Extrinsic sources outside of aforementioned contact resistances are also of relevance. While NCA cells were all degraded under the same conditions, the LFP cells used from a previous study were partially degraded under temperature gradients and different cycling conditions than the NCA cells. Based on the pathway dependence of degradation sources and resultant battery behaviors, this could produce imperfect comparisons between the two battery chemistries as well as variation amongst the LFP cells.

The calculation of time constant values for experimental packs and cells is another area for critique. In theory, time constant values should be calculated based on the battery voltage relaxing to full open-circuit voltage. Given that full voltage relaxation can take several hours, the voltage after a short rest was used in place of OCV for expediency, as stated in sections 6 and 7. Though the magnitude of voltage change between the actual and approximated value for OCV is minimal (several mV), it is technically incorrect. Cross referencing and confirming results with the literature and using the lower resolution equivalent of a one-RC Thévenin model gives confidence that the impacts of this approximation are minor. Furthermore, time constant values were used for conceptual interpretation of test results and did not play a role in model training or testing.

Finally, measurement errors from the Arbin system and rounding errors from data processing can attribute errors to the modeling results. Given that the same Arbin system was used for all cell and pack testing and the same data processing schemes were applied to all data, these errors are considered to be equal in effect across all data. Therefore, comparisons between the voltage responses of all experimental cells and packs should be considered appropriate.

Part V. Conclusion

15 Research Summary

NCA and LFP battery packs were tested to train pack SoH and SoH CtCV PLS models. Pack SoH was defined as the cumulative capacity of the pack divided by its cumulative nominal capacity. SoH CtCV was defined in terms of the standard deviation of cell SoH in a pack. Each pack was made up of four cells in series that were degraded to form packs of various SoH and SoH CtCV. For each battery chemistry 100 packs were used to train the models and 40 additional packs were used to validate the models' accuracy. The under 3-minute tests performed on the packs consisted of a quick charge pulse followed by a rest and extended low-current discharge pulse. The voltage response from each second of the test were used as predictor variables in the PLS models. Models were also created with and without the addition of the minimum SoH cell in a pack (i.e., "MinCell") as a predictor variable.

Analysis of test results showed that the slope of the discharge voltage response curves had a strong correlation with the dynamic voltage response of the NCA packs. The dynamic response of the NCA packs was shown to have a strong relationship with pack SoH, and at a given pack SoH the minimum SoH cell within the pack dominated the overall dynamic response of the pack. The dynamics of the minimum SoH cell was also shown to have moderately strong relationships with SoH CtCV and the slope of the discharge voltage response curve, though the SoH CtCV and voltage response slope did not appear to be directly related. No notable relationships with the LFP pack or cell dynamics were observed.

The pack SoH models without the MinCell variable produced a MAE of 0.41% and 8.50% pack SoH for the NCA and LFP packs, respectively. The difference in model accuracy was attributed to the

relationships between the dynamics of each battery chemistry and SoH. The pack SoH models including the MinCell variable produced a MAE of 0.38% and 1.43% pack SoH for the NCA and LFP packs, respectively. The relative ease of acquiring MinCell values in real-world applications provides evidence of the practical applicability of the model.

SoH CtCV models without MinCell produced unreasonable error in categorizing packs with low, medium, and high standard deviation rankings. The models including MinCell were able to properly categorize packs 72.5% and 65% of the time for NCA and LFP packs, respectively. Further experimentation is necessary to understand the effectiveness of these methods for larger packs.

In summary, the results of this study detail a reproducible methodology for LIB pack characterization. A thorough review of the relevant research literature detailed the deficiencies of common modeling practices, including the scarcity of pack-level SoH models and overly burdensome data collection and computation procedures. In response, this study leveraged quick testing procedures, easily accessible data, and computationally expedient modeling methods. Results produced accurate pack SoH models that pose major advantages over many commonly used modeling procedures.

16 Future Works

The results of this study inspire further questions regarding opportunities to expand on this work. In order to further identify the practicality of these methods, several incremental approaches should be taken to identify the limitations of these procedures in accurately estimating pack SoH. Considering the varying voltage responses and subsequent modeling results of the NCA and LFP packs, testing procedures should be reproduced using additional commonly used LIB chemistries, such as NMC and LCO cells. This would be a simple procedure to help further identify the practical scope of these methods. To that end, larger SoH ranges could be modeled using cells degraded below 80% capacity, as

cells are frequently retired well after their supposed EoL conditions [37]. Provided the proper testing equipment is available, larger series packs should be tested to validate the applicability of these PLS models for use in larger energy storage applications. This would also provide insight to better understand the impact of including or excluding the MinCell variable in the estimation accuracy of pack SoH and SoH CtCV. To closer reflect common LIB operating conditions, additional relevant variables that affect voltage behavior could be included in the models. These would include environmental conditions like temperature, or testing the cells at various SoC. The added interactions of multiple variables would significantly increase model complexity and likely require much larger training and testing data sets. Finally, the test pulse profile could be optimized by identifying the most important components for parameter estimation in the test procedures. Prior to producing this study, brief testing was performed on several NCA and LFP cells before selecting final pulse testing procedures. Longer and higher current pulses produced more variation in voltage responses between cell SoH, hence the selection of a maximum 2C charge pulse and long secondary pulse for this test. A more systematic approach may be effective in reducing testing times and increasing predictive accuracy.

References

[1] Y. Ding, Z. P. Cano, A. Yu, J. Lu, and Z. Chen, "Automotive Li-Ion Batteries: Current Status and Future Perspectives," *Electrochem. Energ. Rev.*, Jan. 2019, doi: 10.1007/s41918-018-0022-z.

[2] International Energy Agency, *Global EV Outlook 2022: Securing supplies for an electric future*. OECD, 2022.

[3] J. M. Tarascon and M. Armand, "Issues and challenges facing rechargeable lithium batteries.," *Nature*, vol. 414, no. 6861, pp. 359–367, Nov. 2001, doi: 10.1038/35104644.

[4] B. J. Landi, M. J. Ganter, C. D. Cress, R. A. DiLeo, and R. P. Raffaelle, "Carbon nanotubes for lithium ion batteries," *Energy Environ. Sci.*, vol. 2, no. 6, p. 638, 2009, doi: 10.1039/b904116h.

[5] V. Srinivasan, D. Hafemeister, B. Levi, M. Levine, and P. Schwartz, "Batteries for vehicular applications," in *AIP Conference Proceedings*, 2008, pp. 283–296, doi: 10.1063/1.2993726.

[6] B. Scrosati, "Lithium Rocking Chair Batteries: An Old Concept?," *J. Electrochem. Soc.*, vol. 139, no. 10, p. 2776, 1992, doi: 10.1149/1.2068978.

[7] X. Yuan, H. Liu, and J. Zhang, Eds., *Lithium-Ion Batteries: Advanced Materials and Technologies*, illustrated ed. CRC Press, 2011.

[8] Y. Mekonnen, A. Sundararajan, and A. I. Sarwat, "A review of cathode and anode materials for lithium-ion batteries," in *SoutheastCon 2016*, Mar. 2016, pp. 1–6, doi: 10.1109/SECON.2016.7506639.

[9] P. Zhu, D. Gastol, J. Marshall, R. Sommerville, V. Goodship, and E. Kendrick, "A review of current collectors for lithium-ion batteries," *J. Power Sources*, vol. 485, p. 229321, Feb. 2021, doi: 10.1016/j.jpowsour.2020.229321.

[10] P. Keil *et al.*, "Calendar Aging of Lithium-Ion Batteries," *J. Electrochem. Soc.*, vol. 163, no. 9, pp. A1872–A1880, 2016, doi: 10.1149/2.0411609jes.

[11] D. Linden and T. B. Reddy, *Handbook Of Batteries*, 3rd ed. New York: McGraw-Hill Professional, 2001, p. 1200.

[12] G. Plett, "Battery Management Systems, Volume I: Battery Modeling | Artech books | IEEE Xplore," 2015. http://ieeexplore.ieee.org/document/9100168 (accessed Oct. 27, 2022).

[13] N. Nitta, F. Wu, J. T. Lee, and G. Yushin, "Li-ion battery materials: present and future," *Materials Today*, vol. 18, no. 5, pp. 252–264, Jun. 2015, doi: 10.1016/j.mattod.2014.10.040.

[14] G.-N. Zhu, Y.-G. Wang, and Y.-Y. Xia, "Ti-based compounds as anode materials for Li-ion batteries," *Energy Environ. Sci.*, vol. 5, no. 5, p. 6652, 2012, doi: 10.1039/c2ee03410g.

[15] R. Wang, W. Cui, F. Chu, and F. Wu, "Lithium metal anodes: Present and future," *Journal of Energy Chemistry*, vol. 48, pp. 145–159, Sep. 2020, doi: 10.1016/j.jechem.2019.12.024.

[16] A.-I. Stan, M. Swierczynski, D.-I. Stroe, R. Teodorescu, and S. J. Andreasen, “Lithium ion battery chemistries from renewable energy storage to automotive and back-up power applications — An overview,” in *2014 International Conference on Optimization of Electrical and Electronic Equipment (OPTIM)*, May 2014, pp. 713–720, doi: 10.1109/OPTIM.2014.6850936.

[17] D. Beck, P. Dechent, M. Junker, D. U. Sauer, and M. Dubarry, “Inhomogeneities and Cell-to-Cell Variations in Lithium-Ion Batteries, a Review,” *Energies*, vol. 14, no. 11, p. 3276, Jun. 2021, doi: 10.3390/en14113276.

[18] F. Feng, X. Hu, L. Hu, F. Hu, Y. Li, and L. Zhang, “Propagation mechanisms and diagnosis of parameter inconsistency within Li-Ion battery packs,” *Renew. Sustain. Energy Rev*, vol. 112, pp. 102–113, Sep. 2019, doi: 10.1016/j.rser.2019.05.042.

[19] Custom Market Insights, “[Latest] Global Lithium-Ion Battery Market Size/Share Worth.” https://www.globenewswire.com/en/news-release/2022/12/05/2567019/0/en/Latest-Global-Lithium-Ion-Battery-Market-Size-Share-Worth-USD-184-15-Billion-by-2030-at-an-18-5-CAGR-Custom-Market-Insights-Analysis-Outlook-Leaders-Report-Trends-Forecast-Segmenta.html (accessed Feb. 06, 2023).

[20] C. Pillot, “The rechargeable battery market and main trends 2018-2030.,” *36th annual international battery seminar & exhibit. avicenne energy*.

[21] G. Zubi, R. Dufo-López, M. Carvalho, and G. Pasaoglu, “The lithium-ion battery: State of the art and future perspectives,” *Renew. Sustain. Energy Rev*, vol. 89, pp. 292–308, Jun. 2018, doi: 10.1016/j.rser.2018.03.002.

[22] A. Colthorpe, “Lithium battery pack prices go up in BloombergNEF annual survey.” https://www.energy-storage.news/lithium-battery-pack-prices-go-up-for-first-time-since-bloombergnef-began-annual-survey/ (accessed Feb. 06, 2023).

[23] J. Dunn, M. Slattery, A. Kendall, H. Ambrose, and S. Shen, “Circularity of Lithium-Ion Battery Materials in Electric Vehicles.,” *Environ. Sci. Technol.*, vol. 55, no. 8, pp. 5189–5198, Apr. 2021, doi: 10.1021/acs.est.0c07030.

[24] M. Berecibar, I. Gandiaga, I. Villarreal, N. Omar, J. Van Mierlo, and P. Van den Bossche, “Critical review of state of health estimation methods of Li-ion batteries for real applications,” *Renew. Sustain. Energy Rev*, vol. 56, pp. 572–587, Apr. 2016, doi: 10.1016/j.rser.2015.11.042.

[25] J. Bi, T. Zhang, H. Yu, and Y. Kang, “State-of-health estimation of lithium-ion battery packs in electric vehicles based on genetic resampling particle filter,” *Appl. Energy*, vol. 182, pp. 558–568, Nov. 2016, doi: 10.1016/j.apenergy.2016.08.138.

[26] P. Marques, R. Garcia, L. Kulay, and F. Freire, “Comparative life cycle assessment of lithium-ion batteries for electric vehicles addressing capacity fade,” *J. Clean. Prod.*, vol. 229, pp. 787–794, Aug. 2019, doi: 10.1016/j.jclepro.2019.05.026.

[27] X. Hu, F. Feng, K. Liu, L. Zhang, J. Xie, and B. Liu, “State estimation for advanced battery management: Key challenges and future trends,” *Renew. Sustain. Energy Rev*, vol. 114, p. 109334, Oct. 2019, doi: 10.1016/j.rser.2019.109334.

[28] T. Q. Duong, “USABC and PNGV test procedures,” *J. Power Sources*, vol. 89, no. 2, pp. 244–248, Aug. 2000, doi: 10.1016/S0378-7753(00)00439-0.

[29] L. Yao *et al.*, “A Review of Lithium-Ion Battery State of Health Estimation and Prediction Methods,” *WEVJ*, vol. 12, no. 3, p. 113, Aug. 2021, doi: 10.3390/wevj12030113.

[30] S. Saxena, C. Le Floch, J. MacDonald, and S. Moura, “Quantifying EV battery end-of-life through analysis of travel needs with vehicle powertrain models,” *J. Power Sources*, vol. 282, pp. 265–276, May 2015, doi: 10.1016/j.jpowsour.2015.01.072.

[31] R. Gold, “Status report on electrification policy: where to next?,” *Curr. Sustainable Renewable Energy Rep.*, vol. 8, no. 2, pp. 114–122, Mar. 2021, doi: 10.1007/s40518-021-00180-w.

[32] N. W. A. Lidula and A. D. Rajapakse, “Microgrids research: A review of experimental microgrids and test systems,” *Renew. Sustain. Energy Rev*, vol. 15, no. 1, pp. 186–202, Jan. 2011, doi: 10.1016/j.rser.2010.09.041.

[33] L. Canals Casals, B. Amante García, and M. M. González Benítez, “A cost analysis of electric vehicle batteries second life businesses,” in *Project management and engineering research, 2014*, J. L. Ayuso Muñoz, J. L. Yagüe Blanco, and S. F. Capuz-Rizo, Eds. Cham: Springer International Publishing, 2016, pp. 129–141.

[34] R. Sathre, C. D. Scown, O. Kavvada, and T. P. Hendrickson, “Energy and climate effects of second-life use of electric vehicle batteries in California through 2050,” *J. Power Sources*, vol. 288, pp. 82–91, Aug. 2015, doi: 10.1016/j.jpowsour.2015.04.097.

[35] N. Jiao and S. Evans, “Business Models for Sustainability: The Case of Second-life Electric Vehicle Batteries,” *Procedia CIRP*, vol. 40, pp. 250–255, 2016, doi: 10.1016/j.procir.2016.01.114.

[36] Y. Zhao *et al.*, “A Review on Battery Market Trends, Second-Life Reuse, and Recycling,” *Sustainable Chemistry*, vol. 2, no. 1, pp. 167–205, Mar. 2021, doi: 10.3390/suschem2010011.

[37] J. Lacap, J. W. Park, and L. Beslow, “Development and Demonstration of Microgrid System Utilizing Second-Life Electric Vehicle Batteries,” *Journal of Energy Storage*, vol. 41, p. 102837, Sep. 2021, doi: 10.1016/j.est.2021.102837.

[38] G. L. Plett, *Battery Management Systems, Volume II: Equivalent-Circuit Methods*, 2nd Revised edition. Artech House, 2020, p. 328.

[39] J. Jiang and C. Zhang, *Fundamentals and Applications of Lithium-ion Batteries in Electric Drive Vehicles*, 1st ed. Singapore: Wiley, 2015, p. 300.

[40] W. Sung and C. B. Shin, “Electrochemical model of a lithium-ion battery implemented into an automotive battery management system,” *Comput. Chem. Eng.*, vol. 76, pp. 87–97, May 2015, doi: 10.1016/j.compchemeng.2015.02.007.

[41] H. A. Gabbar, A. M. Othman, and M. R. Abdussami, “Review of battery management systems (BMS) development and industrial standards,” *Technologies*, vol. 9, no. 2, p. 28, Apr. 2021, doi: 10.3390/technologies9020028.

[42] M. Kaliaperumal *et al.*, “Cause and Mitigation of Lithium-Ion Battery Failure-A Review.,” *Materials (Basel)*, vol. 14, no. 19, Sep. 2021, doi: 10.3390/ma14195676.

[43] Z. Wang, T. He, H. Bian, F. Jiang, and Y. Yang, “Characteristics of and factors influencing thermal runaway propagation in lithium-ion battery packs,” *Journal of Energy Storage*, vol. 41, p. 102956, Sep. 2021, doi: 10.1016/j.est.2021.102956.

[44] J. Vetter *et al.*, “Ageing mechanisms in lithium-ion batteries,” *J. Power Sources*, vol. 147, no. 1–2, pp. 269–281, Sep. 2005, doi: 10.1016/j.jpowsour.2005.01.006.

[45] M. S. H. Lipu *et al.*, “A review of state of health and remaining useful life estimation methods for lithium-ion battery in electric vehicles: Challenges and recommendations,” *J. Clean. Prod.*, vol. 205, pp. 115–133, Dec. 2018, doi: 10.1016/j.jclepro.2018.09.065.

[46] F. Sun, R. Xiong, and H. He, “Estimation of state-of-charge and state-of-power capability of lithium-ion battery considering varying health conditions,” *J. Power Sources*, vol. 259, pp. 166–176, Aug. 2014, doi: 10.1016/j.jpowsour.2014.02.095.

[47] L. Calearo, C. Ziras, A. Thingvad, and M. Marinelli, “Validation of electric vehicle battery capacity measurements with on-board charger.,” 2022.

[48] T. Grandjean, J. Groenewald, A. McGordon, W. Widanage, and J. Marco, “Accelerated Internal Resistance Measurements of Lithium-Ion Cells to Support Future End-of-Life Strategies for Electric Vehicles,” *Batteries*, vol. 4, no. 4, p. 49, Oct. 2018, doi: 10.3390/batteries4040049.

[49] L. He and K. G. Shin, “How long will my phone battery last?.,” *arXiv preprint arXiv:1711.03651*, 2017.

[50] L. He, E. Kim, K. G. Shin, G. Meng, and T. He, “Battery state-of-health estimation for mobile devices,” in *Proceedings of the 8th International Conference on Cyber-Physical Systems - ICCPS ’17*, New York, New York, USA, Apr. 2017, pp. 51–60, doi: 10.1145/3055004.3055018.

[51] D. Stampatori, P. P. Raimondi, and M. Noussan, “Li-Ion Batteries: A Review of a Key Technology for Transport Decarbonization,” *Energies*, vol. 13, no. 10, p. 2638, May 2020, doi: 10.3390/en13102638.

[52] M. S. Reza *et al.*, “Energy storage integration towards achieving grid decarbonization: A bibliometric analysis and future directions,” *Journal of Energy Storage*, vol. 41, p. 102855, Sep. 2021, doi: 10.1016/j.est.2021.102855.

[53] Amnesty International, “‘This is what We Die For’: Human Rights Abuses in the Democratic Republic of the Congo Power the Global Trade in Cobalt,” Amnesty International Ltd, 2016.

[54] J. F. Peters, M. Baumann, B. Zimmermann, J. Braun, and M. Weil, “The environmental impact of Li-Ion batteries and the role of key parameters – A review,” *Renew. Sustain. Energy Rev*, vol. 67, pp. 491–506, Jan. 2017, doi: 10.1016/j.rser.2016.08.039.

[55] K. M. Winslow, S. J. Laux, and T. G. Townsend, “A review on the growing concern and potential management strategies of waste lithium-ion batteries,” *Resources, Conservation and Recycling*, vol. 129, pp. 263–277, Feb. 2018, doi: 10.1016/j.resconrec.2017.11.001.

[56] X. Ma, L. Azhari, and Y. Wang, “Li-ion battery recycling challenges,” *Chem*, vol. 7, no. 11, pp. 2843–2847, Nov. 2021, doi: 10.1016/j.chempr.2021.09.013.

[57] S. Yang, C. Zhang, J. Jiang, W. Zhang, L. Zhang, and Y. Wang, “Review on state-of-health of lithium-ion batteries: Characterizations, estimations and applications,” *J. Clean. Prod.*, vol. 314, p. 128015, Sep. 2021, doi: 10.1016/j.jclepro.2021.128015.

[58] H. Tian, P. Qin, K. Li, and Z. Zhao, “A review of the state of health for lithium-ion batteries: Research status and suggestions,” *J. Clean. Prod.*, vol. 261, p. 120813, Jul. 2020, doi: 10.1016/j.jclepro.2020.120813.

[59] X. Zhou, J. L. Stein, and T. Ersal, “Battery state of health monitoring by estimation of the number of cyclable Li-ions,” *Control Eng. Pract.*, vol. 66, pp. 51–63, Sep. 2017, doi: 10.1016/j.conengprac.2017.05.009.

[60] G. K. Prasad and C. D. Rahn, “Model based identification of aging parameters in lithium ion batteries,” *J. Power Sources*, vol. 232, pp. 79–85, Jun. 2013, doi: 10.1016/j.jpowsour.2013.01.041.

[61] Y. Hua, A. Cordoba-Arenas, N. Warner, and G. Rizzoni, “A multi time-scale state-of-charge and state-of-health estimation framework using nonlinear predictive filter for lithium-ion battery pack with passive balance control,” *J. Power Sources*, vol. 280, pp. 293–312, Apr. 2015, doi: 10.1016/j.jpowsour.2015.01.112.

[62] A. Cordoba-Arenas, S. Onori, and G. Rizzoni, “A control-oriented lithium-ion battery pack model for plug-in hybrid electric vehicle cycle-life studies and system design with consideration of health management,” *J. Power Sources*, vol. 279, pp. 791–808, Apr. 2015, doi: 10.1016/j.jpowsour.2014.12.048.

[63] Y. Zheng, L. Lu, X. Han, J. Li, and M. Ouyang, “LiFePO4 battery pack capacity estimation for electric vehicles based on charging cell voltage curve transformation,” *J. Power Sources*, vol. 226, pp. 33–41, Mar. 2013, doi: 10.1016/j.jpowsour.2012.10.057.

[64] J. Tian *et al.*, “Lithium-ion battery health estimation with real-world data for electric vehicles,” *Energy*, vol. 270, p. 126855, May 2023, doi: 10.1016/j.energy.2023.126855.

[65] W. Diao, J. Jiang, C. Zhang, H. Liang, and M. Pecht, “Energy state of health estimation for battery packs based on the degradation and inconsistency,” *Energy Procedia*, vol. 142, pp. 3578–3583, Dec. 2017, doi: 10.1016/j.egypro.2017.12.248.

[66] X. Zhang, Y. Wang, C. Liu, and Z. Chen, “A novel approach of battery pack state of health estimation using artificial intelligence optimization algorithm,” *J. Power Sources*, vol. 376, pp. 191–199, Feb. 2018, doi: 10.1016/j.jpowsour.2017.11.068.

[67] X. Han *et al.*, “A review on the key issues of the lithium ion battery degradation among the whole life cycle,” *eTransportation*, vol. 1, p. 100005, Aug. 2019, doi: 10.1016/j.etran.2019.100005.

[68] D. Ren *et al.*, “A comparative investigation of aging effects on thermal runaway behavior of lithium-ion batteries,” *eTransportation*, vol. 2, p. 100034, Nov. 2019, doi: 10.1016/j.etran.2019.100034.

[69] M. Dubarry, C. Truchot, and B. Y. Liaw, “Synthesize battery degradation modes via a diagnostic and prognostic model,” *J. Power Sources*, vol. 219, pp. 204–216, Dec. 2012, doi: 10.1016/j.jpowsour.2012.07.016.

[70] C. R. Birkl, M. R. Roberts, E. McTurk, P. G. Bruce, and D. A. Howey, “Degradation diagnostics for lithium ion cells,” *J. Power Sources*, vol. 341, pp. 373–386, Feb. 2017, doi: 10.1016/j.jpowsour.2016.12.011.

[71] X. Han, M. Ouyang, L. Lu, J. Li, Y. Zheng, and Z. Li, “A comparative study of commercial lithium ion battery cycle life in electrical vehicle: Aging mechanism identification,” *J. Power Sources*, vol. 251, pp. 38–54, Apr. 2014, doi: 10.1016/j.jpowsour.2013.11.029.

[72] S. Zhang, K. Zhao, T. Zhu, and J. Li, “Electrochemomechanical degradation of high-capacity battery electrode materials,” *Prog. Mater. Sci.*, vol. 89, pp. 479–521, Aug. 2017, doi: 10.1016/j.pmatsci.2017.04.014.

[73] R. Koerver *et al.*, “Chemo-mechanical expansion of lithium electrode materials – On the route to mechanically optimized all-solid-state batteries,” *Energy Environ. Sci.*, 2018, doi: 10.1039/C8EE00907D.

[74] A. Franco Gonzalez, N.-H. Yang, and R.-S. Liu, “Silicon Anode Design for Lithium-Ion Batteries: Progress and Perspectives,” *J. Phys. Chem. C*, vol. 121, no. 50, pp. 27775–27787, Dec. 2017, doi: 10.1021/acs.jpcc.7b07793.

[75] J.-M. Kim and H.-T. Chung, “The first cycle characteristics of Li[Ni1/3Co1/3Mn1/3]O2 charged up to 4.7 V,” *Electrochim. Acta*, vol. 49, no. 6, pp. 937–944, Mar. 2004, doi: 10.1016/j.electacta.2003.10.005.

[76] W.-J. Zhang, “Structure and performance of LiFePO4 cathode materials: A review,” *J. Power Sources*, vol. 196, no. 6, pp. 2962–2970, Mar. 2011, doi: 10.1016/j.jpowsour.2010.11.113.

[77] A. Wang, S. Kadam, H. Li, S. Shi, and Y. Qi, “Review on modeling of the anode solid electrolyte interphase (SEI) for lithium-ion batteries,” *npj Comput. Mater.*, vol. 4, no. 1, p. 15, Dec. 2018, doi: 10.1038/s41524-018-0064-0.

[78] S. J. An, J. Li, C. Daniel, D. Mohanty, S. Nagpure, and D. L. Wood, “The state of understanding of the lithium-ion-battery graphite solid electrolyte interphase (SEI) and its relationship to formation cycling,” *Carbon N Y*, vol. 105, pp. 52–76, Aug. 2016, doi: 10.1016/j.carbon.2016.04.008.

[79] A. Mukhopadhyay, A. Tokranov, X. Xiao, and B. W. Sheldon, “Stress development due to surface processes in graphite electrodes for Li-ion batteries: A first report,” *Electrochim. Acta*, vol. 66, pp. 28–37, Apr. 2012, doi: 10.1016/j.electacta.2012.01.058.

[80] Y. Merla, B. Wu, V. Yufit, N. P. Brandon, R. F. Martinez-Botas, and G. J. Offer, “Novel application of differential thermal voltammetry as an in-depth state-of-health diagnosis method for lithium-ion batteries,” *J. Power Sources*, vol. 307, pp. 308–319, Mar. 2016, doi: 10.1016/j.jpowsour.2015.12.122.

[81] M. Broussely *et al.*, “Main aging mechanisms in Li ion batteries,” *J. Power Sources*, vol. 146, no. 1–2, pp. 90–96, Aug. 2005, doi: 10.1016/j.jpowsour.2005.03.172.

[82] M. Naumann, M. Schimpe, P. Keil, H. C. Hesse, and A. Jossen, “Analysis and modeling of calendar aging of a commercial LiFePO 4 /graphite cell,” *Journal of Energy Storage*, vol. 17, pp. 153–169, Jun. 2018, doi: 10.1016/j.est.2018.01.019.

[83] I. Bloom *et al.*, “Differential voltage analyses of high-power, lithium-ion cells,” *J. Power Sources*, vol. 139, no. 1–2, pp. 295–303, Jan. 2005, doi: 10.1016/j.jpowsour.2004.07.021.

[84] M. Schimpe, M. E. von Kuepach, M. Naumann, H. C. Hesse, K. Smith, and A. Jossen, “Comprehensive Modeling of Temperature-Dependent Degradation Mechanisms in Lithium Iron Phosphate Batteries,” *J. Electrochem. Soc.*, vol. 165, no. 2, pp. A181–A193, 2018, doi: 10.1149/2.1181714jes.

[85] W. Situ *et al.*, “Effect of high temperature environment on the performance of LiNi0.5Co0.2Mn0.3O2 battery,” *Int. J. Heat Mass Transf.*, vol. 104, pp. 743–748, Jan. 2017, doi: 10.1016/j.ijheatmasstransfer.2016.09.005.

[86] T. T. Lou, W. G. Zhang, H. Y. Guo, and J. S. Wang, “The Internal Resistance Characteristics of Lithium-Ion Battery Based on HPPC Method,” *AMR*, vol. 455–456, pp. 246–251, Jan. 2012, doi: 10.4028/www.scientific.net/AMR.455-456.246.

[87] S. Hossain Ahmed, X. Kang, and S. O. Bade Shrestha, “Effects of Temperature on Internal Resistances of Lithium-Ion Batteries,” *J. Energy Resour. Technol.*, vol. 137, no. 3, May 2015, doi: 10.1115/1.4028698.

[88] Z. Lu *et al.*, “A comprehensive experimental study on temperature-dependent performance of lithium-ion battery,” *Appl. Therm. Eng.*, vol. 158, p. 113800, Jul. 2019, doi: 10.1016/j.applthermaleng.2019.113800.

[89] G. Kucinskis, M. Bozorgchenani, M. Feinauer, M. Kasper, M. Wohlfahrt-Mehrens, and T. Waldmann, “Arrhenius plots for Li-ion battery ageing as a function of temperature, C-rate, and ageing state – An experimental study,” *J. Power Sources*, vol. 549, p. 232129, Nov. 2022, doi: 10.1016/j.jpowsour.2022.232129.

[90] D. Ouyang, J. Weng, M. Chen, and J. Wang, “Impact of high-temperature environment on the optimal cycle rate of lithium-ion battery,” *Journal of Energy Storage*, vol. 28, p. 101242, Apr. 2020, doi: 10.1016/j.est.2020.101242.

[91] W. Tang, W. C. Tam, L. Yuan, T. Dubaniewicz, R. Thomas, and J. Soles, “Estimation of the critical external heat leading to the failure of lithium-ion batteries.,” *Appl. Therm. Eng.*, vol. 179, Oct. 2020, doi: 10.1016/j.applthermaleng.2020.115665.

[92] Y. Wu, P. Keil, S. F. Schuster, and A. Jossen, “Impact of Temperature and Discharge Rate on the Aging of a $LiCoO_2$ /$LiNi_{0.8}Co_{0.15}Al_{0.05}O_2$ Lithium-Ion Pouch Cell,” *J. Electrochem. Soc.*, vol. 164, no. 7, pp. A1438–A1445, 2017, doi: 10.1149/2.0401707jes.

[93] T. Waldmann, M. Wilka, M. Kasper, M. Fleischhammer, and M. Wohlfahrt-Mehrens, "Temperature dependent ageing mechanisms in Lithium-ion batteries – A Post-Mortem study," *J. Power Sources*, vol. 262, pp. 129–135, Sep. 2014, doi: 10.1016/j.jpowsour.2014.03.112.

[94] Y. Preger *et al.*, "Degradation of Commercial Lithium-Ion Cells as a Function of Chemistry and Cycling Conditions," *J. Electrochem. Soc.*, vol. 167, no. 12, p. 120532, Sep. 2020, doi: 10.1149/1945-7111/abae37.

[95] L. Bodenes *et al.*, "Lithium secondary batteries working at very high temperature: Capacity fade and understanding of aging mechanisms," *J. Power Sources*, vol. 236, pp. 265–275, Aug. 2013, doi: 10.1016/j.jpowsour.2013.02.067.

[96] S. Ma *et al.*, "Temperature effect and thermal impact in lithium-ion batteries: A review," *Progress in Natural Science: Materials International*, vol. 28, no. 6, pp. 653–666, Dec. 2018, doi: 10.1016/j.pnsc.2018.11.002.

[97] M. M. Kabir and D. E. Demirocak, "Degradation mechanisms in Li-ion batteries: a state-of-the-art review," *Int. J. Energy Res.*, vol. 41, no. 14, pp. 1963–1986, Nov. 2017, doi: 10.1002/er.3762.

[98] S. F. Schuster *et al.*, "Nonlinear aging characteristics of lithium-ion cells under different operational conditions," *Journal of Energy Storage*, vol. 1, pp. 44–53, Jun. 2015, doi: 10.1016/j.est.2015.05.003.

[99] D. Burow *et al.*, "Inhomogeneous degradation of graphite anodes in automotive lithium ion batteries under low-temperature pulse cycling conditions," *J. Power Sources*, vol. 307, pp. 806–814, Mar. 2016, doi: 10.1016/j.jpowsour.2016.01.033.

[100] M. Ouyang *et al.*, "Low temperature aging mechanism identification and lithium deposition in a large format lithium iron phosphate battery for different charge profiles," *J. Power Sources*, vol. 286, pp. 309–320, Jul. 2015, doi: 10.1016/j.jpowsour.2015.03.178.

[101] G. Zhang *et al.*, "Lithium plating on the anode for lithium-ion batteries during long-term low temperature cycling," *J. Power Sources*, vol. 484, p. 229312, Feb. 2021, doi: 10.1016/j.jpowsour.2020.229312.

[102] N. Piao *et al.*, "Challenges and development of lithium-ion batteries for low temperature environments," *eTransportation*, vol. 11, p. 100145, Feb. 2022, doi: 10.1016/j.etran.2021.100145.

[103] W. Wu, R. Ma, J. Liu, M. Liu, W. Wang, and Q. Wang, "Impact of low temperature and charge profile on the aging of lithium-ion battery: Non-invasive and post-mortem analysis," *Int. J. Heat Mass Transf.*, vol. 170, p. 121024, May 2021, doi: 10.1016/j.ijheatmasstransfer.2021.121024.

[104] B. K. Purushothaman and U. Landau, "Rapid charging of lithium-ion batteries using pulsed currents: A theoretical analysis.," *Journal of The Electrochemical Society*, vol. 153, no. 3, 2006.

[105] N. Legrand, B. Knosp, P. Desprez, F. Lapicque, and S. Raël, "Physical characterization of the charging process of a Li-ion battery and prediction of Li plating by electrochemical modelling," *J. Power Sources*, vol. 245, pp. 208–216, Jan. 2014, doi: 10.1016/j.jpowsour.2013.06.130.

[106] M. Petzl and M. A. Danzer, “Nondestructive detection, characterization, and quantification of lithium plating in commercial lithium-ion batteries,” *J. Power Sources*, vol. 254, pp. 80–87, May 2014, doi: 10.1016/j.jpowsour.2013.12.060.

[107] N. Gunawardhana, N. Dimov, M. Sasidharan, G.-J. Park, H. Nakamura, and M. Yoshio, “Suppression of lithium deposition at sub-zero temperatures on graphite by surface modification,” *Electrochem. commun.*, vol. 13, no. 10, pp. 1116–1118, Oct. 2011, doi: 10.1016/j.elecom.2011.07.014.

[108] Z. Li, J. Huang, B. Yann Liaw, V. Metzler, and J. Zhang, “A review of lithium deposition in lithium-ion and lithium metal secondary batteries,” *J. Power Sources*, vol. 254, pp. 168–182, May 2014, doi: 10.1016/j.jpowsour.2013.12.099.

[109] M. Petzl, M. Kasper, and M. A. Danzer, “Lithium plating in a commercial lithium-ion battery – A low-temperature aging study,” *J. Power Sources*, vol. 275, pp. 799–807, Feb. 2015, doi: 10.1016/j.jpowsour.2014.11.065.

[110] R. V. Bugga and M. C. Smart, “Lithium Plating Behavior in Lithium-Ion Cells,” *ECS Trans.*, vol. 25, no. 36, pp. 241–252, Apr. 2010, doi: 10.1149/1.3393860.

[111] L. Kong, Y. Li, and W. Feng, “Strategies to solve lithium battery thermal runaway: from mechanism to modification,” *Electrochem. Energ. Rev.*, vol. 4, no. 4, pp. 633–679, Dec. 2021, doi: 10.1007/s41918-021-00109-3.

[112] C. Hendricks, N. Williard, S. Mathew, and M. Pecht, “A failure modes, mechanisms, and effects analysis (FMMEA) of lithium-ion batteries,” *J. Power Sources*, vol. 297, pp. 113–120, Nov. 2015, doi: 10.1016/j.jpowsour.2015.07.100.

[113] J. Wen, Y. Yu, and C. Chen, “A Review on Lithium-Ion Batteries Safety Issues: Existing Problems and Possible Solutions,” *Mat. Express*, vol. 2, no. 3, pp. 197–212, Sep. 2012, doi: 10.1166/mex.2012.1075.

[114] B. Sundén, “Thermal management of batteries,” in *Hydrogen, batteries and fuel cells*, Elsevier, 2019, pp. 93–110.

[115] M. Ouyang *et al.*, “Overcharge-induced capacity fading analysis for large format lithium-ion batteries with LiyNi1/3Co1/3Mn1/3O2+LiyMn2O4 composite cathode,” *J. Power Sources*, vol. 279, pp. 626–635, Apr. 2015, doi: 10.1016/j.jpowsour.2015.01.051.

[116] N. Mao, T. Zhang, Z. Wang, and Q. Cai, “A systematic investigation of internal physical and chemical changes of lithium-ion batteries during overcharge,” *J. Power Sources*, vol. 518, p. 230767, Jan. 2022, doi: 10.1016/j.jpowsour.2021.230767.

[117] Q. Yuan, F. Zhao, W. Wang, Y. Zhao, Z. Liang, and D. Yan, “Overcharge failure investigation of lithium-ion batteries,” *Electrochim. Acta*, vol. 178, pp. 682–688, Oct. 2015, doi: 10.1016/j.electacta.2015.07.147.

[118] D. Ren, X. Feng, L. Lu, X. He, and M. Ouyang, “Overcharge behaviors and failure mechanism of lithium-ion batteries under different test conditions,” *Appl. Energy*, vol. 250, pp. 323–332, Sep. 2019, doi: 10.1016/j.apenergy.2019.05.015.

[119] T. Ohsaki *et al.*, “Overcharge reaction of lithium-ion batteries,” *J. Power Sources*, vol. 146, no. 1–2, pp. 97–100, Aug. 2005, doi: 10.1016/j.jpowsour.2005.03.105.

[120] S. Tobishima and J. Yamaki, “A consideration of lithium cell safety,” *J. Power Sources*, vol. 81–82, pp. 882–886, Sep. 1999, doi: 10.1016/S0378-7753(98)00240-7.

[121] P. Arora, “Capacity Fade Mechanisms and Side Reactions in Lithium-Ion Batteries,” *J. Electrochem. Soc.*, vol. 145, no. 10, p. 3647, 1998, doi: 10.1149/1.1838857.

[122] D. R. Baker and M. W. Verbrugge, “Modeling overcharge at graphite electrodes: plating and dissolution of lithium,” *J. Electrochem. Soc.*, vol. 167, no. 1, p. 013504, 2020, doi: 10.1149/2.0042001JES.

[123] R. D. Perkins, A. V. Randall, X. Zhang, and G. L. Plett, “Controls oriented reduced order modeling of lithium deposition on overcharge,” *J. Power Sources*, vol. 209, pp. 318–325, Jul. 2012, doi: 10.1016/j.jpowsour.2012.03.003.

[124] W. Mei, L. Zhang, J. Sun, and Q. Wang, “Experimental and numerical methods to investigate the overcharge caused lithium plating for lithium ion battery,” *Energy Storage Materials*, vol. 32, pp. 91–104, Nov. 2020, doi: 10.1016/j.ensm.2020.06.021.

[125] R. Guo, L. Lu, M. Ouyang, and X. Feng, “Mechanism of the entire overdischarge process and overdischarge-induced internal short circuit in lithium-ion batteries.,” *Sci. Rep.*, vol. 6, p. 30248, Jul. 2016, doi: 10.1038/srep30248.

[126] D. Ouyang, J. Weng, M. Chen, J. Liu, and J. Wang, “Experimental analysis on the degradation behavior of overdischarged lithium-ion battery combined with the effect of high-temperature environment,” *Int. J. Energy Res.*, vol. 44, no. 1, pp. 229–241, Jan. 2020, doi: 10.1002/er.4898.

[127] T. Langner, T. Sieber, and J. Acker, “Studies on the deposition of copper in lithium-ion batteries during the deep discharge process.,” *Sci. Rep.*, vol. 11, no. 1, p. 6316, Mar. 2021, doi: 10.1038/s41598-021-85575-x.

[128] L. Huang *et al.*, “A review of the internal short circuit mechanism in lithium-ion batteries: Inducement, detection and prevention,” *Int. J. Energy Res.*, vol. 45, no. 11, pp. 15797–15831, Sep. 2021, doi: 10.1002/er.6920.

[129] E. J. Nemanick, D. Wang, J. Matsumoto, and N. Ives, “Effects of Cell Reversal on Li-Ion Batteries,” *Meet. Abstr.*, vol. MA2016-02, no. 6, pp. 897–897, Sep. 2016, doi: 10.1149/MA2016-02/6/897.

[130] D. Juarez-Robles, A. A. Vyas, C. Fear, J. A. Jeevarajan, and P. P. Mukherjee, “Overdischarge and Aging Analytics of Li-Ion Cells,” *J. Electrochem. Soc.*, vol. 167, no. 9, p. 090558, Jan. 2020, doi: 10.1149/1945-7111/aba00a.

[131] H. Maleki and J. N. Howard, “Effects of overdischarge on performance and thermal stability of a Li-ion cell,” *J. Power Sources*, vol. 160, no. 2, pp. 1395–1402, Oct. 2006, doi: 10.1016/j.jpowsour.2006.03.043.

[132] J. Shu, M. Shui, D. Xu, D. Wang, Y. Ren, and S. Gao, “A comparative study of overdischarge behaviors of cathode materials for lithium-ion batteries,” *J. Solid State Electrochem.*, vol. 16, no. 2, pp. 819–824, Feb. 2012, doi: 10.1007/s10008-011-1484-7.

[133] G. Ning, B. Haran, and B. N. Popov, “Capacity fade study of lithium-ion batteries cycled at high discharge rates,” *J. Power Sources*, vol. 117, no. 1–2, pp. 160–169, May 2003, doi: 10.1016/S0378-7753(03)00029-6.

[134] J. Wang *et al.*, “Degradation of lithium ion batteries employing graphite negatives and nickel–cobalt–manganese oxide + spinel manganese oxide positives: Part 1, aging mechanisms and life estimation,” *J. Power Sources*, vol. 269, pp. 937–948, Dec. 2014, doi: 10.1016/j.jpowsour.2014.07.030.

[135] J. C. Burns, D. A. Stevens, and J. R. Dahn, “In-Situ Detection of Lithium Plating Using High Precision Coulometry,” *J. Electrochem. Soc.*, vol. 162, no. 6, pp. A959–A964, 2015, doi: 10.1149/2.0621506jes.

[136] J. Christensen and J. Newman, “Stress generation and fracture in lithium insertion materials,” *J. Solid State Electrochem.*, vol. 10, no. 5, pp. 293–319, May 2006, doi: 10.1007/s10008-006-0095-1.

[137] S. Sun *et al.*, “Accelerated aging and degradation mechanism of LiFePO4/graphite batteries cycled at high discharge rates.,” *RSC Adv.*, vol. 8, no. 45, pp. 25695–25703, Jul. 2018, doi: 10.1039/c8ra04074e.

[138] M. Ecker *et al.*, “Development of a lifetime prediction model for lithium-ion batteries based on extended accelerated aging test data,” *J. Power Sources*, vol. 215, pp. 248–257, Oct. 2012, doi: 10.1016/j.jpowsour.2012.05.012.

[139] J. Wang *et al.*, “Cycle-life model for graphite-LiFePO4 cells,” *J. Power Sources*, vol. 196, no. 8, pp. 3942–3948, Apr. 2011, doi: 10.1016/j.jpowsour.2010.11.134.

[140] N. Omar *et al.*, “Lithium iron phosphate based battery – Assessment of the aging parameters and development of cycle life model,” *Appl. Energy*, vol. 113, pp. 1575–1585, Jan. 2014, doi: 10.1016/j.apenergy.2013.09.003.

[141] S. Watanabe, M. Kinoshita, T. Hosokawa, K. Morigaki, and K. Nakura, “Capacity fading of LiAlyNi1−x−yCoxO2 cathode for lithium-ion batteries during accelerated calendar and cycle life tests (effect of depth of discharge in charge–discharge cycling on the suppression of the micro-crack generation of LiAlyNi1−x−yCoxO2 particle),” *J. Power Sources*, vol. 260, pp. 50–56, Aug. 2014, doi: 10.1016/j.jpowsour.2014.02.103.

[142] T. C. Bach *et al.*, “Nonlinear aging of cylindrical lithium-ion cells linked to heterogeneous compression,” *Journal of Energy Storage*, vol. 5, pp. 212–223, Feb. 2016, doi: 10.1016/j.est.2016.01.003.

[143] X.-G. Yang, Y. Leng, G. Zhang, S. Ge, and C.-Y. Wang, “Modeling of lithium plating induced aging of lithium-ion batteries: Transition from linear to nonlinear aging,” *J. Power Sources*, vol. 360, pp. 28–40, Aug. 2017, doi: 10.1016/j.jpowsour.2017.05.110.

[144] R. Spotnitz, “Simulation of capacity fade in lithium-ion batteries,” *J. Power Sources*, vol. 113, no. 1, pp. 72–80, Jan. 2003, doi: 10.1016/S0378-7753(02)00490-1.

[145] S. F. Schuster, M. J. Brand, P. Berg, M. Gleissenberger, and A. Jossen, “Lithium-ion cell-to-cell variation during battery electric vehicle operation,” *J. Power Sources*, vol. 297, pp. 242–251, Nov. 2015, doi: 10.1016/j.jpowsour.2015.08.001.

[146] M. Dubarry *et al.*, “Evaluation of commercial lithium-ion cells based on composite positive electrode for plug-in hybrid electric vehicle applications. Part II. Degradation mechanism under 2C cycle aging,” *J. Power Sources*, vol. 196, no. 23, pp. 10336–10343, Dec. 2011, doi: 10.1016/j.jpowsour.2011.08.078.

[147] M. Ecker *et al.*, “Calendar and cycle life study of Li(NiMnCo)O2-based 18650 lithium-ion batteries,” *J. Power Sources*, vol. 248, pp. 839–851, Feb. 2014, doi: 10.1016/j.jpowsour.2013.09.143.

[148] E. Sarasketa-Zabala, F. Aguesse, I. Villarreal, L. M. Rodriguez-Martinez, C. M. López, and P. Kubiak, “Understanding Lithium Inventory Loss and Sudden Performance Fade in Cylindrical Cells during Cycling with Deep-Discharge Steps,” *J. Phys. Chem. C*, vol. 119, no. 2, pp. 896–906, Jan. 2015, doi: 10.1021/jp510071d.

[149] X. Lin, J. Park, L. Liu, Y. Lee, A. M. Sastry, and W. Lu, “A Comprehensive Capacity Fade Model and Analysis for Li-Ion Batteries,” *J. Electrochem. Soc.*, vol. 160, no. 10, pp. A1701–A1710, 2013, doi: 10.1149/2.040310jes.

[150] P. M. Attia *et al.*, “Review—‘Knees’ in Lithium-Ion Battery Aging Trajectories,” *J. Electrochem. Soc.*, vol. 169, no. 6, p. 060517, Jun. 2022, doi: 10.1149/1945-7111/ac6d13.

[151] C. Strange, S. Li, R. Gilchrist, and G. dos Reis, “Elbows of Internal Resistance Rise Curves in Li-Ion Cells,” *Energies*, vol. 14, no. 4, p. 1206, Feb. 2021, doi: 10.3390/en14041206.

[152] M. Klett *et al.*, “Non-uniform aging of cycled commercial LiFePO4//graphite cylindrical cells revealed by post-mortem analysis,” *J. Power Sources*, vol. 257, pp. 126–137, Jul. 2014, doi: 10.1016/j.jpowsour.2014.01.105.

[153] Y. Bao, W. Dong, and D. Wang, “Online internal resistance measurement application in lithium ion battery capacity and state of charge estimation,” *Energies*, vol. 11, no. 5, p. 1073, Apr. 2018, doi: 10.3390/en11051073.

[154] L. Chen, Z. Lü, W. Lin, J. Li, and H. Pan, “A new state-of-health estimation method for lithium-ion batteries through the intrinsic relationship between ohmic internal resistance and capacity,” *Measurement*, vol. 116, pp. 586–595, Feb. 2018, doi: 10.1016/j.measurement.2017.11.016.

[155] X. Li, Q. Wang, Y. Yang, and J. Kang, “Correlation between capacity loss and measurable parameters of lithium-ion batteries,” *International Journal of Electrical Power & Energy Systems*, vol. 110, pp. 819–826, Sep. 2019, doi: 10.1016/j.ijepes.2019.03.046.

[156] P. Peanjad, C. Manee-Inn, and S. Khomfoi, “State of health estimation of LFP batteries using DC internal resistance and neural network,” in *2022 19th International Conference on Electrical*

Engineering/Electronics, Computer, Telecommunications and Information Technology (ECTI-CON), May 2022, pp. 1–4, doi: 10.1109/ECTI-CON54298.2022.9795407.

[157] D. Cittanti, A. Ferraris, A. Airale, S. Fiorot, S. Scavuzzo, and M. Carello, "Modeling Li-ion batteries for automotive application: A trade-off between accuracy and complexity," in *2017 International Conference of Electrical and Electronic Technologies for Automotive*, Jun. 2017, pp. 1–8, doi: 10.23919/EETA.2017.7993213.

[158] Z. Song, X.-G. Yang, N. Yang, F. P. Delgado, H. Hofmann, and J. Sun, "A study of cell-to-cell variation of capacity in parallel-connected lithium-ion battery cells," *eTransportation*, vol. 7, p. 100091, Feb. 2021, doi: 10.1016/j.etran.2020.100091.

[159] A. Barré, B. Deguilhem, S. Grolleau, M. Gérard, F. Suard, and D. Riu, "A review on lithium-ion battery ageing mechanisms and estimations for automotive applications," *J. Power Sources*, vol. 241, pp. 680–689, Nov. 2013, doi: 10.1016/j.jpowsour.2013.05.040.

[160] G. Dong, X. Zhang, C. Zhang, and Z. Chen, "A method for state of energy estimation of lithium-ion batteries based on neural network model," *Energy*, vol. 90, pp. 879–888, Oct. 2015, doi: 10.1016/j.energy.2015.07.120.

[161] Y. Jiang, J. Jiang, C. Zhang, W. Zhang, Y. Gao, and Q. Guo, "Recognition of battery aging variations for LiFePO4 batteries in 2nd use applications combining incremental capacity analysis and statistical approaches," *J. Power Sources*, vol. 360, pp. 180–188, Aug. 2017, doi: 10.1016/j.jpowsour.2017.06.007.

[162] R. Xiong, L. Li, and J. Tian, "Towards a smarter battery management system: A critical review on battery state of health monitoring methods," *J. Power Sources*, vol. 405, pp. 18–29, Nov. 2018, doi: 10.1016/j.jpowsour.2018.10.019.

[163] L. A. Middlemiss, A. J. R. Rennie, R. Sayers, and A. R. West, "Characterisation of batteries by electrochemical impedance spectroscopy," *Energy Reports*, vol. 6, pp. 232–241, May 2020, doi: 10.1016/j.egyr.2020.03.029.

[164] B. Jiang, J. Zhu, X. Wang, X. Wei, W. Shang, and H. Dai, "A comparative study of different features extracted from electrochemical impedance spectroscopy in state of health estimation for lithium-ion batteries," *Appl. Energy*, vol. 322, p. 119502, Sep. 2022, doi: 10.1016/j.apenergy.2022.119502.

[165] M.-F. Ge, Y. Liu, X. Jiang, and J. Liu, "A review on state of health estimations and remaining useful life prognostics of lithium-ion batteries," *Measurement*, vol. 174, p. 109057, Apr. 2021, doi: 10.1016/j.measurement.2021.109057.

[166] U. Tröltzsch, O. Kanoun, and H.-R. Tränkler, "Characterizing aging effects of lithium ion batteries by impedance spectroscopy," *Electrochim. Acta*, vol. 51, no. 8–9, pp. 1664–1672, Jan. 2006, doi: 10.1016/j.electacta.2005.02.148.

[167] S. Thanagasundram, R. Arunachala, K. Makinejad, T. Teutsch, and A. Jossen, "A cell level model for battery simulation.," *European Electric Vehicle Congress*, p. 1, 2012.

[168] Jong Hoon Kim, Seong Jun Lee, Jae Moon Lee, and Bo Hyung Cho, “A new direct current internal resistance and state of charge relationship for the Li-ion battery pulse power estimation,” in *2007 7th Internatonal Conference on Power Electronics*, Oct. 2007, pp. 1173–1178, doi: 10.1109/ICPE.2007.4692563.

[169] M. Coleman, W. G. Hurley, and Chin Kwan Lee, “An Improved Battery Characterization Method Using a Two-Pulse Load Test,” *IEEE Trans. Energy Convers.*, vol. 23, no. 2, pp. 708–713, Jun. 2008, doi: 10.1109/TEC.2007.914329.

[170] E. Braco, I. San Martin, P. Sanchis, A. Ursúa, and D.-I. Stroe, “Health indicator selection for state of health estimation of second-life lithium-ion batteries under extended ageing,” *Journal of Energy Storage*, vol. 55, p. 105366, Nov. 2022, doi: 10.1016/j.est.2022.105366.

[171] A. Ran *et al.*, “Fast remaining capacity estimation for lithium-ion batteries based on short-time pulse test and gaussian process regression,” *Energy Environ. Mater.*, Jun. 2022, doi: 10.1002/eem2.12386.

[172] J. Meng, L. Cai, G. Luo, D.-I. Stroe, and R. Teodorescu, “Lithium-ion battery state of health estimation with short-term current pulse test and support vector machine,” *Microelectronics Reliability*, vol. 88–90, pp. 1216–1220, Sep. 2018, doi: 10.1016/j.microrel.2018.07.025.

[173] Z. Song, X. Wu, X. Li, J. Sun, H. F. Hofmann, and J. Hou, “Current profile optimization for combined state of charge and state of health estimation of lithium ion battery based on cramer–rao bound analysis,” *IEEE Trans. Power Electron.*, vol. 34, no. 7, pp. 7067–7078, Jul. 2019, doi: 10.1109/TPEL.2018.2877294.

[174] Z. Song, H. Wang, J. Hou, H. F. Hofmann, and J. Sun, “Combined State and Parameter Estimation of Lithium-Ion Battery With Active Current Injection,” *IEEE Trans. Power Electron.*, vol. 35, no. 4, pp. 4439–4447, Apr. 2020, doi: 10.1109/TPEL.2019.2945513.

[175] M. J. Rothenberger, D. J. Docimo, M. Ghanaatpishe, and H. K. Fathy, “Genetic optimization and experimental validation of a test cycle that maximizes parameter identifiability for a Li-ion equivalent-circuit battery model,” *Journal of Energy Storage*, vol. 4, pp. 156–166, Dec. 2015, doi: 10.1016/j.est.2015.10.004.

[176] Q. Lai, H. J. Ahn, G. Kim, W. T. Joe, and X. Lin, “Optimization of Current Excitation for Identification of Battery Electrochemical Parameters based on Analytic Sensitivity Expression,” in *2020 American Control Conference (ACC)*, Jul. 2020, pp. 346–351, doi: 10.23919/ACC45564.2020.9147575.

[177] L. Zheng, J. Zhu, D. D.-C. Lu, G. Wang, and T. He, “Incremental capacity analysis and differential voltage analysis based state of charge and capacity estimation for lithium-ion batteries,” *Energy*, vol. 150, pp. 759–769, May 2018, doi: 10.1016/j.energy.2018.03.023.

[178] Q. Zhang, C.-G. Huang, H. Li, G. Feng, and W. Peng, “Electrochemical Impedance Spectroscopy Based State-of-Health Estimation for Lithium-Ion Battery Considering Temperature and State-of-Charge Effect,” *IEEE Trans. Transp. Electrific.*, vol. 8, no. 4, pp. 4633–4645, Dec. 2022, doi: 10.1109/TTE.2022.3160021.

[179] X. Hu, S. E. Li, Z. Jia, and B. Egardt, “Enhanced sample entropy-based health management of Li-ion battery for electrified vehicles,” *Energy*, vol. 64, pp. 953–960, Jan. 2014, doi: 10.1016/j.energy.2013.11.061.

[180] N. Khare, S. Chandra, and R. Govil, “Statistical modeling of SoH of an automotive battery for online indication,” in *INTELEC 2008 - 2008 IEEE 30th International Telecommunications Energy Conference*, Sep. 2008, pp. 1–7, doi: 10.1109/INTLEC.2008.4664086.

[181] M.-K. Tran *et al.*, “A comprehensive equivalent circuit model for lithium-ion batteries, incorporating the effects of state of health, state of charge, and temperature on model parameters,” *Journal of Energy Storage*, vol. 43, p. 103252, Nov. 2021, doi: 10.1016/j.est.2021.103252.

[182] K. Mc Carthy, H. Gullapalli, K. M. Ryan, and T. Kennedy, “Electrochemical impedance correlation analysis for the estimation of Li-ion battery state of charge, state of health and internal temperature,” *Journal of Energy Storage*, vol. 50, p. 104608, Jun. 2022, doi: 10.1016/j.est.2022.104608.

[183] A. Romero-Becerril and L. Alvarez-Icaza, “Comparison of discretization methods applied to the single-particle model of lithium-ion batteries,” *J. Power Sources*, vol. 196, no. 23, pp. 10267–10279, Dec. 2011, doi: 10.1016/j.jpowsour.2011.06.091.

[184] V. Ramadesigan, V. Boovaragavan, J. C. Pirkle, and V. R. Subramanian, “Efficient Reformulation of Solid-Phase Diffusion in Physics-Based Lithium-Ion Battery Models,” *J. Electrochem. Soc.*, vol. 157, no. 7, p. A854, 2010, doi: 10.1149/1.3425622.

[185] Y. Wang *et al.*, “A comprehensive review of battery modeling and state estimation approaches for advanced battery management systems,” *Renew. Sustain. Energy Rev*, vol. 131, p. 110015, Oct. 2020, doi: 10.1016/j.rser.2020.110015.

[186] Z. Wang, G. Feng, D. Zhen, F. Gu, and A. Ball, “A review on online state of charge and state of health estimation for lithium-ion batteries in electric vehicles,” *Energy Reports*, vol. 7, pp. 5141–5161, Nov. 2021, doi: 10.1016/j.egyr.2021.08.113.

[187] Z. Xia and J. A. Abu Qahouq, “Evaluation of Parameter Variations of Equivalent Circuit Model of Lithium-ion Battery under Different SOH Conditions,” in *2020 IEEE Energy Conversion Congress and Exposition (ECCE)*, Oct. 2020, pp. 1519–1523, doi: 10.1109/ECCE44975.2020.9236339.

[188] F. Leng, C. M. Tan, and M. Pecht, “Effect of Temperature on the Aging rate of Li Ion Battery Operating above Room Temperature.,” *Sci. Rep.*, vol. 5, p. 12967, Aug. 2015, doi: 10.1038/srep12967.

[189] G. L. Plett, “Dual and joint EKF for simultaneous SOC and SOH estimation.,” *Proceedings of the 21st Electric Vehicle Symposium (EVS21), Monaco*, p. 1, 2005.

[190] S. Schwunk, N. Armbruster, S. Straub, J. Kehl, and M. Vetter, “Particle filter for state of charge and state of health estimation for lithium–iron phosphate batteries,” *J. Power Sources*, vol. 239, pp. 705–710, Oct. 2013, doi: 10.1016/j.jpowsour.2012.10.058.

[191] L. Zheng, L. Zhang, J. Zhu, G. Wang, and J. Jiang, “Co-estimation of state-of-charge, capacity and resistance for lithium-ion batteries based on a high-fidelity electrochemical model,” *Appl. Energy*, vol. 180, pp. 424–434, Oct. 2016, doi: 10.1016/j.apenergy.2016.08.016.

[192] B. Ning, B. Cao, B. Wang, and Z. Zou, “Adaptive sliding mode observers for lithium-ion battery state estimation based on parameters identified online,” *Energy*, vol. 153, pp. 732–742, Jun. 2018, doi: 10.1016/j.energy.2018.04.026.

[193] X. Li, Z. Wang, and L. Zhang, “Co-estimation of capacity and state-of-charge for lithium-ion batteries in electric vehicles,” *Energy*, vol. 174, pp. 33–44, May 2019, doi: 10.1016/j.energy.2019.02.147.

[194] W. Xu *et al.*, “A novel adaptive dual extended Kalman filtering algorithm for the Li-ion battery state of charge and state of health co-estimation,” *Int. J. Energy Res.*, vol. 45, no. 10, pp. 14592–14602, Aug. 2021, doi: 10.1002/er.6719.

[195] N. Jiang and H. Pang, “Study on Co-Estimation of SoC and SoH for Second-Use Lithium-Ion Power Batteries,” *Electronics*, vol. 11, no. 11, p. 1789, Jun. 2022, doi: 10.3390/electronics11111789.

[196] Y. Li *et al.*, “Data-driven health estimation and lifetime prediction of lithium-ion batteries: A review,” *Renew. Sustain. Energy Rev*, vol. 113, p. 109254, Oct. 2019, doi: 10.1016/j.rser.2019.109254.

[197] M. Chen, G. Ma, W. Liu, N. Zeng, and X. Luo, “An overview of data-driven battery health estimation technology for battery management system,” *Neurocomputing*, vol. 532, pp. 152–169, May 2023, doi: 10.1016/j.neucom.2023.02.031.

[198] K. S. Ng, C.-S. Moo, Y.-P. Chen, and Y.-C. Hsieh, “Enhanced coulomb counting method for estimating state-of-charge and state-of-health of lithium-ion batteries,” *Appl. Energy*, vol. 86, no. 9, pp. 1506–1511, Sep. 2009, doi: 10.1016/j.apenergy.2008.11.021.

[199] A. Eddahech, O. Briat, N. Bertrand, J.-Y. Delétage, and J.-M. Vinassa, “Behavior and state-of-health monitoring of Li-ion batteries using impedance spectroscopy and recurrent neural networks,” *International Journal of Electrical Power & Energy Systems*, vol. 42, no. 1, pp. 487–494, Nov. 2012, doi: 10.1016/j.ijepes.2012.04.050.

[200] D. Andre, A. Nuhic, T. Soczka-Guth, and D. U. Sauer, “Comparative study of a structured neural network and an extended Kalman filter for state of health determination of lithium-ion batteries in hybrid electricvehicles,” *Eng. Appl. Artif. Intell.*, vol. 26, no. 3, pp. 951–961, Mar. 2013, doi: 10.1016/j.engappai.2012.09.013.

[201] D. Andre, C. Appel, T. Soczka-Guth, and D. U. Sauer, “Advanced mathematical methods of SOC and SOH estimation for lithium-ion batteries,” *J. Power Sources*, vol. 224, pp. 20–27, Feb. 2013, doi: 10.1016/j.jpowsour.2012.10.001.

[202] B. Pattipati, C. Sankavaram, and K. Pattipati, “System identification and estimation framework for pivotal automotive battery management system characteristics,” *IEEE Trans. Syst., Man, Cybern. C*, vol. 41, no. 6, pp. 869–884, Nov. 2011, doi: 10.1109/TSMCC.2010.2089979.

[203] J. Kim, S. Lee, and B. H. Cho, “Complementary cooperation algorithm based on DEKF combined with pattern recognition for soc/capacity estimation and SOH prediction,” *IEEE Trans. Power Electron.*, vol. 27, no. 1, pp. 436–451, Jan. 2012, doi: 10.1109/TPEL.2011.2158554.

[204] H. T. Lin, T. J. Liang, and S. M. Chen, “The state-of-health diagnosis of Li-Co batteries with fuzzy identification.,” *Proceedings of The 7th International Power Electronics and Motion Control Conference*, vol. 4, p. 2678, 2012.

[205] S. K. Pradhan and B. Chakraborty, “Battery management strategies: An essential review for battery state of health monitoring techniques,” *Journal of Energy Storage*, vol. 51, p. 104427, Jul. 2022, doi: 10.1016/j.est.2022.104427.

[206] C. Zhang, Y. Jiang, J. Jiang, G. Cheng, W. Diao, and W. Zhang, “Study on battery pack consistency evolutions and equilibrium diagnosis for serial- connected lithium-ion batteries,” *Appl. Energy*, Jun. 2017, doi: 10.1016/j.apenergy.2017.05.176.

[207] C. T. Love, M. B. V. Virji, R. E. Rocheleau, and K. E. Swider-Lyons, “State-of-health monitoring of 18650 4S packs with a single-point impedance diagnostic,” *J. Power Sources*, vol. 266, pp. 512–519, Nov. 2014, doi: 10.1016/j.jpowsour.2014.05.033.

[208] M. Huotari, S. Arora, A. Malhi, and K. Främling, “Comparing seven methods for state-of-health time series prediction for the lithium-ion battery packs of forklifts,” *Appl. Soft Comput.*, vol. 111, p. 107670, Nov. 2021, doi: 10.1016/j.asoc.2021.107670.

[209] D. Zhou, P. Fu, H. Yin, W. Xie, and S. Feng, “A Study of Online State-of-Health Estimation Method for In-Use Electric Vehicles Based on Charge Data,” *IEICE Trans. Inf. Syst.*, vol. E102.D, no. 7, pp. 1302–1309, Jul. 2019, doi: 10.1587/transinf.2019EDP7010.

[210] M. Dubarry, N. Vuillaume, and B. Y. Liaw, “From single cell model to battery pack simulation for Li-ion batteries,” *J. Power Sources*, vol. 186, no. 2, pp. 500–507, Jan. 2009, doi: 10.1016/j.jpowsour.2008.10.051.

[211] C. Truchot, M. Dubarry, and B. Y. Liaw, “State-of-charge estimation and uncertainty for lithium-ion battery strings,” *Appl. Energy*, vol. 119, pp. 218–227, Apr. 2014, doi: 10.1016/j.apenergy.2013.12.046.

[212] C. Zhang, G. Cheng, Q. Ju, W. Zhang, J. Jiang, and L. Zhang, “Study on Battery Pack Consistency Evolutions during Electric Vehicle Operation with Statistical Method,” *Energy Procedia*, vol. 105, pp. 3551–3556, May 2017, doi: 10.1016/j.egypro.2017.03.816.

[213] M. Dubarry, C. Pastor-Fernández, G. Baure, T. F. Yu, W. D. Widanage, and J. Marco, “Battery energy storage system modeling: Investigation of intrinsic cell-to-cell variations,” *Journal of Energy Storage*, vol. 23, pp. 19–28, Jun. 2019, doi: 10.1016/j.est.2019.02.016.

[214] M. Dubarry, N. Vuillaume, and B. Y. Liaw, “Origins and accommodation of cell variations in Li-ion battery pack modeling,” *Int. J. Energy Res.*, vol. 34, no. 2, pp. 216–231, Feb. 2010, doi: 10.1002/er.1668.

[215] M. Baumann, L. Wildfeuer, S. Rohr, and M. Lienkamp, “Parameter variations within Li-Ion battery packs – Theoretical investigations and experimental quantification,” *Journal of Energy Storage*, vol. 18, pp. 295–307, Aug. 2018, doi: 10.1016/j.est.2018.04.031.

[216] K. Rumpf, M. Naumann, and A. Jossen, “Experimental investigation of parametric cell-to-cell variation and correlation based on 1100 commercial lithium-ion cells,” *Journal of Energy Storage*, vol. 14, pp. 224–243, Dec. 2017, doi: 10.1016/j.est.2017.09.010.

[217] T. Baumhöfer, M. Brühl, S. Rothgang, and D. U. Sauer, “Production caused variation in capacity aging trend and correlation to initial cell performance,” *J. Power Sources*, vol. 247, pp. 332–338, Feb. 2014, doi: 10.1016/j.jpowsour.2013.08.108.

[218] C. Pastor-Fernández, T. Bruen, W. D. Widanage, M. A. Gama-Valdez, and J. Marco, “A Study of Cell-to-Cell Interactions and Degradation in Parallel Strings: Implications for the Battery Management System,” *J. Power Sources*, vol. 329, pp. 574–585, Oct. 2016, doi: 10.1016/j.jpowsour.2016.07.121.

[219] R. Gogoana, M. B. Pinson, M. Z. Bazant, and S. E. Sarma, “Internal resistance matching for parallel-connected lithium-ion cells and impacts on battery pack cycle life,” *J. Power Sources*, vol. 252, pp. 8–13, Apr. 2014, doi: 10.1016/j.jpowsour.2013.11.101.

[220] S. Miyatake, Y. Susuki, T. Hikihara, S. Itoh, and K. Tanaka, “Discharge characteristics of multicell lithium-ion battery with nonuniform cells,” *J. Power Sources*, vol. 241, pp. 736–743, Nov. 2013, doi: 10.1016/j.jpowsour.2013.05.179.

[221] W. Diao *et al.*, “Flexible grouping for enhanced energy utilization efficiency in battery energy storage systems,” *Energies*, vol. 9, no. 7, p. 498, Jun. 2016, doi: 10.3390/en9070498.

[222] S. Paul, C. Diegelmann, H. Kabza, and W. Tillmetz, “Analysis of ageing inhomogeneities in lithium-ion battery systems,” *J. Power Sources*, vol. 239, pp. 642–650, Oct. 2013, doi: 10.1016/j.jpowsour.2013.01.068.

[223] J. Cao, N. Schofield, and A. Emadi, “Battery balancing methods: A comprehensive review,” in *2008 IEEE Vehicle Power and Propulsion Conference*, Sep. 2008, pp. 1–6, doi: 10.1109/VPPC.2008.4677669.

[224] Y. Hua *et al.*, “A comprehensive review on inconsistency and equalization technology of lithium-ion battery for electric vehicles,” *Int. J. Energy Res.*, vol. 44, no. 14, pp. 11059–11087, Nov. 2020, doi: 10.1002/er.5683.

[225] L. H. Saw, Y. Ye, and A. A. O. Tay, “Integration issues of lithium-ion battery into electric vehicles battery pack,” *J. Clean. Prod.*, vol. 113, pp. 1032–1045, Feb. 2016, doi: 10.1016/j.jclepro.2015.11.011.

[226] I. Aizpuru, U. Iraola, J. Mari, and A. Goikoetxea, “Comparative study and evaluation of passive balancing against single switch active balancing systems for energy storage systems.,” *PCIM Europe 2016; International Exhibition and Conference for Power Electronics, Intelligent Motion, Renewable Energy and Energy Management*, p. 2016, 2016.

[227] A. Krupp, E. Ferg, F. Schuldt, K. Derendorf, and C. Agert, “Incremental Capacity Analysis as a State of Health Estimation Method for Lithium-Ion Battery Modules with Series-Connected Cells,” *Batteries*, vol. 7, no. 1, p. 2, Dec. 2020, doi: 10.3390/batteries7010002.

[228] T. R. Tanim, E. J. Dufek, L. K. Walker, C. D. Ho, C. E. Hendricks, and J. P. Christophersen, “Advanced diagnostics to evaluate heterogeneity in lithium-ion battery modules,” *eTransportation*, vol. 3, p. 100045, Feb. 2020, doi: 10.1016/j.etran.2020.100045.

[229] T. Rüther, C. Plank, M. Schamel, and M. A. Danzer, “Detection of inhomogeneities in serially connected lithium-ion batteries,” *Appl. Energy*, vol. 332, p. 120514, Feb. 2023, doi: 10.1016/j.apenergy.2022.120514.

[230] H. Wang, L. Dai, L. Mao, Y. Liu, Y. Jin, and Q. Wu, “In Situ Detection of Lithium-Ion Battery Pack Capacity Inconsistency Using Magnetic Field Scanning Imaging.,” *Small Methods*, vol. 6, no. 3, p. e2101358, Mar. 2022, doi: 10.1002/smtd.202101358.

[231] S. Raschka, “Model evaluation, model selection, and algorithm selection in machine learning.,” *arXiv preprint arXiv:1811.12808*, 2018.

[232] I. H. Witten, E. Frank, and M. A. Hall, *Data mining: practical machine learning tools and techniques*, 3rd ed. Burlington, MA. USA: Elsevier, 2011, p. 664.

[233] “APA Dictionary of Psychology.” https://dictionary.apa.org/perfect-correlation (accessed Mar. 28, 2023).

[234] X. Su, X. Yan, and C.-L. Tsai, “Linear regression,” *WIREs Comp Stat*, vol. 4, no. 3, pp. 275–294, May 2012, doi: 10.1002/wics.1198.

[235] R. D. Tobias, “An introduction to partial least squares regression.,” *Proceedings of the twentieth annual SAS users group international conference*, vol. 20, p. 1250, 1995.

[236] H. Abdi, “Partial least square regression (PLS regression).,” *Encyclopedia for research methods for the social sciences*, vol. 6, no. 4, pp. 792–795, 2003.

[237] D. T. Harvey and B. A. Hanson, “Understanding Scores and Loadings,” CRAN.R-project.org, Vignette 04, Jan. 2022. Accessed: Mar. 20, 2023. [Online]. Available: https://cran.r-project.org/web/packages/LearnPCA/vignettes/Vig_04_Scores_Loadings.pdf.

[238] P. Geladi and B. R. Kowalski, “Partial least-squares regression: a tutorial,” *Anal. Chim. Acta*, vol. 185, pp. 1–17, 1986, doi: 10.1016/0003-2670(86)80028-9.

[239] “6.7.7. How the PLS model is calculated — Process Improvement using Data.” https://learnche.org/pid/latent-variable-modelling/projection-to-latent-structures/how-the-pls-model-is-calculated (accessed Mar. 29, 2023).

[240] S. de Jong, “SIMPLS: An alternative approach to partial least squares regression,” *Chemometrics and Intelligent Laboratory Systems*, vol. 18, no. 3, pp. 251–263, Mar. 1993, doi: 10.1016/0169-7439(93)85002-X.

[241] Yu, Xie, Sang, Yang, and Huang, “State-Of-Charge Estimation for Lithium-Ion Battery Using Improved DUKF Based on State-Parameter Separation,” *Energies*, vol. 12, no. 21, p. 4036, Oct. 2019, doi: 10.3390/en12214036.

[242] P. S. Attidekou, C. Wang, M. Armstrong, S. M. Lambert, and P. A. Christensen, “A new time constant approach to online capacity monitoring and lifetime prediction of lithium ion batteries for electric vehicles (EV),” *J. Electrochem. Soc.*, vol. 164, no. 9, pp. A1792–A1801, 2017, doi: 10.1149/2.0101709jes.

[243] A. Nyman, T. G. Zavalis, R. Elger, M. Behm, and G. Lindbergh, “Analysis of the Polarization in a Li-Ion Battery Cell by Numerical Simulations,” *J. Electrochem. Soc.*, vol. 157, no. 11, p. A1236, 2010, doi: 10.1149/1.3486161.

[244] R. Guo and W. Shen, “A Review of Equivalent Circuit Model Based Online State of Power Estimation for Lithium-Ion Batteries in Electric Vehicles,” *Vehicles*, vol. 4, no. 1, pp. 1–31, Dec. 2021, doi: 10.3390/vehicles4010001.

[245] B. Zhang, M. Chen, and D. Yang, “Investigation of the polarization effect in lithium iron phosphate battery for electric vehicles,” in *2014 IEEE Conference and Expo Transportation Electrification Asia-Pacific (ITEC Asia-Pacific)*, Aug. 2014, pp. 1–5, doi: 10.1109/ITEC-AP.2014.6941178.

[246] K. Li and K. J. Tseng, “An equivalent circuit model for state of energy estimation of lithium-ion battery,” in *2016 IEEE Applied Power Electronics Conference and Exposition (APEC)*, Mar. 2016, pp. 3422–3430, doi: 10.1109/APEC.2016.7468359.

[247] L. Barzacchi, M. Lagnoni, R. D. Rienzo, A. Bertei, and F. Baronti, “Enabling early detection of lithium-ion battery degradation by linking electrochemical properties to equivalent circuit model parameters,” *Journal of Energy Storage*, vol. 50, p. 104213, Jun. 2022, doi: 10.1016/j.est.2022.104213.

[248] B. Yuan *et al.*, “Study on the Relationship Between Open-Circuit Voltage, Time Constant And Polarization Resistance of Lithium-Ion Batteries,” *J. Electrochem. Soc.*, vol. 169, no. 6, p. 060513, Jun. 2022, doi: 10.1149/1945-7111/ac7359.

[249] D. Theuerkauf and L. Swan, “Characteristics of Open Circuit Voltage Relaxation in Lithium-Ion Batteries for the Purpose of State of Charge and State of Health Analysis,” *Batteries*, vol. 8, no. 8, p. 77, Jul. 2022, doi: 10.3390/batteries8080077.

[250] X. Liu *et al.*, “Online identification of power battery parameters for electric vehicles using a decoupling multiple forgetting factors recursive least squares method.,” *CSEE Journal of Power and Energy Systems*, vol. 6, no. 3, pp. 735–742, 2019.

[251] X. Hu, S. Li, and H. Peng, “A comparative study of equivalent circuit models for Li-ion batteries,” *J. Power Sources*, vol. 198, pp. 359–367, Jan. 2012, doi: 10.1016/j.jpowsour.2011.10.013.

[252] P. Vyroubal and T. Kazda, “Equivalent circuit model parameters extraction for lithium ion batteries using electrochemical impedance spectroscopy,” *Journal of Energy Storage*, vol. 15, pp. 23–31, Feb. 2018, doi: 10.1016/j.est.2017.10.019.

[253] M.-K. Tran, A. Mevawala, S. Panchal, K. Raahemifar, M. Fowler, and R. Fraser, “Effect of integrating the hysteresis component to the equivalent circuit model of Lithium-ion battery for dynamic and non-dynamic applications,” *Journal of Energy Storage*, vol. 32, p. 101785, Dec. 2020, doi: 10.1016/j.est.2020.101785.

[254] Q.-Q. Yu, R. Xiong, L.-Y. Wang, and C. Lin, “A Comparative Study on Open Circuit Voltage Models for Lithium-ion Batteries,” *CJME*, vol. 31, no. 1, p. 65, Dec. 2018, doi: 10.1186/s10033-018-0268-8.

[255] A. Nikolian *et al.*, “Lithium Ion Batteries—Development of Advanced Electrical Equivalent Circuit Models for Nickel Manganese Cobalt Lithium-Ion,” *Energies*, vol. 9, no. 5, p. 360, May 2016, doi: 10.3390/en9050360.

[256] M.-K. Tran, A. DaCosta, A. Mevawalla, S. Panchal, and M. Fowler, “Comparative Study of Equivalent Circuit Models Performance in Four Common Lithium-Ion Batteries: LFP, NMC, LMO, NCA,” *Batteries*, vol. 7, no. 3, p. 51, Jul. 2021, doi: 10.3390/batteries7030051.

[257] A. Gholamy, V. Kreinovich, and O. Kosheleva, “Why 70/30 or 80/20 Relation Between Training and Testing Sets: A Pedagogical Explanation,” The University of Texas at El Paso, UTEP-CS-18-09, Feb. 2018.

[258] R Foundation for Statistical Computing, *R: A language and environment for statistical computing*. R Foundation for Statistical Computing, 2022.

[259] J. Zhou, B. Xing, and C. Wang, “A review of lithium ion batteries electrochemical models for electric vehicles,” *E3S Web of Conferences*, vol. 185, p. 04001, 2020, doi: 10.1051/e3sconf/202018504001.

[260] M. Lagnoni, C. Nicolella, and A. Bertei, “Survey and sensitivity analysis of critical parameters in lithium-ion battery thermo-electrochemical modeling,” *Electrochim. Acta*, vol. 394, p. 139098, Oct. 2021, doi: 10.1016/j.electacta.2021.139098.

[261] C. Weng, Y. Cui, J. Sun, and H. Peng, “On-board state of health monitoring of lithium-ion batteries using incremental capacity analysis with support vector regression,” *J. Power Sources*, vol. 235, pp. 36–44, Aug. 2013, doi: 10.1016/j.jpowsour.2013.02.012.

[262] M. A. Hoque *et al.*, “Data driven analysis of lithium-ion battery internal resistance towards reliable state of health prediction,” *J. Power Sources*, vol. 513, p. 230519, Nov. 2021, doi: 10.1016/j.jpowsour.2021.230519.

[263] K. Qian, B. Huang, A. Ran, Y.-B. He, B. Li, and F. Kang, “State-of-health (SOH) evaluation on lithium-ion battery by simulating the voltage relaxation curves,” *Electrochim. Acta*, vol. 303, pp. 183–191, Apr. 2019, doi: 10.1016/j.electacta.2019.02.055.

[264] I. Baghdadi, O. Briat, P. Gyan, and J. M. Vinassa, “State of health assessment for lithium batteries based on voltage–time relaxation measure,” *Electrochim. Acta*, vol. 194, pp. 461–472, Mar. 2016, doi: 10.1016/j.electacta.2016.02.109.

[265] J. Zhu *et al.*, “Data-driven capacity estimation of commercial lithium-ion batteries from voltage relaxation.,” *Nat. Commun.*, vol. 13, no. 1, p. 2261, Apr. 2022, doi: 10.1038/s41467-022-29837-w.

[266] K. Huang, Y.-F. Guo, M.-L. Tseng, K.-J. Wu, and Z.-G. Li, “A Novel Health Factor to Predict the Battery’s State-of-Health Using a Support Vector Machine Approach,” *Appl. Sci.*, vol. 8, no. 10, p. 1803, Oct. 2018, doi: 10.3390/app8101803.

[267] Y. Wu, Q. Xue, J. Shen, Z. Lei, Z. Chen, and Y. Liu, “State of Health Estimation for Lithium-Ion Batteries Based on Healthy Features and Long Short-Term Memory,” *IEEE Access*, vol. 8, pp. 28533–28547, 2020, doi: 10.1109/ACCESS.2020.2972344.

[268] P. Venugopal and V. T., “State-of-Health Estimation of Li-ion Batteries in Electric Vehicle Using IndRNN under Variable Load Condition,” *Energies*, vol. 12, no. 22, p. 4338, Nov. 2019, doi: 10.3390/en12224338.